August 9 to 12, 2010

Accelerated Implementation of Intelligent Compaction Technology for Embankment Subgrade Soils, Aggregate Base, and Asphalt Pavement Materials: US 12 Marmarth, North Dakota

FHWA Pooled Fund Study TPF-5 (128) ER10-08

Final Report

EERC
EARTHWORKS ENGINEERING
RESEARCH CENTER

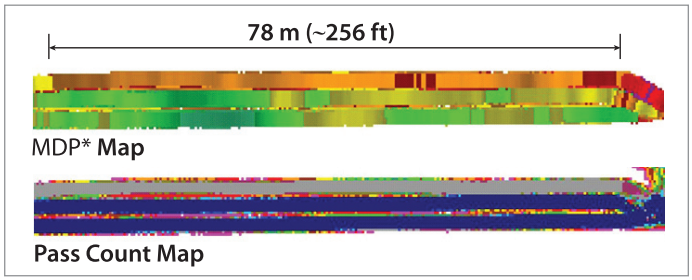

IOWA STATE UNIVERSITY
Institute for Transportation

About the EERC

The mission of the Earthworks Engineering Research Center at Iowa State University is to be the nation's premier institution for developing fundamental knowledge of earth mechanics, and creating innovative technologies, sensors, and systems to enable rapid, high quality, environmentally friendly, and economical construction of roadways, aviation runways, railroad embankments, dams, structural foundations, fortifications constructed from earth materials, and related geotechnical applications.

Disclaimer Notice

The contents of this report reflect the views of the authors, who are responsible for the facts and the accuracy of the information presented herein. The opinions, findings and conclusions expressed in this publication are those of the authors and not necessarily those of the sponsors.

The sponsors assume no liability for the contents or use of the information contained in this document. This report does not constitute a standard, specification, or regulation.

The sponsors do not endorse products or manufacturers. Trademarks or manufacturers' names appear in this report only because they are considered essential to the objective of the document.

Non-discrimination Statement

Iowa State University does not discriminate on the basis of race, color, age, religion, national origin, sexual orientation, gender identity, sex, marital status, disability, or status as a U.S. veteran. Inquiries can be directed to the Director of Equal Opportunity and Diversity, (515) 294-7612.

ACCELERATED IMPLEMENTATION OF INTELLIGENT COMPACTION TECHNOLOGY FOR EMBANKMENT SUBGRADE SOILS, AGGREGATE BASE, AND ASPHALT PAVEMENT MATERIALS: US 12 MARMARTH, NORTH DAKOTA

Final Report ER10-08
US12, ND Field Project
August 9 to 12, 2010

Prepared By

David J. White, Ph.D.
Pavana KR. Vennapusa, Ph.D.
Heath Gieselman, M.S.
Jiake Zhang, M.S.
Michael Eidem

Earthworks Engineering Research Center (EERC)
Department of Civil Construction and Environmental Engineering
Iowa State University
2711 South Loop Drive, Suite 4600
Ames, IA 50010-8664
Phone: 515-294-7910
www.eerc.iastate.edu

November 10, 2010

About the EERC

The mission of the Earthworks Engineering Research Center at Iowa State University is to be the nation's premier institution for developing fundamental knowledge of earth mechanics, and creating innovative technologies, sensors, and systems to enable rapid, high quality, environmentally friendly, and economical construction of roadways, aviation runways, railroad embankments, dams, structural foundations, fortifications constructed from earth materials, and related geotechnical applications.

Disclaimer Notice

The contents of this report reflect the views of the authors, who are responsible for the facts and the accuracy of the information presented herein. The opinions, findings and conclusions expressed in this publication are those of the authors and not necessarily those of the sponsors.

The sponsors assume no liability for the contents or use of the information contained in this document. This report does not constitute a standard, specification, or regulation.

The sponsors do not endorse products or manufacturers. Trademarks or manufacturers' names appear in this report only because they are considered essential to the objective of the document.

Non-discrimination Statement

Iowa State University does not discriminate on the basis of race, color, age, religion, national origin, sexual orientation, gender identity, sex, marital status, disability, or status as a U.S. veteran. Inquiries can be directed to the Director of Equal Opportunity and Diversity, (515) 294-7612.

TABLE OF CONTENTS

LIST OF FIGURES

LIST OF TABLES

ACKNOWLEDGMENTS

This study was funded by Federal Highway Administration under the pooled fund contract DTFH61-07-C-R0032 for a research project titled "*Accelerated Implementation of Intelligent Compaction Technology for Embankment Subgrade Soils, Aggregate Base, and Asphalt Pavement Materials*". George Chang from the Transtec Group, Inc. is the Principal Investigator for this research project. Robert D. Horan is the project facilitator and assisted with scheduling rollers for the project. Caterpillar Inc. provided the IC rollers. Mario Souraty and Candice Young from Caterpillar, Inc. provided field support on the IC rollers. Jon Ketterling, Jason Fischer, Greg Wolter, Matt Kurle, Matt Dietrich, Dallan Fiest, and Harry Wolbaum with North Dakota Department of Transportation (DOT) provided assistance with field testing. Northern Improvement Company and Gratech personnel provided assistance with preparation of the test beds. All their assistance and interest is greatly appreciated.

LIST OF SYMBOLS AND ABBREVIATIONS

a	Theoretical vibration amplitude (eccentric moment divided by the drum mass)
A_Ω	Acceleration at fundamental frequency
$A_{2\Omega}$	Acceleration of the first harmonic component of the vibration
$A_{0.5\Omega}$	Subharmonic acceleration amplitude caused by jumping
A	Sample cross-sectional area
A’	Machine acceleration
b	Machine internal loss coefficient used in MDP calculation
b_0	Intercept in a linear regression equation
b_1, b_2, b_3	Regression coefficients
c’	Effective cohesion
B	Contact width of the drum
BST	Bore hole shear test
CBR	California bearing ratio
CBR_{200}	Weighted average CBR to a depth of 200 mm
CBR_{250}	Weighted average CBR to a depth of 250 mm
CMV	Compaction meter value
COV	Coefficient of variation (calculated as the ratio of mean and standard deviation)
c_c	Coefficient of curvature
c_u	Coefficient of uniformity
DPI	Dynamic cone penetration index
d_0	Measured settlement under the plate
D_{10}	Particle size corresponding to 10% passing
D_{30}	Particle size corresponding to 30% passing
D_{60}	Particle size corresponding to 60% passing
E	Elastic modulus
E_{LWD-Z2}	Elastic modulus determined from 200-mm plate Zorn light weight deflectometer
E_{LWD-Z3}	Elastic modulus determined from 300-mm plate Zorn light weight deflectometer
E_{FWD-K3}	Elastic modulus determined from 300-mm plate KUAB falling weight deflectometer
E_{FWD-D3}	Elastic modulus determined from 300-mm plate Dynatest falling weight deflectometer
f	Vibration frequency
F	Shape factor
g	Acceleration of gravity
G_s	Specific gravity
GPS	Global positioning system
h	Separation distance
H	Sample height at any gyration cycle
IC-MV	Intelligent compaction measurement value
LL	Liquid limit
m	Machine internal loss coefficient used in MDP calculation
MDP	Caterpillar Machine drive power
MDP*	MDP* value rescaled to range between 1 and 150 (see description in text)
MV	Measurement value

NG	Nuclear gauge
n	Number of test measurements
p	Number of regression parameters
P_g	Gross power needed to move the machine
PDA	Pressure distribution analyzer
PI	Plasticity index
PL	Plastic limit
Point-MV	In-situ point measurement value
r	Radius of the plate
R	Semivariogram range
R'	Resultant force
R^2	Coefficient of determination
RMV	Resonant meter value
v	Roller velocity
w	Moisture content determined from Humboldt nuclear gauge
w_{opt}	Optimum moisture content
W	Roller weight
ZAV	Zero air void
ϕ'	Effective angle of internal friction
μ	Statistical mean
σ	Statistical standard deviation
σ_0	Applied vertical stress
τ_G	Frictional or shear resistance calculated from PDA
η	Poisson's ratio
γ_d	Dry unit weight determined from Humboldt nuclear gauge (NG)
γ_{dmax}	Maximum dry unit weight
$\gamma(h)$	Semivariogram

INTRODUCTION

This report presents results from a field investigation conducted on US Highway 12 in Marmarth, North Dakota. The machine configurations and roller-integrated measurement systems used on this project included: a Caterpillar CP56 smooth drum roller with a padfoot shell kit (here after referred to as padfoot roller) equipped with machine drive power (MDP), and a Caterpillar CS563E vibratory smooth drum roller equipped with MDP and compaction meter value (CMV) intelligent compaction (IC) measurement technologies. The machines were equipped with real time kinematic (RTK) global positioning system (GPS) and on-board display and documentation systems. The project involved construction and testing of seven test beds. Four of these test beds included silty subgrade materials and the remaining three included salvage base materials. The test beds with salvage base materials varied in terms of their underlying support conditions. One test bed was reinforced with two layers of geogrid in the base layers, one test bed was partially treated with over excavation and replacement due to soft subgrade conditions, and the other test bed served as a control section with no special treatments.

The IC measurement values (IC-MVs) were evaluated by conducting field testing in conjunction with a variety of in-situ testing devices measuring density, moisture content, California bearing ratio (CBR), shear strength, elastic modulus. An open house was conducted near the end of the field investigation to disseminate results from current and previous IC projects. The North Dakota department of transportation (NDDOT), contractor's personnel, and representatives from the IC roller manufacturers participated in the field testing phase of the project and the open house.

The goals of this field investigation were similar to previous demonstration projects and included the following:

- document machine vibration amplitude influence on compaction efficiency,
- develop correlations between IC-MVs to traditional in-situ point measurements (point-MVs),
- evaluate the impact of geogrid reinforcement in the base layers on IC-MVs and point-MVs in comparison with sections without reinforcement,
- compare IC results to traditional compaction operations,
- study IC measurement values in production compaction operations, and
- evaluate IC measurement values in terms of alternative specification options.

This report presents brief background information for the two IC-MVs evaluated in this study (MDP and CMV), documents the results and analysis from the laboratory and field testing, and documents the field demonstration activities. Regression analysis was performed to evaluate correlations between IC-MVs and in-situ compaction measurements determined using point-MVs. Dry density and moisture content measurements were obtained using a calibrated Humboldt nuclear gauge, modulus measurements were obtained using Zorn light weight deflectometers (LWDs) setup with 300 mm and 200 mm diameter plates, a Dynatest falling weight deflectometer (FWD) setup with 300 mm diameter plate, a KUAB FWD setup with 300 mm diameter plate, and a in-situ bore hole shear test (BST) device. The BST device was used to evaluate the soil shear strength properties. Geostatistical methods were used to quantify and

characterize spatial non-uniformity of the subgrade materials using spatially referenced IC-MV data. All IC-MVs and point-MVs were recorded with real time kinematic (RTK) global positioning system (GPS) measurements.

Empirical correlations between IC-MVs and in-situ point-MVs are first evaluated independently for each test bed which were sometimes obtained over a narrow measurement range and then combined to develop site wide correlations capturing a wide measurement range. The results and correlations provided in this report should be of significant interest to the pavement, geotechnical, and construction engineering community and are anticipated to serve as a good knowledge base for implementation of IC compaction monitoring technologies and various new in-situ testing methods into earthwork construction practice.

BACKGROUND

Caterpillar CS56 smooth drum with a padfoot shell kit and Caterpillar CS563E vibratory smooth drum IC rollers were used on the project (Figure 1). A digital display unit employing proprietary software is mounted in the roller cabin for on-board visualization of roller position, IC-MVs, coverage information, amplitude/frequency settings, speed, etc. The rollers were outfitted with a real-time kinematic (RTK) global positioning system (GPS) to continuously record the roller position information. Some key features of the rollers are summarized in Table 1. The padfoot roller (CS56) recorded machine drive power (MDP), while the smooth drum roller (CS563E) recorded machine drive power (MDP) and compaction meter value (CMV). Brief descriptions of these IC-MVs are provided in the following discussion.

Table 1. Key features of the IC rollers used on the project

Feature	Caterpillar CS56 and CS563
Drum Type	CS56 – Padfoot shell kit over smooth drum CS563E – Smooth drum
Frequency (f)	30 Hz
Amplitude (a) Settings	Static, 0.90 mm (low amplitude), and 1.80 mm (high amplitude)
IC-MV	MDP_{40} (shown as CCV in the output), and Geodynamik CMV and RMV
Display Software	AccuGrade™ office
GPS coordinates	Based on local arbitrary coordinates at the base station
Output Documentation	Date/Time, Location (Northing/Easting/Elevation of left and right ends of the roller drum), Speed, CCV, CMV, RMV, Frequency, Amplitude (theoretical), Direction (forward/ backward), Vibration (On/Off)
Data frequency	About every 0.2 m at the center of the drum (for a nominal v = 4 km/h)
Output Export File	*.csv
Automatic Feedback Control (AFC)[a]	No

[a]AFC mode involves automatic adjustment of vibration amplitude and/or frequency during compaction.

Figure 1. Caterpillar CS56 smooth drum with padfoot shell kit (top) and Caterpillar CS563E smooth drum (bottom) IC rollers used on the project

Machine Drive Power (MDP) Value

MDP technology relates mechanical performance of the roller during compaction to the properties of the compacted soil. Detailed background information on the MDP system is provided by White et al. (2005). Controlled field studies documented by White and Thompson (2008), Thompson and White (2008), and Vennapusa et al. (2009) verified that MDP values are empirically related to soil compaction characteristics (e.g., density, stiffness, and strength). MDP is calculated using Eq. 1.

$$MDP = P_g - Wv\left(\text{Sin}\alpha + \frac{A'}{g}\right) - (mv + b) \quad (1)$$

Where MDP = machine drive power (kJ/s), P_g = gross power needed to move the machine (kJ/s), W = roller weight (kN), A' = machine acceleration (m/s^2), g = acceleration of gravity (m/s^2), α = slope angle (roller pitch from a sensor), *v* = roller velocity (m/s), and m (kJ/m) and b (kJ/s) = machine internal loss coefficients specific to a particular machine (White et al. 2005). MDP is a relative value referencing the material properties of the calibration surface, which is generally a hard compacted surface (MDP = 0 kJ/s). Positive MDP values therefore indicate material that is less compact than the calibration surface, while negative MDP values indicate material that is more compacted than the calibration surface (i.e. less roller drum sinkage). The MDP values obtained from the machine were recalculated to range between 1 and 150 and these re-scaled values are referred to as MDP* in this report. While the original MDP values decrease in increasing compaction, the MDP* values increase with increasing compaction.

Compaction Meter Value (CMV) and Resonant Meter Value (RMV)

CMV is a dimensionless compaction parameter developed by Geodynamik (http://www.geodynamik.com/languages/english/index_gb.html) that depends on roller dimensions, (i.e., drum diameter and weight) and roller operation parameters (e.g., frequency, amplitude, speed), and is determined using the dynamic roller response (Sandström 1994). It is calculated using Eq. 3, where C is a constant (300), $A_{2\Omega}$ = the acceleration of the first harmonic component of the vibration, A_{Ω} = the acceleration of the fundamental component of the vibration (Sandström and Pettersson 2004). Correlation studies relating CMV to soil dry unit weight, strength, and stiffness are documented in the literature (e.g., Floss et al. 1983, Samaras et al. 1991, Brandl and Adam 1997, Thompson and White 2008, White and Thompson 2008).

$$CMV = C \cdot \frac{A_{2\Omega}}{A_{\Omega}} \quad (3)$$

RMV provides an indication of the drum behavior (e.g. continuous contact, partial uplift, double jump, rocking motion, and chaotic motion) and is calculated using Eq. 4, where $A_{0.5\Omega}$ = subharmonic acceleration amplitude caused by jumping (the drum skips every other cycle). It is important to note that the drum behavior affects the CMV measurements (Brandl and Adam 1997) and therefore must be interpreted in conjunction with the RMV measurements (Vennapusa et al. 2010).

$$RMV = C \cdot \frac{A_{0.5\Omega}}{A_{\Omega}} \quad (4)$$

Earthwork Compaction Specifications

The subgrade and base materials were placed and constructed in accordance with Section 203.02G of the North Dakota DOT Standard Specifications. The fill material was required to be compacted to at least 90% of the AASHTO T-180 maximum dry unit weight. The moisture

content of the soil at the time of compaction shall be not less than the optimum moisture content and no more than 5% above the AASHTO T-180 optimum moisture content.

ANALYSIS METHODS

Regression Analysis

Simple linear and non-linear regression relationships between IC-MVs and in-situ point-MVs were developed by spatially pairing the data obtained from the test beds using GPS measurements. The analysis was performed by considering point-MVs as "true" independent variables and IC-MVs as dependent variables using the models shown in Eqs. 7 and 8, where b_0 = intercept and b_1, b_2 = regression parameters.

$$\text{Linear model: } IC\text{–}MV = b_0 + b_1 \cdot Point\ MV \tag{7}$$

$$\text{Non-linear power model: } IC\text{–}MV = b_1 (Point\ MV)^{b_2} \tag{8}$$

Statistical significance of the independent variable was assessed based on *p*- and *t*-values. The selected criteria for identifying the significance of a parameter included: *p*-value < 0.05 = significant, < 0.10 = possibly significant, > 0.10 = not significant, and *t*-value < -2 or > +2 = significant. The best fit model is determined based on the strength of the regression relationships assessed by the coefficient of determination (i.e., R^2) values. For the analysis and discussion in this report, an R^2 value ≥ 0.5 is considered acceptable following the guidelines from European specifications. A statistical prediction interval approach for determining "target" values from the regression relationships would account for R^2 values in the relationships (see NCHRP 21-09, 2010). A regression relationship with lower R^2 values would result in higher target value and a regression relationship with higher R^2 value will result in lower target values.

Geostatistical Analysis

Spatially referenced IC measurement values provide an opportunity to quantify "non-uniformity" of compacted fill materials. Vennapusa et al. (2010) demonstrated the use of semivariogram analysis in combination with conventional statistical analysis to evaluate non-uniformity in QC/QA during earthwork construction. A semivariogram is a plot of the average squared differences between data values as a function of separation distance, and is a common tool used in geostatistical studies to describe spatial variation. A typical semivariogram plot is presented in Figure 2. The semivariogram $\gamma(h)$ is defined as one-half of the average squared differences between data values that are separated at a distance h (Isaaks and Srivastava 1989). If this calculation is repeated for many different values of h (as the sample data will support) the result can be graphically presented as experimental semivariogram shown as circles in Figure 2. More details on experimental semivariogram calculation procedure are available elsewhere in the literature (e.g., Clark and Harper 2002, Isaaks and Srivastava 1989).

To obtain an algebraic expression for the relationship between separation distance and experimental semivariogram, a theoretical model is fit to the data. Some commonly used models include linear, spherical, exponential, and Gaussian models. A spherical model was used for data analysis in this report. Arithmetic expression of the spherical model and the spherical

variogram are shown in Figure 2. Three parameters are used to construct a theoretical semivariogram: sill ($C+C_0$), range (R), and nugget (C_0). These parameters are briefly described in Figure 2. More discussion on the theoretical models can be found elsewhere in the literature (e.g., Clark and Harper 2002, Isaaks and Srivastava 1989). For the results presented in this section, the sill, range, and nugget values during theoretical model fitting were determined by checking the models for "goodness" using the modified Cressie goodness fit method (see Clark and Harper 2002) and cross-validation process (see Isaaks and Srivastava 1989). From a theoretical semivariogram model, a low "sill" and longer "range of influence" represent best conditions for uniformity, while the opposite represents an increasingly non-uniform condition.

Some of the results presented in this report revealed nested structures with short-range and long-range components in the experimental semivariograms. Nested structures have been observed in geological applications where different physical processes are responsible for spatial variations at different scale (see Chiles and Delfiner 1999). For the cases with nested structures, nested spherical variograms combining two spherical models (with two sill values and two range values) are fit to the experimental semivariogram data. Previous field studies in New York and Mississippi conducted as part of this research also revealed similar nested structures.

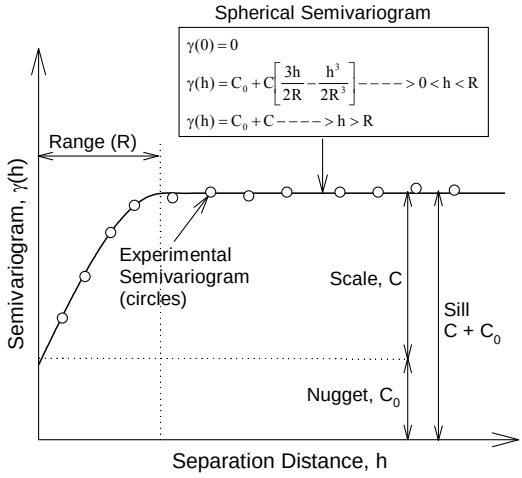

Range, R: As the separation distance between pairs increase, the corresponding semivariogram value will also generally increase. Eventually, however, an increase in the distance no longer causes a corresponding increase in the semivariogram, i.e., where the semivariogram reaches a plateau. The distance at which the semivariogram reaches this plateau is called as range. Longer range values suggest greater spatial continuity or relatively larger (more spatially coherent) "hot spots".

Sill, $C+C_0$: The plateau that the semivariogram reaches at the range is called the sill. A semivariogram generally has a sill that is approximately equal to the variance of the data.

Nugget, C_0: Though the value of the semivariogram at h = 0 is strictly zero, several factors, such as sampling error and very short scale variability, may cause sample values separated by extremely short distances to be quite dissimilar. This causes a discontinuity at the origin of the semivariogram and is described as nugget effect. (Isaaks and Srivastava, 1989)

Figure 2. Description of a typical experimental and spherical semivariogram and its parameters

EXPERIMENTAL TESTING

Description of Test Beds

A total of seven test beds with one subgrade material and one base material were constructed and tested as part of this study. A summary of test beds with material conditions and tests performed is provided in Table 2. A summary of material index properties is provided in Table 3. Details regarding construction and testing of each test bed are provided in the discussion later in this report.

Table 2. Summary of test beds and in-situ testing

TB	Description	Material	Date	Machine	Total Passes	Amp. (mm)*, Speed (km/h)**	In-situ Point Measurements
1	Calibration Test Strip (lane 1)	Subgrade	08/09	Padfoot	16	Static, 3.2	$E_{LWD\text{-}Z2}$, γ_d, w, and CBR
	Calibration Test Strip (lane 1)			Padfoot	16	0.90, 3.2	$E_{LWD\text{-}Z2}$, γ_d, w, and CBR
	Calibration Test Strip (lane 3)			Padfoot	16	1.80, 3.2	$E_{LWD\text{-}Z2}$, γ_d, w, and CBR
2	Test Strip	Subgrade	0809	Padfoot	1	0.90, 3.2	—
3	Production Area Compaction	Subgrade	08/09	Padfoot	9	Static, 4.0	
	Production Area Mapping			Padfoot	1	Static, 3.2	
				Padfoot	1	0.90, 3.2	
	Production Area Leveling/ Sealing			Pneumatic	2	—	$E_{LWD\text{-}Z2}$ and CBR
4	Production Area (TX5 geogrid placed over subgrade and base layer 1)	Existing Subgrade	08/10	—	—	—	$E_{LWD\text{-}Z3}$, CBR, $E_{FWD\text{-}D3}$ and $E_{FWD\text{-}K3}$
		Base Layer 1	08/10	Smooth Drum	6 (forward and reverse)	Forward: 0.90, 3.2 Reverse: Static, 6.0	$E_{LWD\text{-}Z3}$, γ_d, w $E_{FWD\text{-}D3}$ and $E_{FWD\text{-}K3}$
		Base Layer 2	08/10	Smooth Drum	6 (forward and reverse)	Forward: 0.90, 3.2 Reverse: Static, 6.0	$E_{LWD\text{-}Z3}$, CBR, BST, $E_{FWD\text{-}D3}$, and $E_{FWD\text{-}K3}$
5-1	Production Area (no geogrid)	Base Layer 2	08/10	Smooth Drum	1	0.90, 3.2	—
5-2	Production Area (no geogrid) After Trafficking	Base Layer 2	08/11	Smooth Drum	1	0.90, 3.2	$E_{LWD\text{-}Z3}$ and $E_{FWD\text{-}K3}$
6	Production Area (Core out and replacement in the subgrade)	Existing Subgrade	08/10	Smooth Drum	1	0.90, 3.2	$E_{LWD\text{-}Z3}$, $E_{FWD\text{-}K3}$, CBR (DCP before and after core out), BST
		Base Layer 2	08/10	Smooth Drum	1	0.90, 3.2	$E_{LWD\text{-}Z3}$, $E_{FWD\text{-}K3}$, and CBR
7	Production Area Compaction	Subgrade	08/11	Padfoot	4 to 5	Static, 4.0	—
	Production Area Mapping	Subgrade	08/11	Padfoot	1	Static, 3.2	γ_d, w, and CBR

Notes: TB – test bed, *theoretical amplitude, **nominal, w – moisture content, γ_d – dry unit weight, CBR – California bearing ratio determined from DCP test, $E_{LWD\text{-}Z2}$ – elastic modulus determined using 200 mm diameter plate Zorn LWD, $E_{LWD\text{-}Z3}$ – elastic modulus determined using 300 mm diameter plate Zorn LWD, $E_{FWD\text{-}D3}$ – elastic modulus determined using 300 mm diameter plate Dynatest FWD test, $E_{FWD\text{-}K3}$ – elastic modulus determined using 300 mm diameter plate KUAB FWD; BST – bore hole shear test

Laboratory Testing

Laboratory testing was performed on the silty subgrade and salvage base materials obtained from the project. Testing involved conducting grain size analysis and Atterberg limits tests to classify the materials in accordance with the unified soil classification system (USCS) and the American association of state highway and transportation officials (AASHTO) system, and conducting laboratory Proctor and gyratory compaction tests.

A summary of the material index properties is provided in Table 3. Grain size distribution curves of the two materials are presented in Figure 3. Results from laboratory standard (AASHTO T-99) and modified (AASHTO T-180) Proctor tests on subgrade and base materials are shown in Figure 4 and Figure 5, respectively. Maximum dry unit weight (γ_{dmax}) and optimum moisture content (w_{opt}) results from the Proctor tests are summarized in Table 3. Gyratory compaction tests were conducted on the base material using AFGB1A Brovold gyratory compactor shown in Figure 6 (manufactured by Pine Instrument Company). A pressure distribution analyzer (PDA) as shown in Figure 6 was installed above the sample in the gyratory compaction mold to capture the pressure distribution across the sample during compaction. PDA is described in detail elsewhere in the literature (e.g., Guler et al. 2000, White et al. 2009). In brief, the PDA consists of three pressure transducers which are used to output the total resultant force (R) and eccentricity (e) at which the resultant force occurs for each gyration. The R and e measurements can be used to calculate frictional resistance or shear resistance (τ_G) of the compaction material using Eq. 9:

$$\tau_G = \frac{R' \cdot e}{A \cdot H} \tag{9}$$

where R' = resultant force, e = eccentricity, A = sample cross-sectional area, and H = sample height at any gyration cycle. A previous study by White et al. (2009) indicated that the τ_G values determined from the PDA can be correlated to resilient modulus and undrained shear strength properties.

Gyratory compaction tests were conducted on the base material at its natural moisture content (w = 5.0%). The material was thoroughly mixed and loosely placed into the gyratory compaction mold, the PDA was installed above the sample, a controlled vertical stress (σ_o = 300, 600, and 900 kPa) was applied to both the top and bottom of the sample, and compacted using 100 gyrations at a constant gyration rate (gyrations per minute = 30). A gyration angle of 1.25 degrees was used to compact the material. The H, R', and e values were recorded for each gyration cycle to determine γ_d and τ_G.

Results from gyratory compaction tests are presented in Figure 7 which shows γ_d and τ_G compaction curves for σ_o = 300, 600, and 900 kPa. The maximum γ_d and the maximum τ_G (i.e., after 100 gyrations) values for each applied stress condition are summarized in Table 3. The γ_d compaction curves indicate that σ_o = 600 kPa results in γ_d similar to the AASHTO T-180 γ_{dmax} after 100 gyrations. 90% of AASHTO T-180 γ_{dmax} was achieved at 12 gyrations using σ_o = 300 kPa, and at 5 gyrations using σ_o = 600 and 900 kPa.

Table 3. Summary of material index properties and laboratory test results

Parameter	Subgrade	Base
Material Description	Greenish Gray Silty Sand	Olive Gray Poorly Graded Sand with Gravel
Grain-Size Analysis Results (ASTM D422-63; C136-06)		
Gravel Content (%) (> 4.75mm)	2.4	36.2
Sand Content (%) (4.75mm – 75μm)	65.0	62.8
Silt Content (%) (75μm – 2μm)	21.7	1.0
Clay Content (%) (< 2μm)	10.9	
D_{10} (mm)	0.002	0.362
D_{30} (mm)	0.067	1.025
D_{60} (mm)	0.142	4.002
Coefficient of Uniformity, c_u	87.3	11.1
Coefficient of Curvature, c_c	19.7	0.7
Atterberg Limits Test Results (ASTM D4318-05)		
Liquid Limit, LL (%)	31	NP
Plastic Limit, PL (%)	22	
AASHTO Classification (ASTM D3282-09)	A-2-4	A-1-a
USCS Classification (ASTM D2487-00)	SM	GM
Specific Gravity, G_s (Assumed)	2.70	2.70
Standard Proctor Test Results (AASHTO T-99)		
γ_{dmax} (kN/m^3, pcf)	16.97, 108.0	20.56, 130.9
w_{opt}	17.0	9.2
Modified Proctor Test Results (AASHTO T-180)		
γ_{dmax} (pcf)	18.85, 120.0	21.41, 136.3
w_{opt}	12.0	7.8
Gyratory Compaction Test and PDA Results (at 100 gyrations)		
γ_{dmax} (kN/m^3, pcf) at σ_o = 300 kPa	Not performed	20.67, 131.6
γ_{dmax} (kN/m^3, pcf) at σ_o = 600 kPa		21.41, 136.3
γ_{dmax} (kN/m^3, pcf) at σ_o = 900 kPa		21.69, 138.1
τ_G (kPa, psf) at σ_o = 300 kPa		84.8, 1772
τ_G (kPa, psf) at σ_o = 600 kPa		186.4, 3894
τ_G (kPa, psf) at σ_o = 900 kPa		443.9, 9271

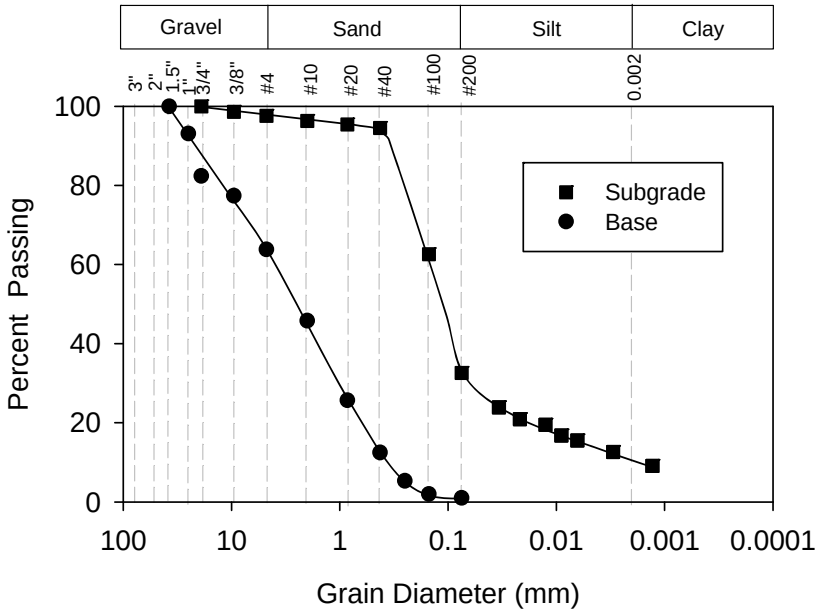

Figure 3. Grain-size distribution curves of subgrade and base materials

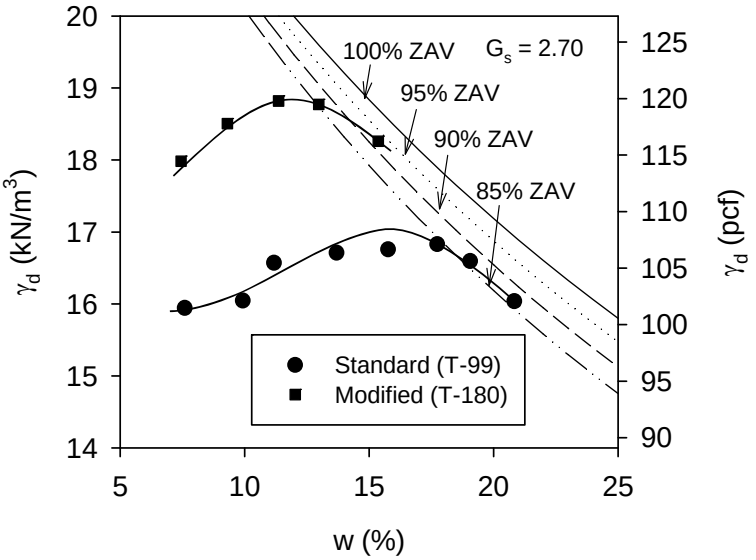

Figure 4. Laboratory Proctor test results for subgrade material

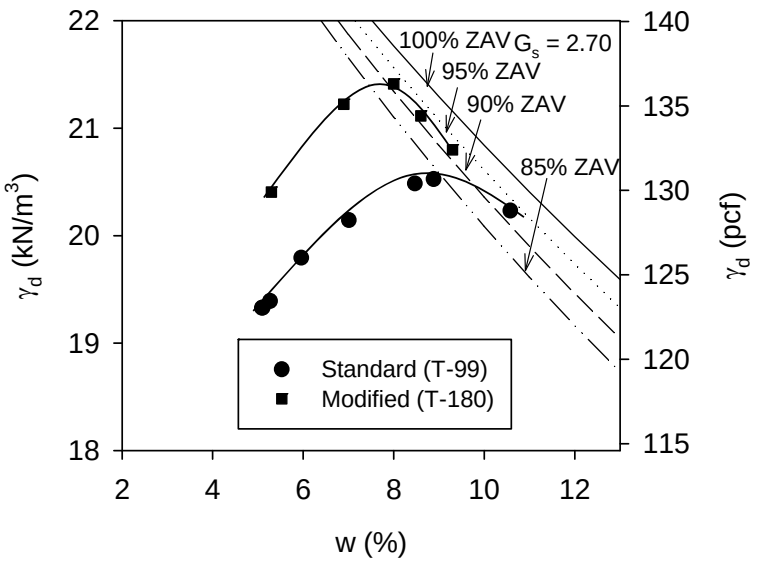

Figure 5. Laboratory Proctor test results for base material

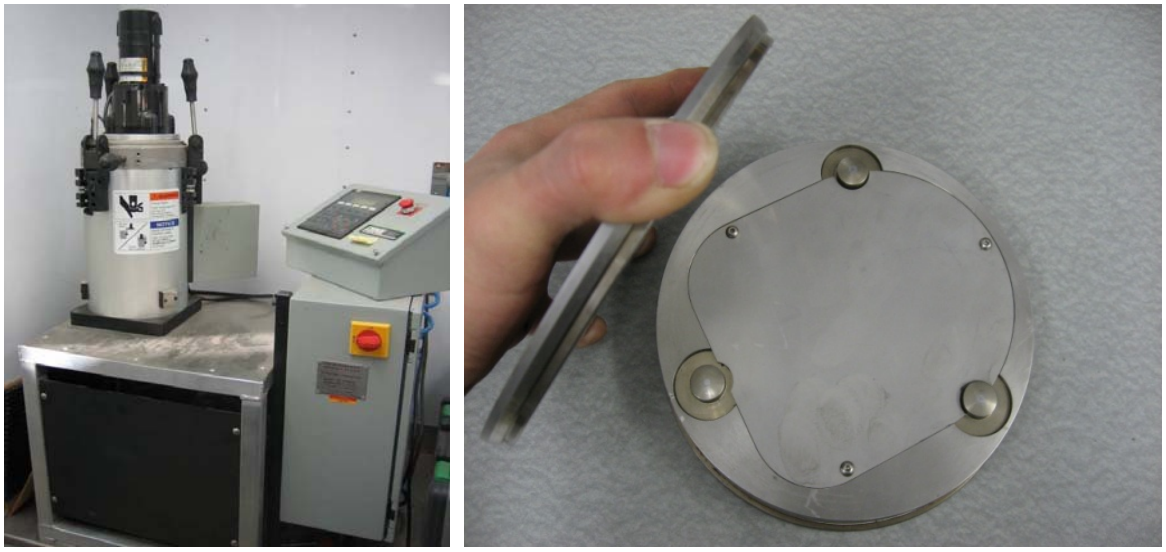

Figure 6. AFGB1A gyratory compactor (left) and pressure distribution analyzer (PDA, right)

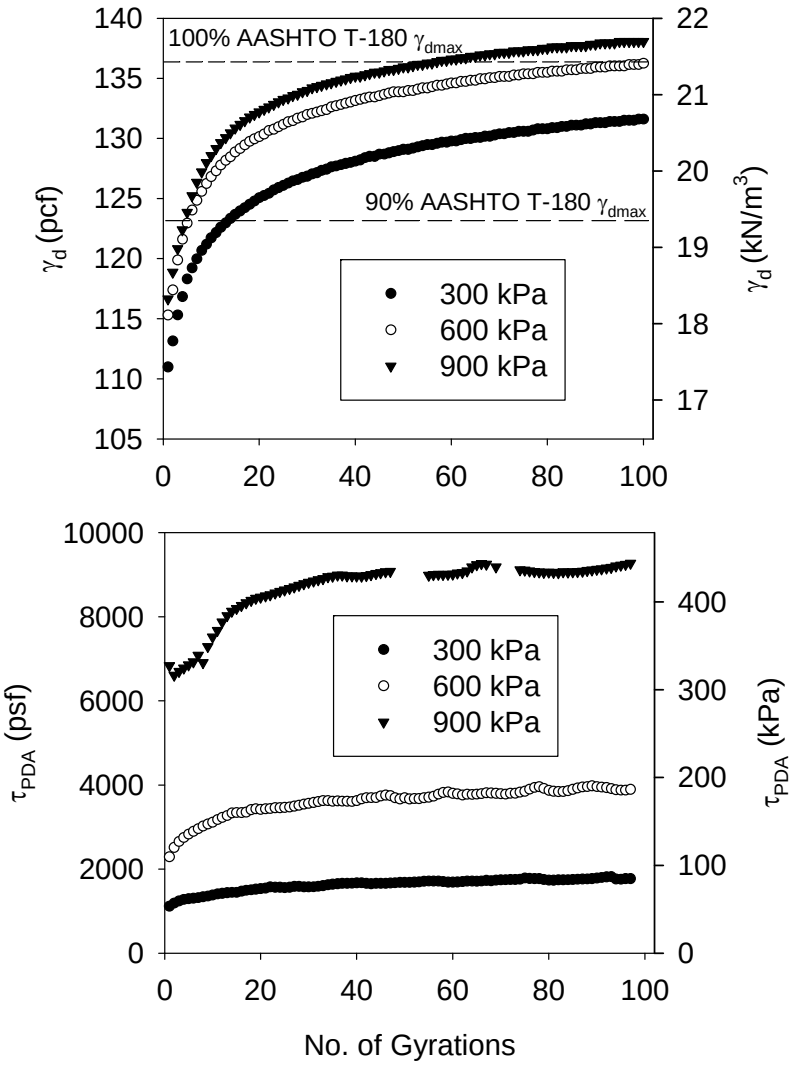

Figure 7. Dry unit weight and PDA shear resistance compaction curves from gyratory compaction test on base material

In-situ Testing Methods

Six different in-situ testing methods were used in this study to evaluate the in-situ soil engineering properties (Figure 8): (a) Zorn light weight deflectometer setup with 200 and 300 mm diameter plates to determine elastic modulus ($E_{LWD\text{-}Z2}$ for 200 mm plate diameter and $E_{LWD\text{-}Z3}$ for 300 mm plate diameter), (b) dynamic cone penetrometer (DCP) to determine California bearing ratio (CBR), (c) calibrated Humboldt nuclear gauge (NG) to measure moisture content (w) and dry unit weight (γ_d), (d) Dynatest falling weight deflectometer (FWD) setup with 300 mm diameter plate to determine elastic modulus ($E_{FWD\text{-}D3}$), (e) Kuab falling weight deflectometer (FWD) setup with 300 mm diameter plate to determine elastic modulus ($E_{FWD\text{-}K3}$), and (f) insitu bore hole shear test (BST) to determine soil drained shear strength properties.

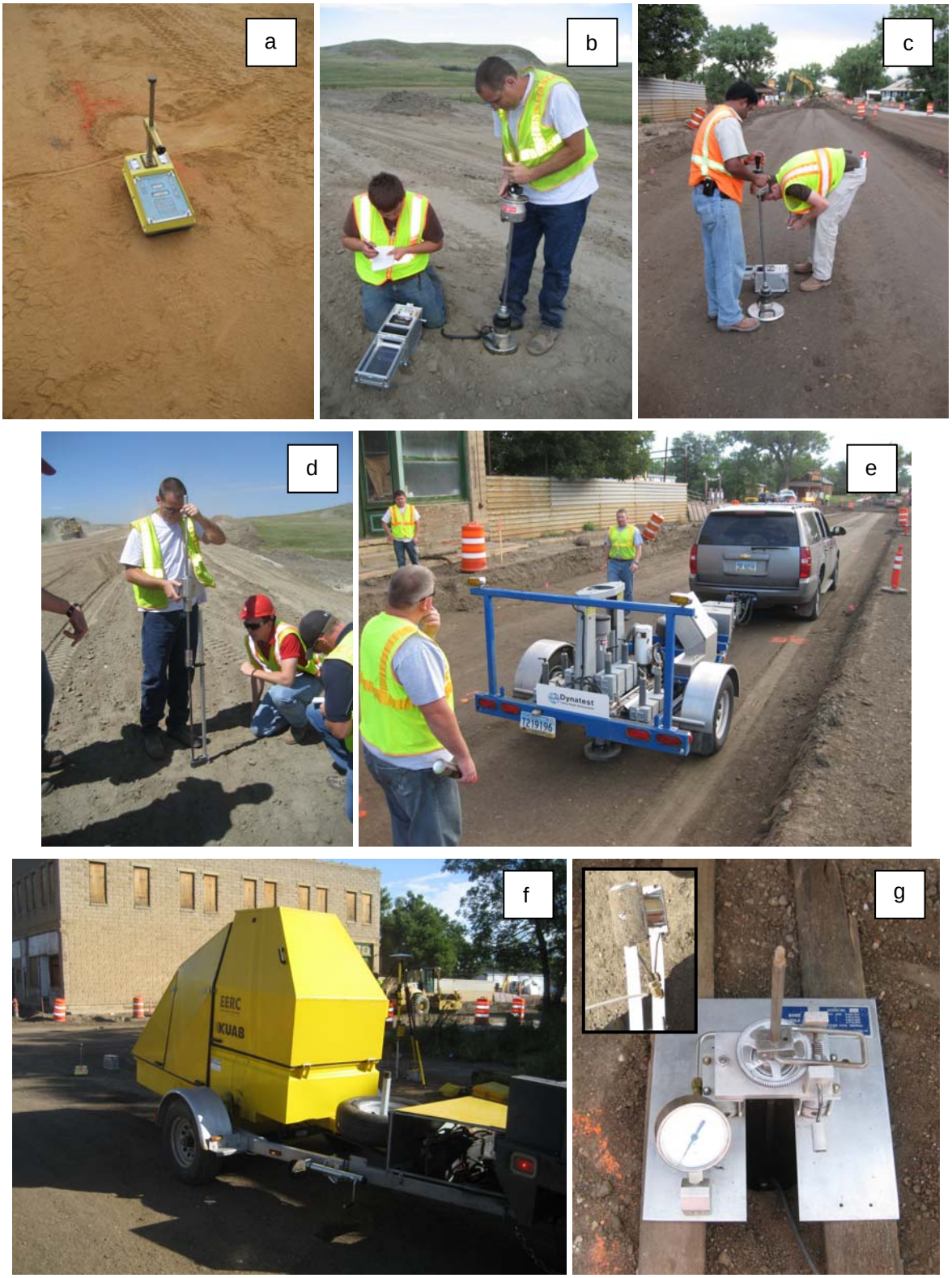

Figure 8. In-situ testing methods used on the project: (a) Humboldt nuclear gauge, (b) 200 mm Zorn LWD, (c) 300 mm Zorn LWD, (d) dynamic cone penetrometer, (e) Dynatest FWD, (f) KUAB FWD, (g) Iowa BST (expandable contact plates shown in the insert)

LWD tests were performed following manufacturer recommendations (Zorn 2003) and the E_{LWD} values were determined using Eq. 10, where E = elastic modulus (MPa), d_0 = measured settlement (mm), η = Poisson's ratio (0.4), σ_0 = applied stress (MPa), r = radius of the plate (mm), F = shape factor depending on stress distribution (assumed as 8/3) (see Vennapusa and White 2009). The results are reported as $E_{LWD\text{-}Z3}$ (Z represents Zorn LWD and 3 represents 300 mm diameter plate).

$$E = \frac{(1-\eta^2)\sigma_0 r}{d_0} \times F \tag{10}$$

Dynatest FWD testing was performed by applying one seating drop and two test drops each using a nominal force of about 31 kN (7000 lbf). Kuab FWD testing was performed by applying one seating drop using a nominal force of about 29 kN (6500 lbf) followed by two test drops each at a nominal force of about 42 kN (9500 lbf) and 56 kN (12500 lbf). The actual applied force for both FWDs was recorded using a load cell. The deflections were measured at the centre of the plate and at 152, 305, 357, 610, 914, 1219, and 1524 mm offsets from the centre of the plate. A composite modulus value ($E_{FWD\text{-}D3}$ using Dynatest FWD and $E_{FWD\text{-}K3}$ using Kuab FWD) was calculated using the measured deflection at the center of the plate, corresponding applied contact force, and Eq. 10. F = 8/3 was assumed in the calculations similar to LWD calculations for the Dynatest FWD. F = 2 was assumed in the calculations for the KUAB FWD as the plate used was a four-segmented plate and the contact stress distribution was assumed to be uniform.

DCP tests were performed in accordance with ASTM D6951-03 to determine dynamic cone penetration index (DPI) and calculate CBR using Eq. 11. The DCP test results are presented in this report as CBR point values or CBR depth profiles. When the data is presented as point values, the data represents a weighted average CBR of depth indicated in the subscript (e.g., CBR_{200} indicates weighted average CBR to a depth of 200 mm).

$$CBR = \frac{292}{DPI^{1.12}} \tag{11}$$

In situ borehole shear tests (BSTs) were performed in a bore hole at various depths in the compacted base and subgrade layers to determine their drained shear strength properties. BST is described elsewhere in the literature (see Handy and Fox 1967, Handy et al. 1985). In brief, the test involves: (a) drilling a bore hole, (b) inserting two curved contact plates (see Figure 8g) into the bore hole to a desired depth, (c) applying a normal pressure by expanding the plates inside the hole, and (d) applying a shearing stress by pulling the expanded contact plates until a peak value is reached. The test was performed by applying three different applied normal pressures (50, 100, and 150 kPa) at each test location. The test essentially represents a direct shear test on a soil. A constant normal stress was applied on the soil for about 5 minutes. If the normal stresses did not change during that time, it was assumed that consolidation is complete and then shearing stresses were applied. A normal stress versus peak shearing stress plot is generated from the data

to determine effective cohesion (c') and drained angle of internal friction (ϕ') parameters as illustrated in Figure 9.

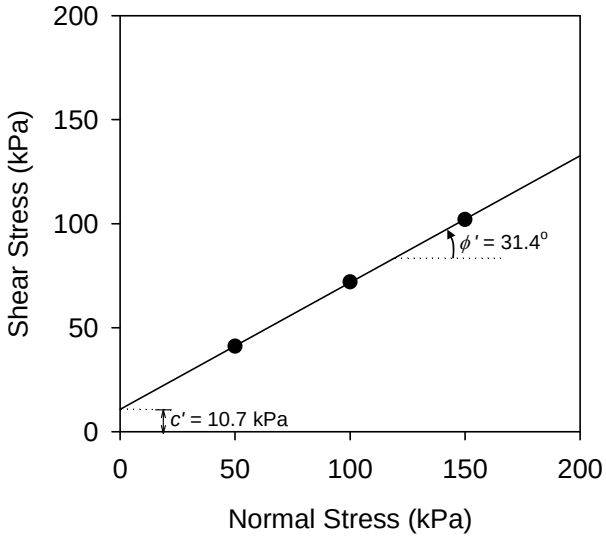

Figure 9. Illustration of shear strength parameter determination from Iowa borehole shear test (results obtained from TB4)

The Iowa State University Geotechnical mobile laboratory (Figure 10) is equipped with Davis Vantage Pro weather station with a Weatherlink datalogger system. Weather data was monitored and recorded every 30 minutes by the datalogger. Air temperature and wind speed recorded during the course of the project are presented in Figure 11. Approximate time of construction and testing of different test beds is shown in Figure 11.

Figure 10. Iowa State University geotechnical mobile laboratory

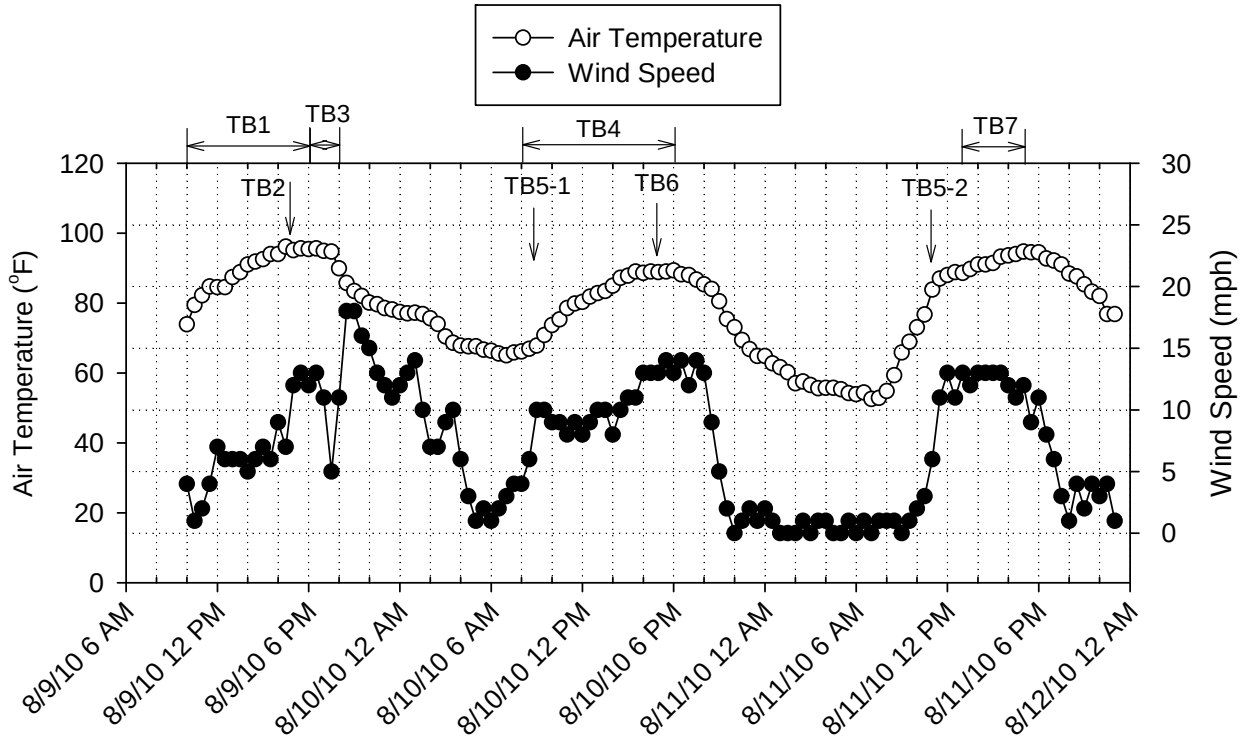

Figure 11. Air temperature and wind speed data

EXPERIMENTAL TEST RESULTS

TB1 Subgrade Calibration Test Strips (Padfoot Roller)

Test beds construction and in-situ testing (Lanes 1, 2, and 3)

TB1 consisted of silty subgrade material scarified to approximately 220 to 270 mm depth using a motor grader. The material was initially wet and was dried out using disking operations. Photographs taken during construction operations are shown in Figure 12. The test bed area was divided into three roller lanes as shown in Figure 13. Compaction was performed using the padfoot IC roller using 10 to 16 roller passes. All roller passes were performed in forward motion only. Lane 1 was compacted in static mode, lane 2 was compacted in low amplitude mode (a = 0.90 mm and f = 30 Hz), and lane 3 was compacted in high amplitude mode (a = 1.80 mm and f = 30 Hz). A summary of nominal machine settings is provided in Table 2.

In-situ point-MVs (γ_d, w, CBR_{250}, and $E_{LWD\text{-}Z2}$) were obtained at 9 locations along lanes 1 and 2, and 7 locations along lane 3. Point-MVs were obtained after 0, 1, 2, 4, 8, and 16 roller passes on lane 1, after 16 roller passes on lane 2, and after 10 roller passes on lane 3. The moisture content of the subgrade material varied between 9% and 16% which is about -3 to +4% of AASHTO T-180 w_{opt}. Comparison of w-γ_d point-MVs obtained on each lane after the final roller pass with laboratory Proctor test results is shown in Figure 14.

The objectives of testing on this test bed were to evaluate the influence of vibration amplitude on soil compaction properties (i.e., density, modulus, and CBR) and MDP* IC-MVs, and obtain correlations between MDP* IC-MVs and different point-MVs.

Figure 12. Photographs of construction and testing of TB1

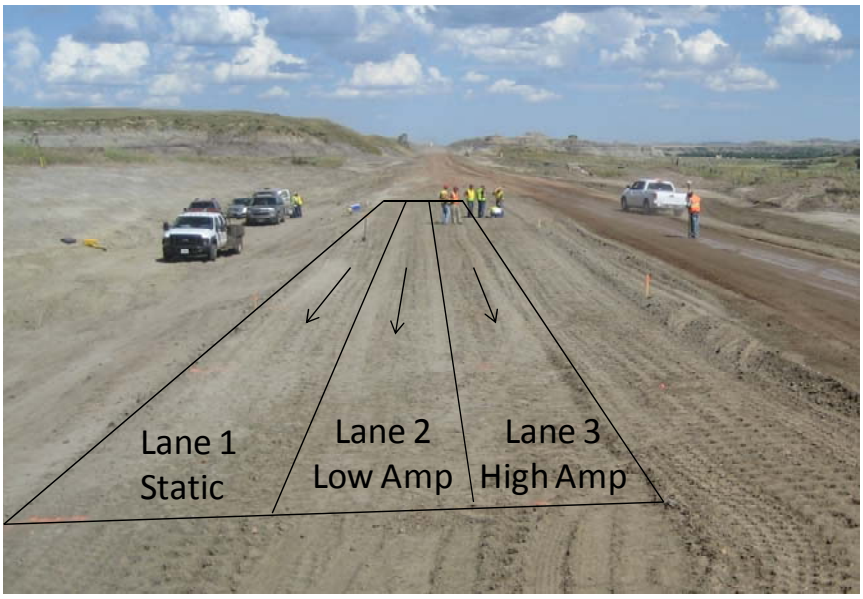

Figure 13. Subgrade calibration strips (lanes 1 to 3) – TB1

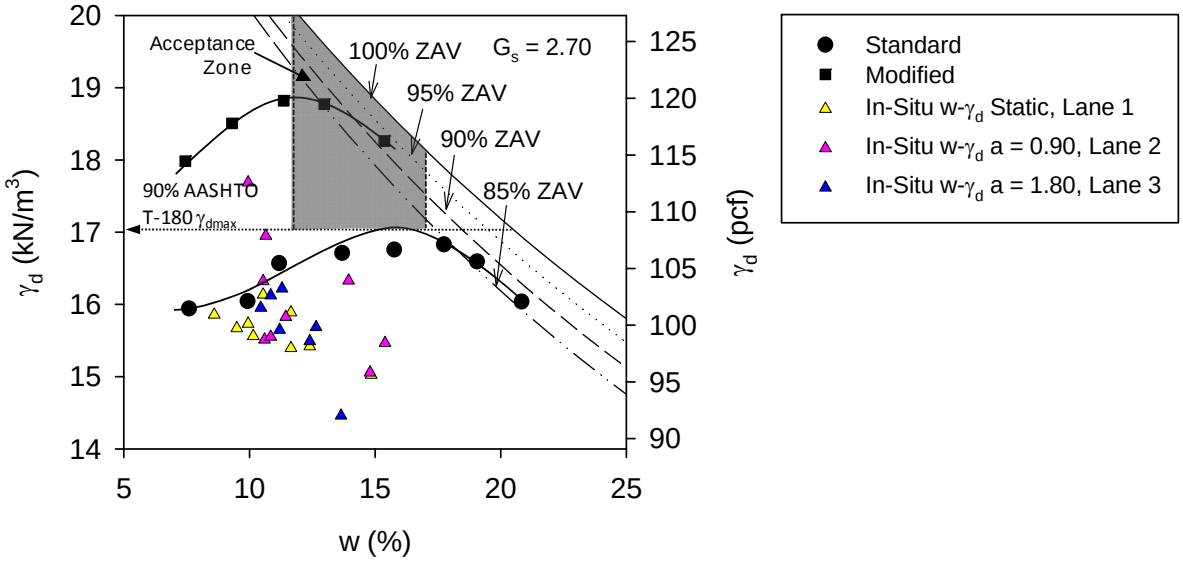

Figure 14. Comparison of in-situ moisture-dry unit weight measurements on TB1 (lanes 1 to 3 after final compaction pass) with laboratory Proctor test results

Test Results, Analysis, and Discussion

Spatial MDP* IC-MV and pass count maps for lanes 1, 2, and 3 are provided in Figure 15. MDP* spatial maps for multiple roller passes on each lane are also shown in Figure 15. MDP* line plots for lanes 1, 2, and 3 for multiple roller passes (1, 2, 4, 8, 10, 12, and 16) are provided in Figure 16. MDP* IC-MV plots for lanes 1 and 2 in Figure 16 indicate that the values are repeatable and they generally increase with increasing roller passes indicating compaction. The average MDP* on lanes 1 and 2 generally increased with increasing number of passes (Figure 17). On the other hand, MDP* on lane 3 where the high amplitude (a = 1.80 mm) setting was

used did not show a repeatable pattern along the lane (Figure 16) and the compaction growth curve yielded inconsistent results between passes (Figure 17). This is attributed to de-compaction of the material (as indicated by a reduction in average MDP* for passes 3, 5, and 9) at the surface and possibly deeper compaction due to the high amplitude setting used for compaction. On average, the MDP* values obtained on lane 2 in low amplitude mode were either similar or slightly lower (by about 1.02 to 1.05 times) than the MDP* values obtained on lane 1 in static mode. The average MDP* values obtained on lane 3 in high amplitude mode were lower (by about 1.19 to 1.25 times) than the average MDP* values on lanes 1 and 2.

Average point-MV compaction curves for lane 1 are presented in Figure 17. On average, γ_d, $E_{LWD\text{-}Z2}$, and CBR_{250} increased with increasing pass indicating compaction. The average $E_{LWD\text{-}Z2}$ continued to increase with increasing compaction passes up to 16 passes. The average γ_d increased up to 2 passes, remained constant up to 8 passes, and then continued to increase up to 16 passes. The average CBR_{250} increased up to 2 passes, remained about the same up to 4 passes, and then continued to increase up to 16 passes. The average point-MVs obtained after the final compaction pass on lanes 2 and 3 are also presented for comparison in Figure 17. On average, the $E_{LWD\text{-}Z2}$ and CBR_{250} point-MVs were lower on lanes 2 and 3 compacted in low and high amplitude mode, compared to lane 1 compacted in static mode. In contrary, the average γ_d on lanes 2 and 3 was greater on lanes 2 and 3 than on lane 1.

MDP* IC-MV plots (as lines) in comparison with point-MVs (as points) along lane 1 after 1, 2, 4, 8, and 16 passes are presented in Figure 18 to Figure 20. DCP-CBR depth profiles obtained before compaction (pass 0), and after 1, 2, 4, 8, and 16 passes on lane 1 at each point location are presented in Figure 21. MDP* IC-MV plots in comparison with point-MVs along lane 2 after 16 passes are presented in Figure 22. DCP-CBR depth profiles obtained after 16 passes on lane 2 at each point location are presented in Figure 23. MDP* IC-MV plots in comparison with point-MVs along lane 3 after 10 passes are presented in Figure 24. DCP-CBR depth profiles obtained after 16 passes on lane 3 at each point location are presented in Figure 25.

Regression analysis results between IC-MVs and point-MVs by spatially pairing the nearest point data is presented separately for lanes 1, 2, and 3, in Figure 26, Figure 27, and Figure 28, respectively. Regression relationships for lane 1 where MDP* values were obtained in static mode showed R^2 values ranging from 0.15 to 0.54. MDP* values were better correlated with $E_{LWD\text{-}Z2}$ ($R^2 = 0.54$), than with CBR_{250} ($R^2 = 0.17$) and γ_d ($R^2 = 0.15$). This observation is generally consistent with findings from several previous case studies that the IC-MVs correlate better with stiffness or modulus measurements compared to density measurements. The MDP* values on lane 1 did not show a statistically significant relationship with *w*. Correlations on lanes 2 and 3 generally showed weak relationships and sometimes incorrect trends (for e.g., MDP* versus CBR_{250} on lane 2 and MDP* versus γ_d on lane 3 showed decreasing MDP* with increasing point-MV). The narrow range of measurements on lanes 2 and 3 (MDP* varied from 116 to 121 on lane 2 and 101 to 108 on lane 3) as the measurements were obtained only after the final compaction pass, contributed to such weak relationships. On lane 3, de-compaction of the subgrade material was observed at the surface which also can affect the relationships. MDP* values on lanes 2 and 3 showed statistically significant relationship with *w* with $R^2 = 0.67$ and 0.86, respectively.

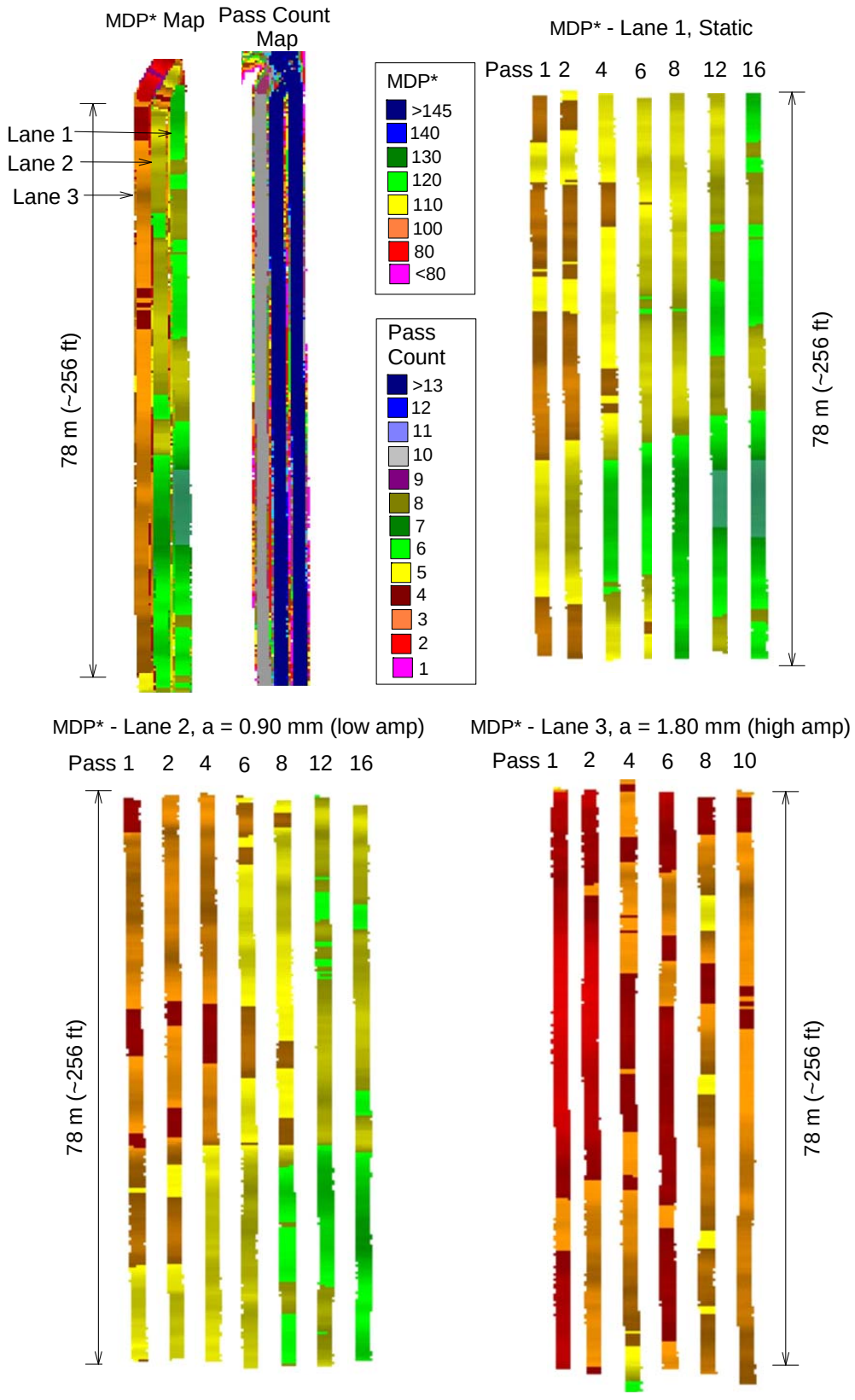

Figure 15. MDP* and elevation maps of lanes 1 to 3, and MDP* spatial maps for multiple padfoot roller passes on lanes 1 to 3 – TB1

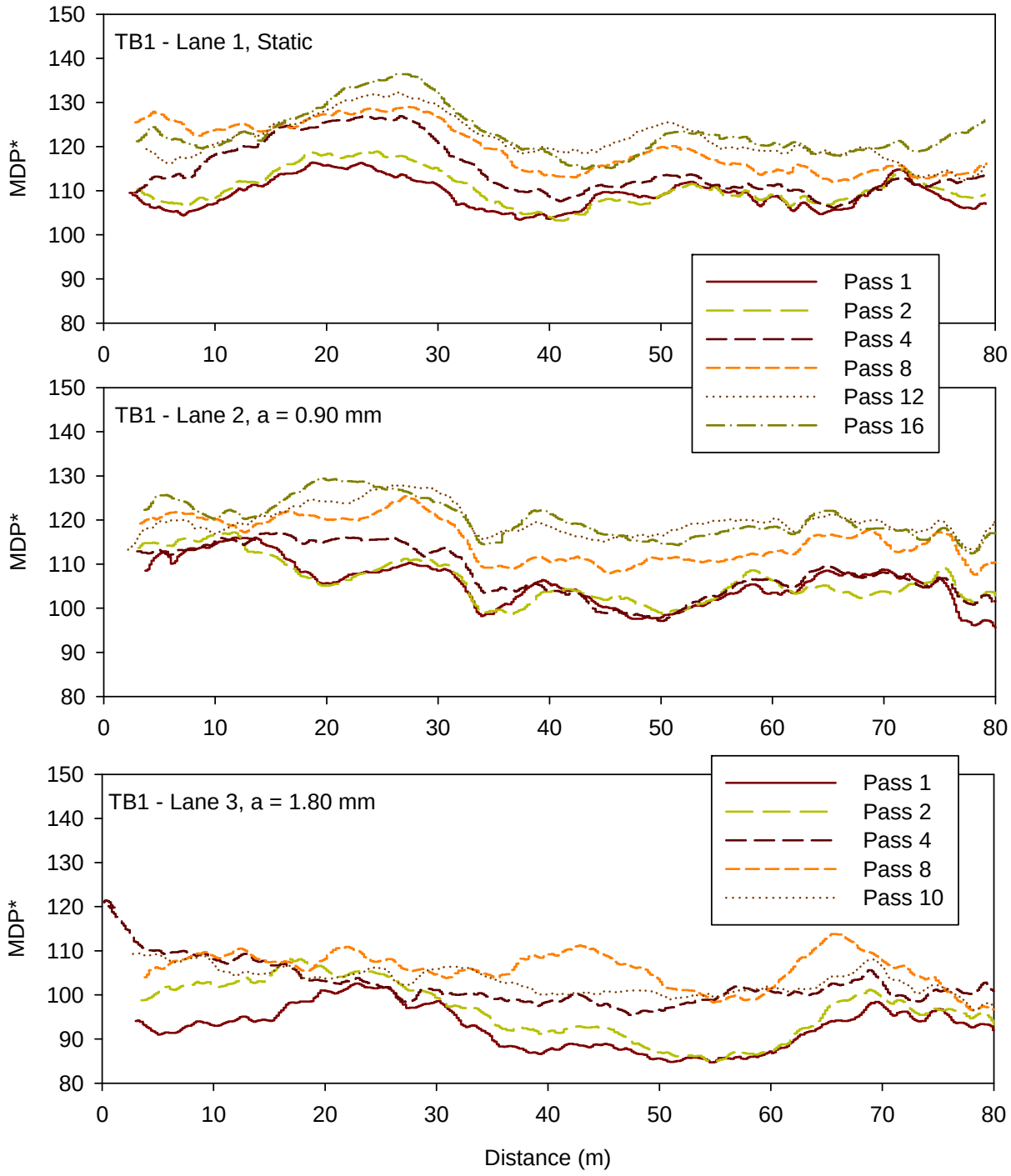

Figure 16. MDP* data for multiple roller passes on lanes 1 to 3 – TB1

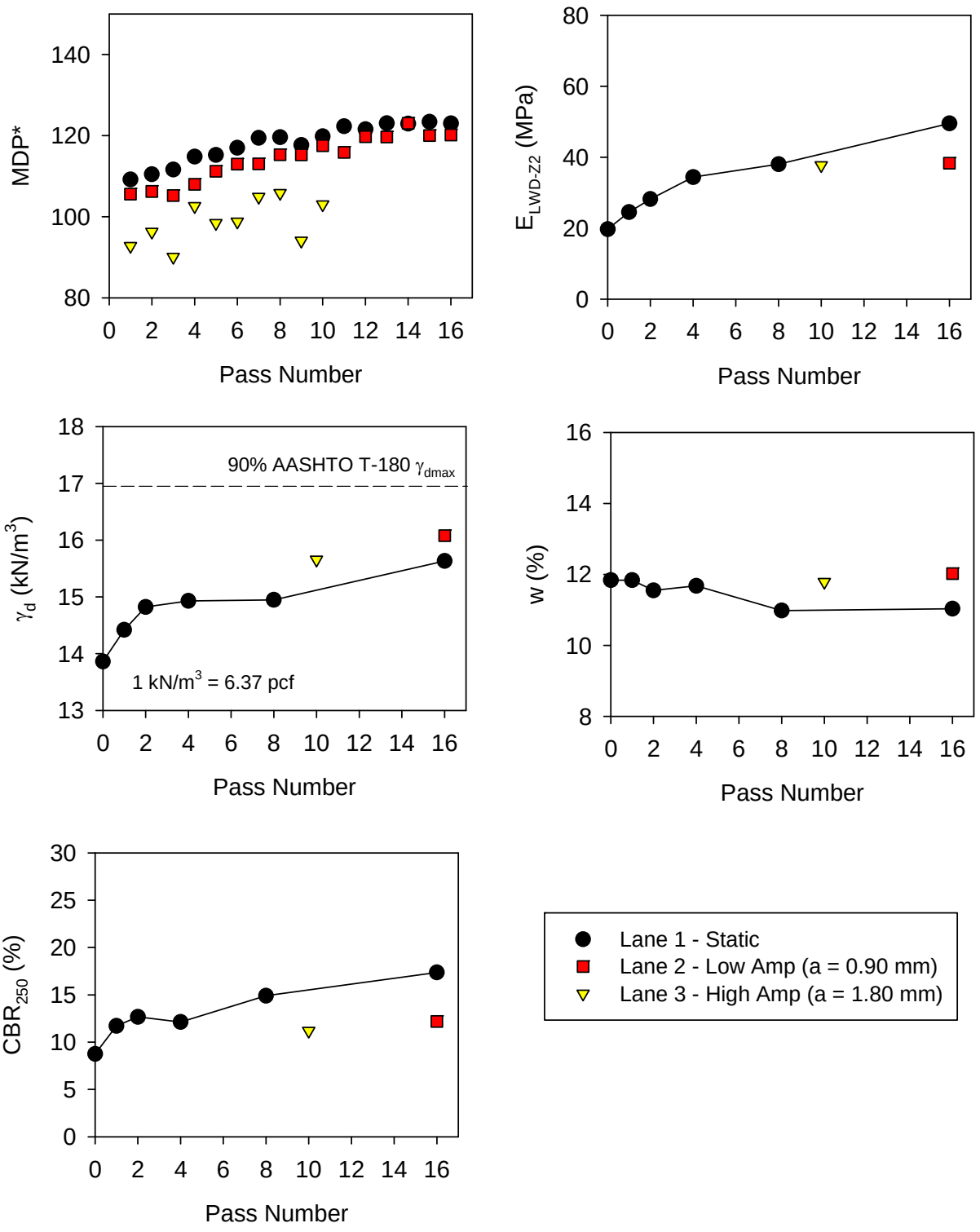

Figure 17. Average MDP* and in-situ point measurement values with increasing roller passes on lanes 1 to 3 – TB1

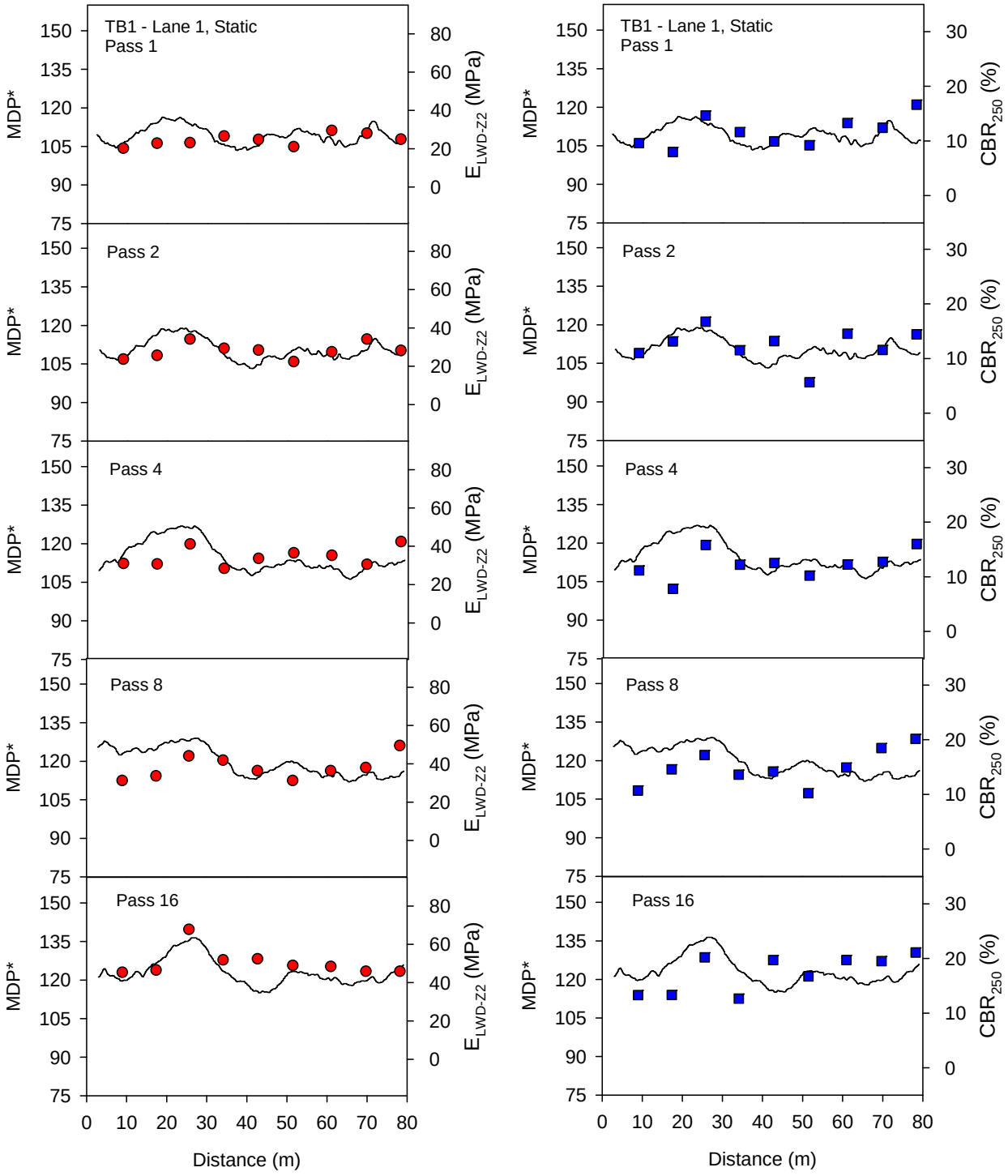

Figure 18. Comparison between MDP* and in-situ LWD and CBR point measurements on lane 1 for multiple roller passes – TB1

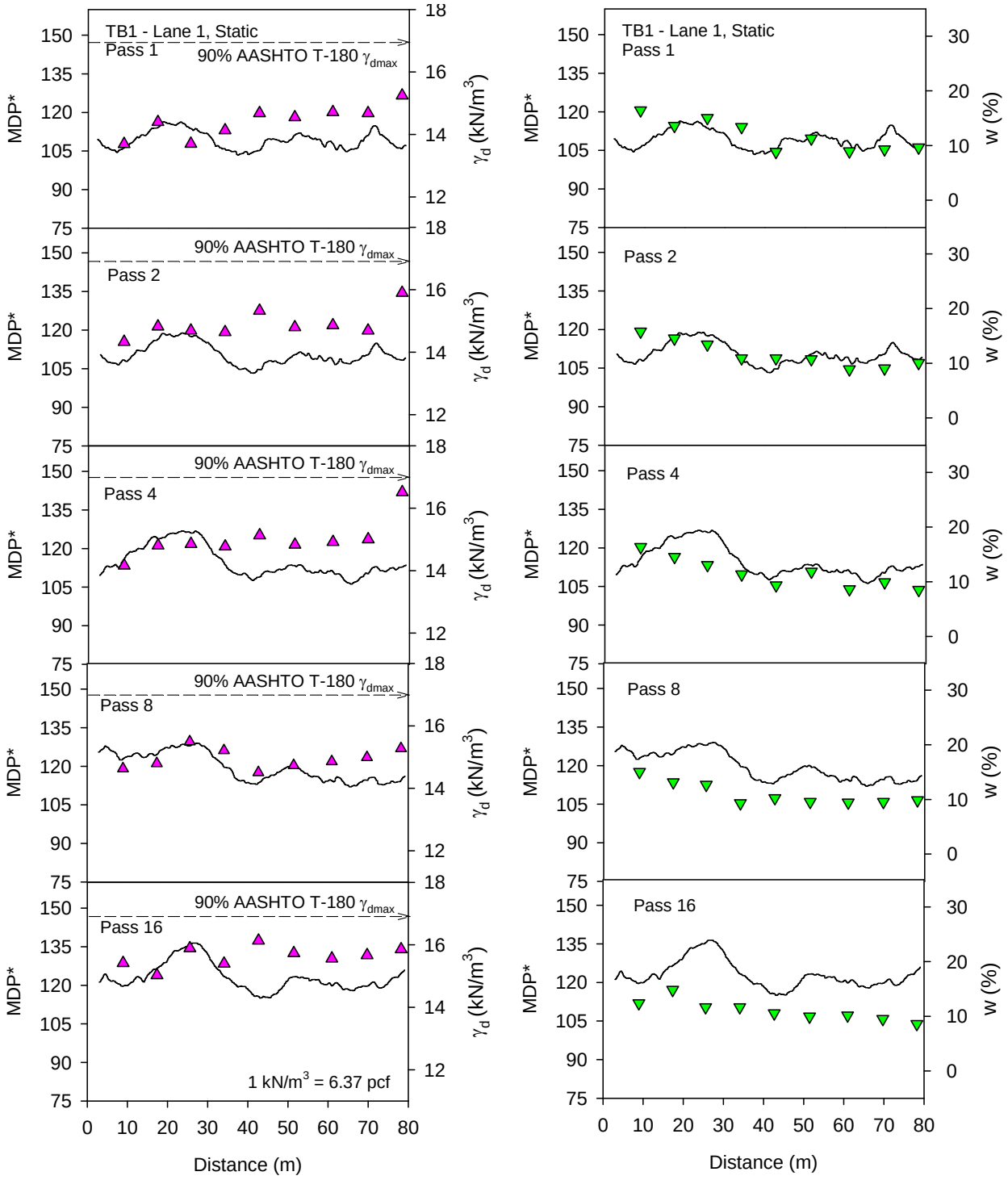

Figure 19. Comparison between MDP* and in-situ NG point measurements (dry unit weight and moisture content) on lane 1 for multiple roller passes – TB1

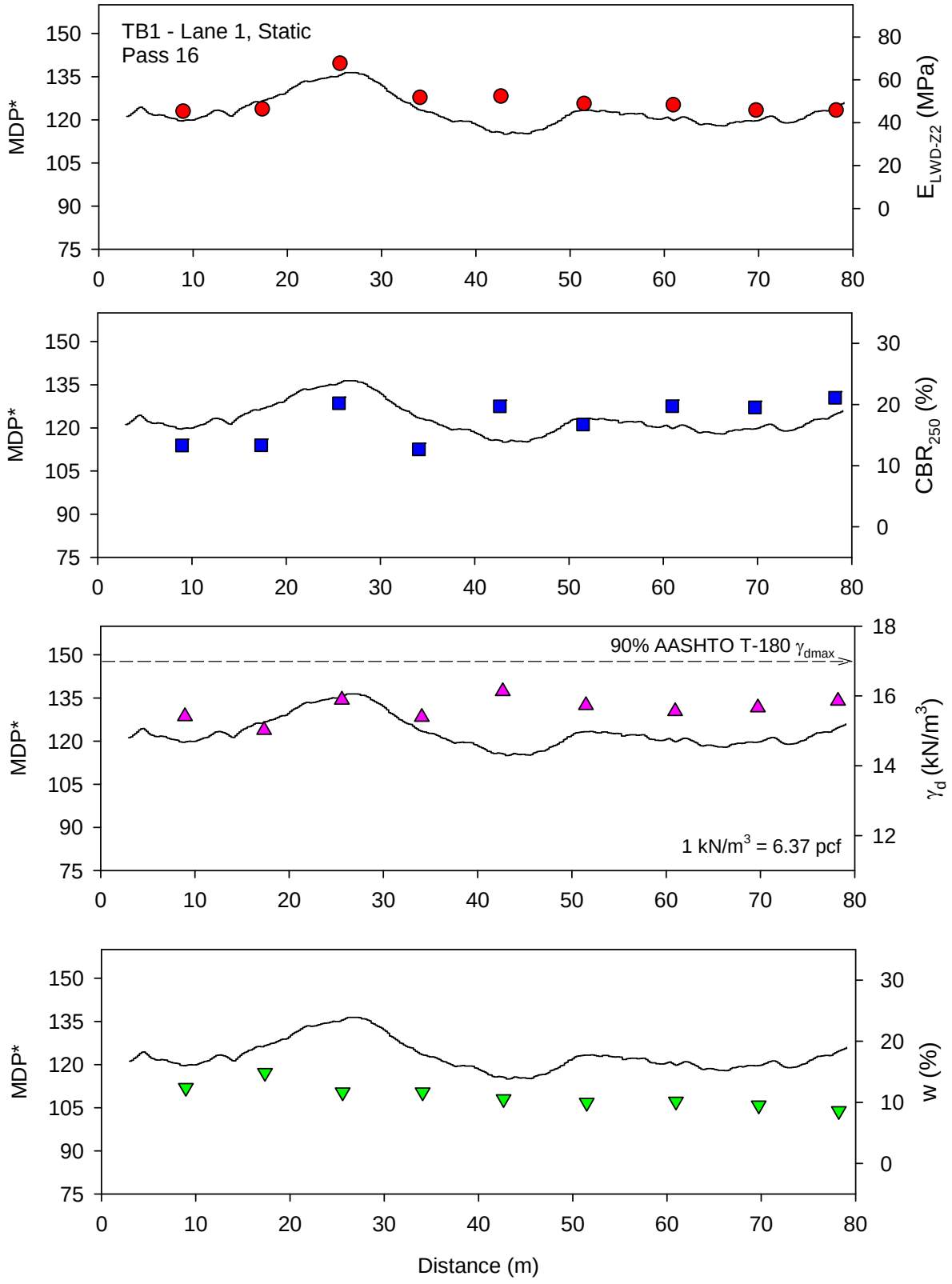

Figure 20. Comparison between MDP* and in-situ point measurements on lane 1 (static) after pass 16 – TB1

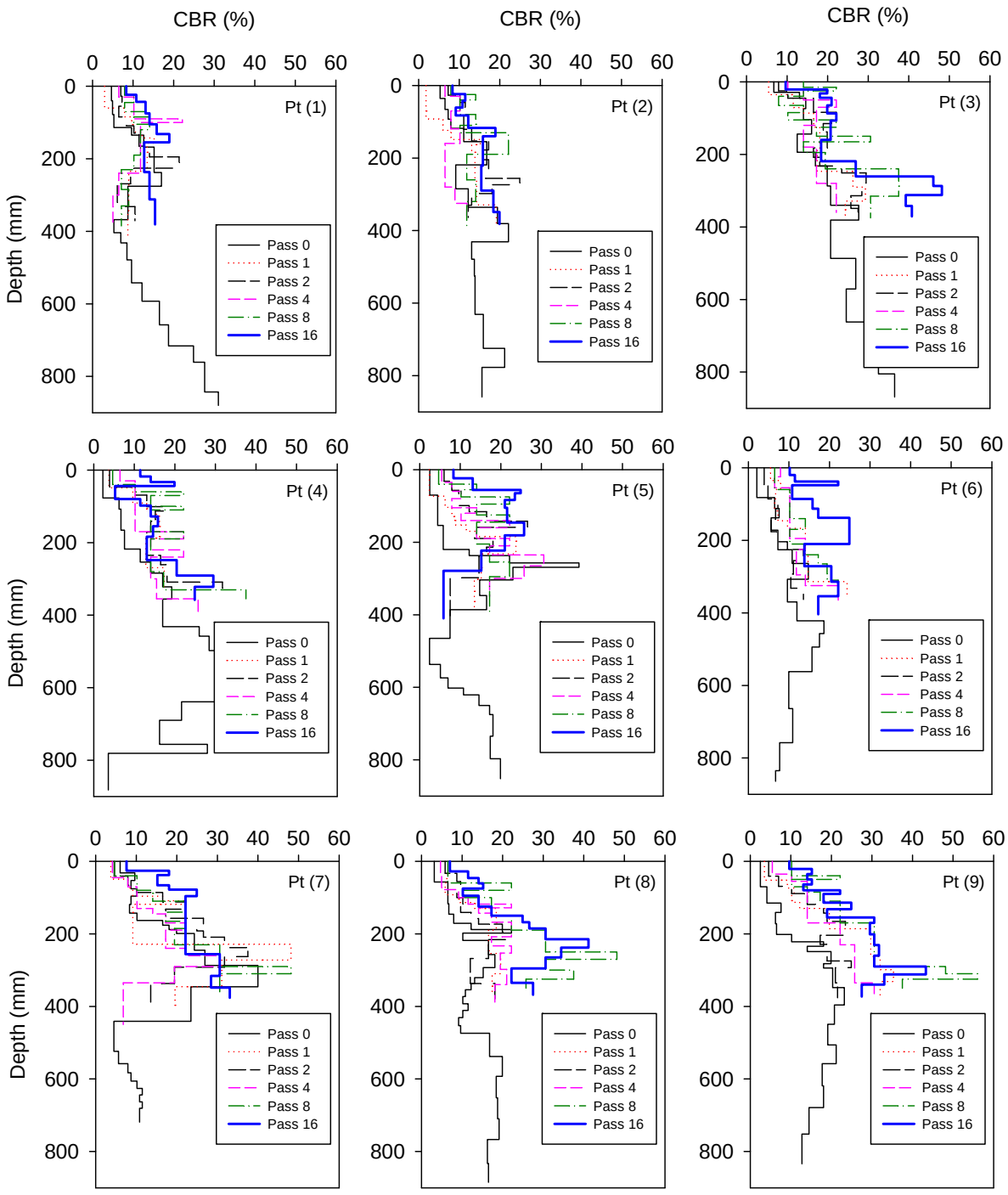

Figure 21. DCP-CBR profiles on lane 1 before compaction (pass 0) and after passes 1, 2, 4, 8, and 16 – TB1

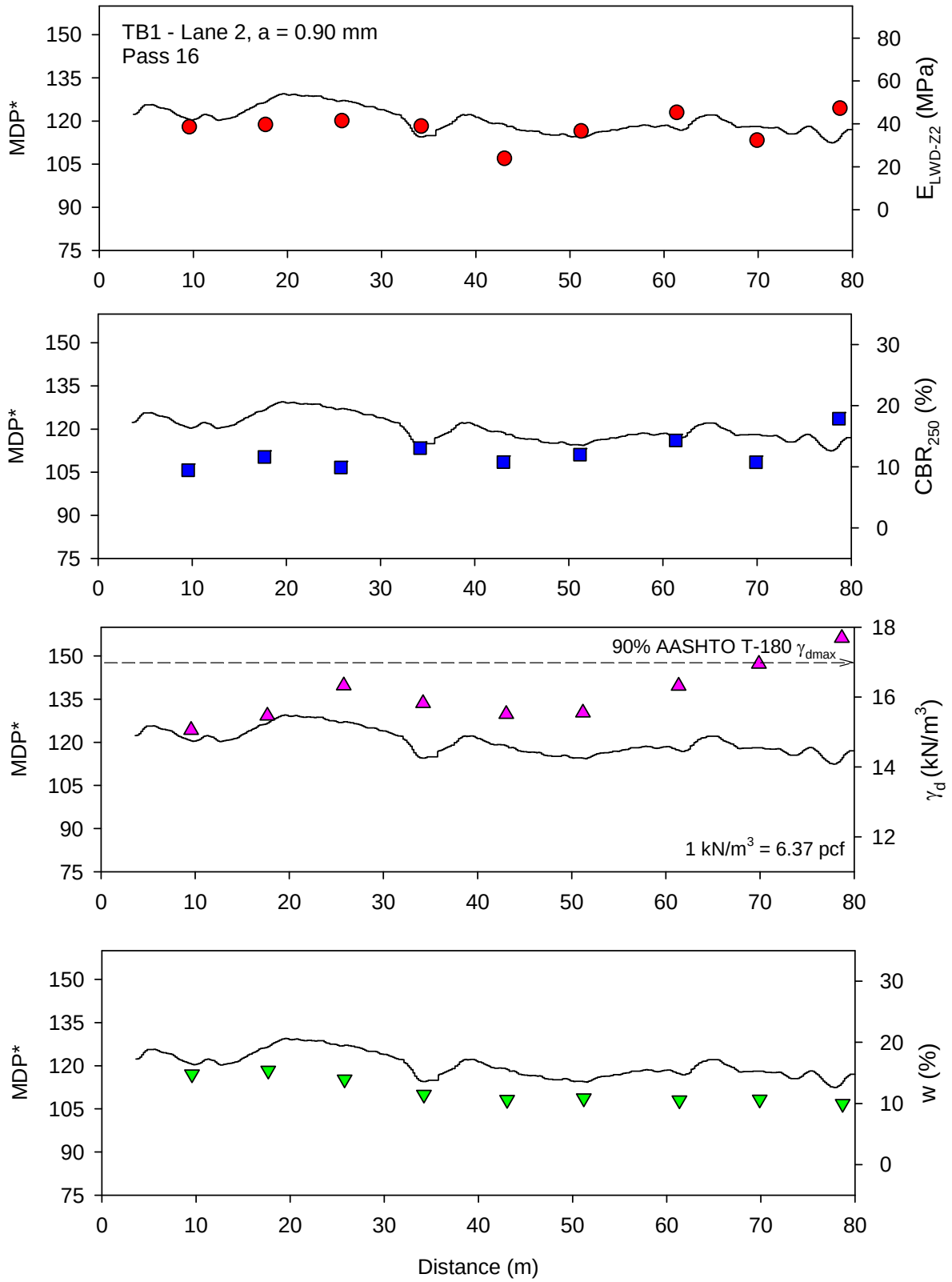

Figure 22. Comparison between MDP* and in-situ point measurements on lane 2 (low amplitude mode) after pass 16 – TB1

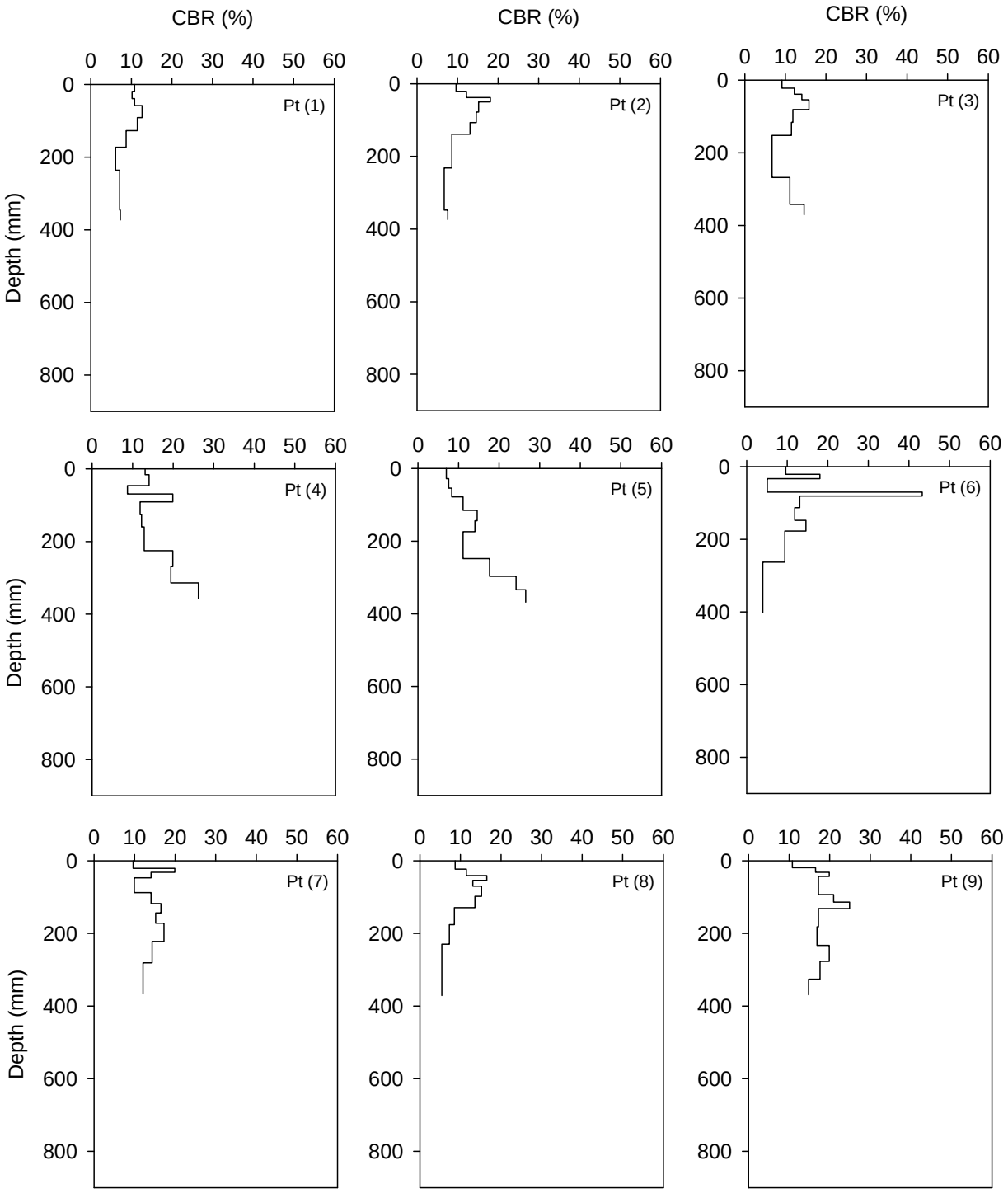

Figure 23. DCP-CBR profiles on lane 2 after 16 passes – TB1

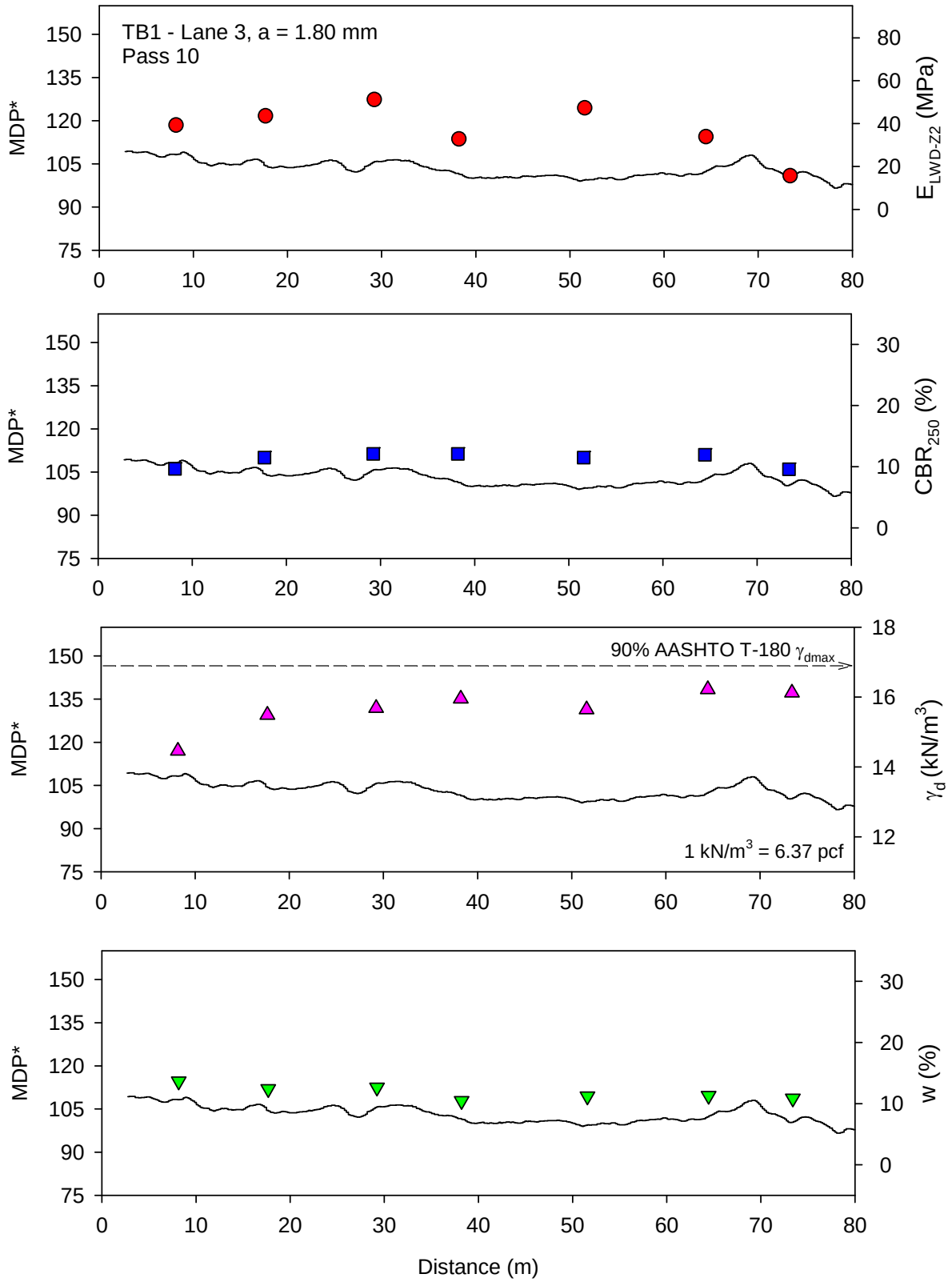

Figure 24. Comparison between MDP* and in-situ point measurements on lane 3 (high amplitude mode) after pass 10 – TB1

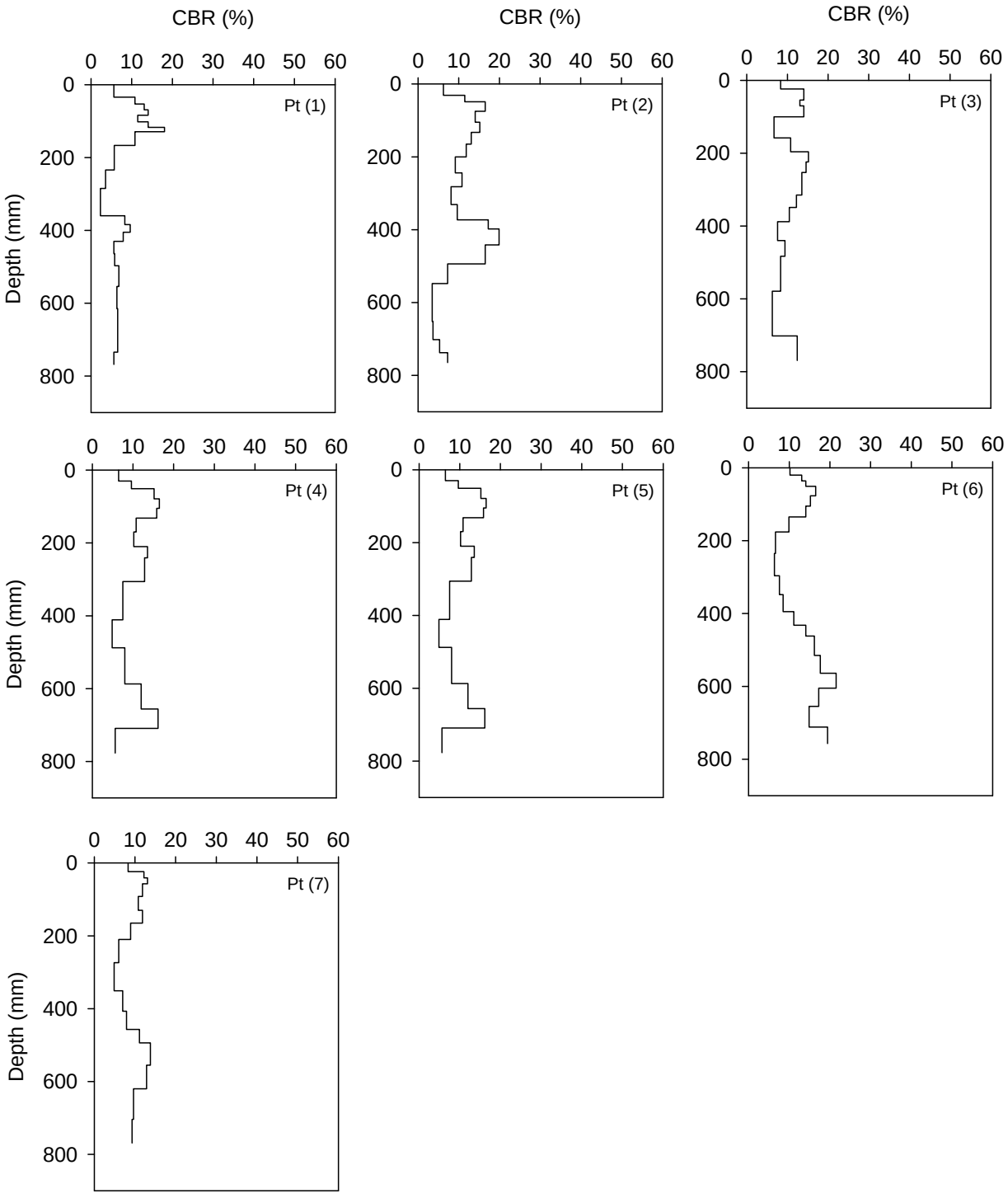

Figure 25. DCP-CBR profiles on lane 3 after 10 passes – TB1

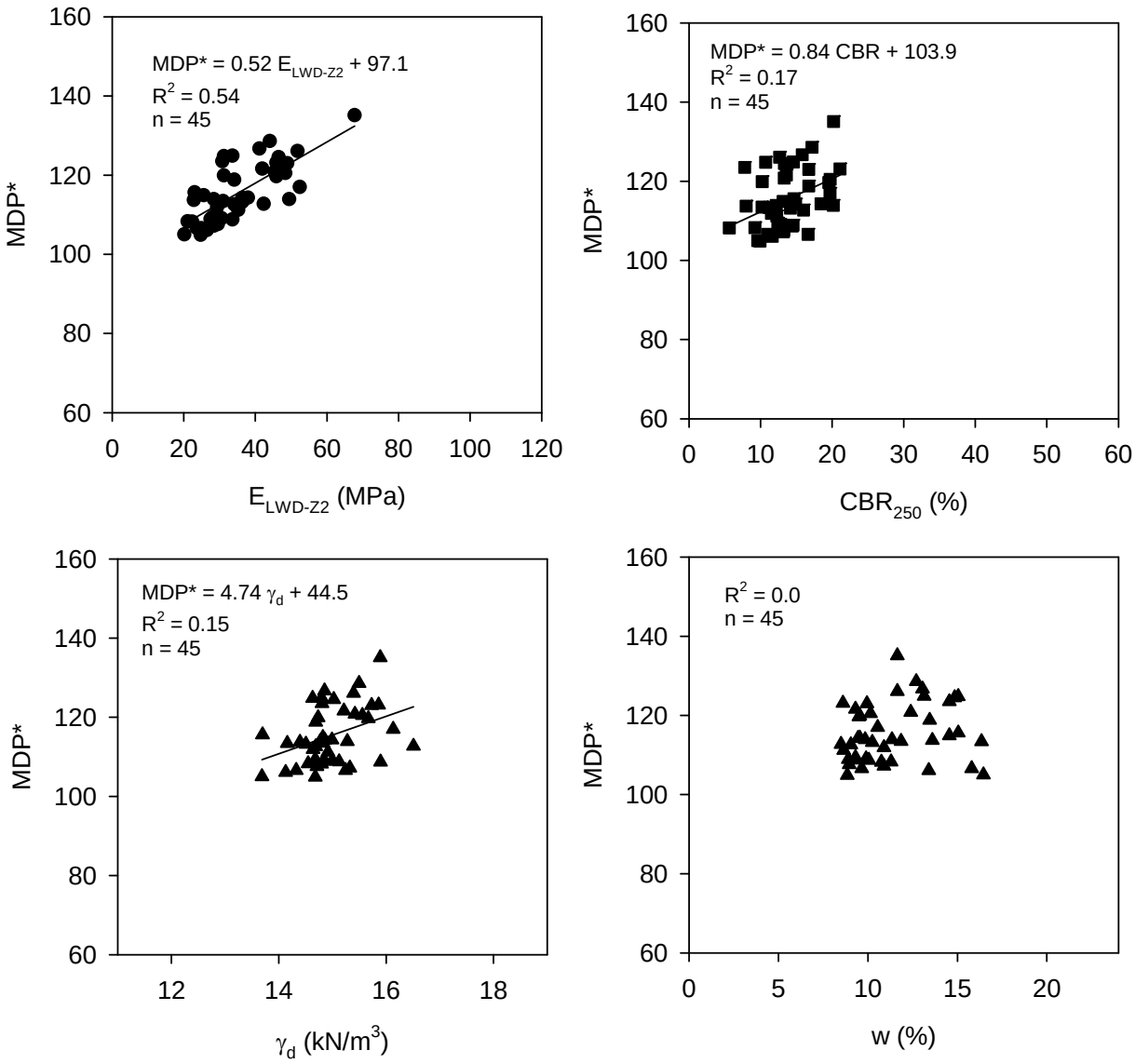

Figure 26. Correlations between MDP* and in-situ point measurements on lane 1 (static) – TB1

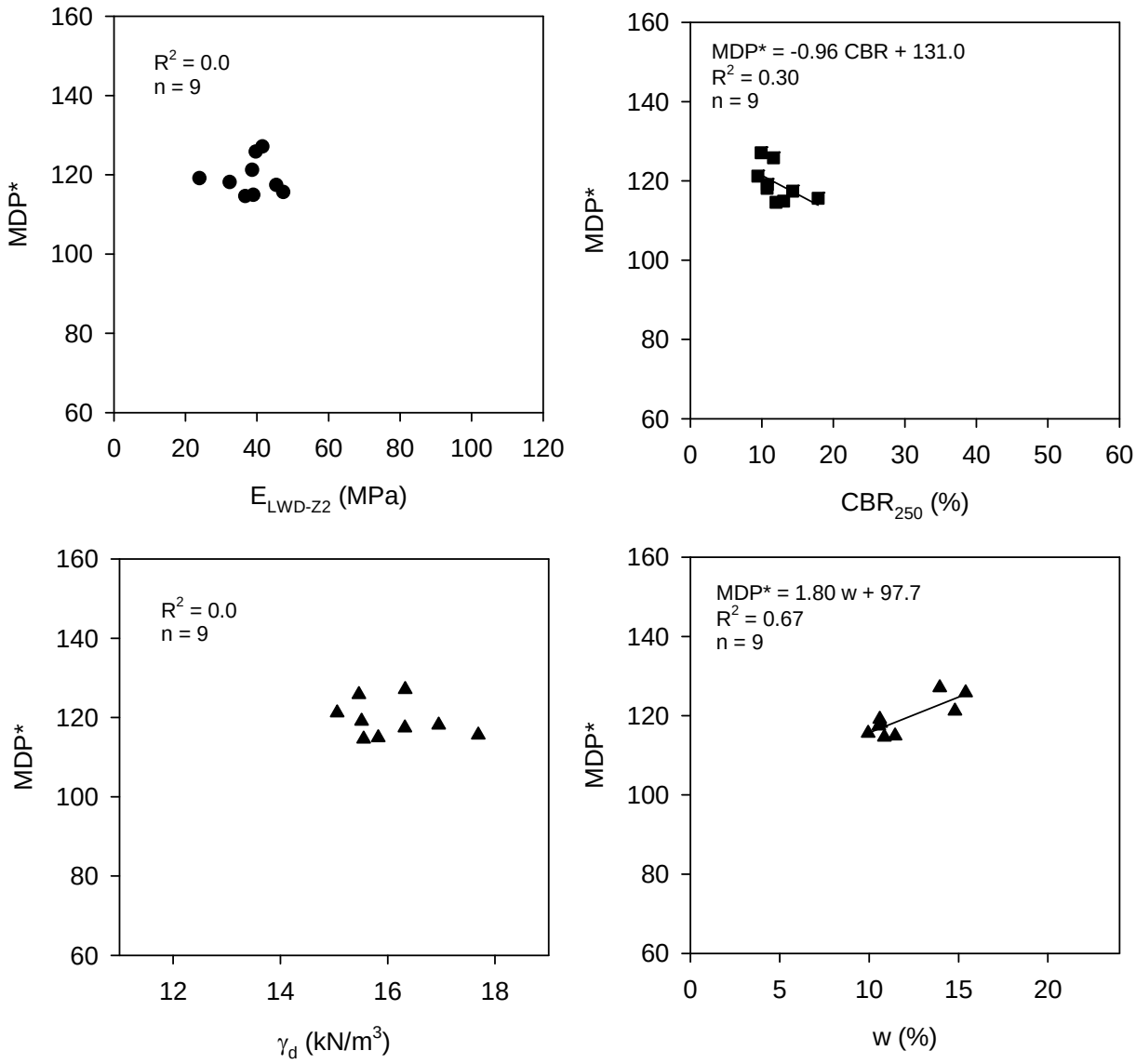

Figure 27. Correlations between MDP* and in-situ point measurements on lane 2 (*a* = 0.90 mm and *f* = 30Hz) – TB1

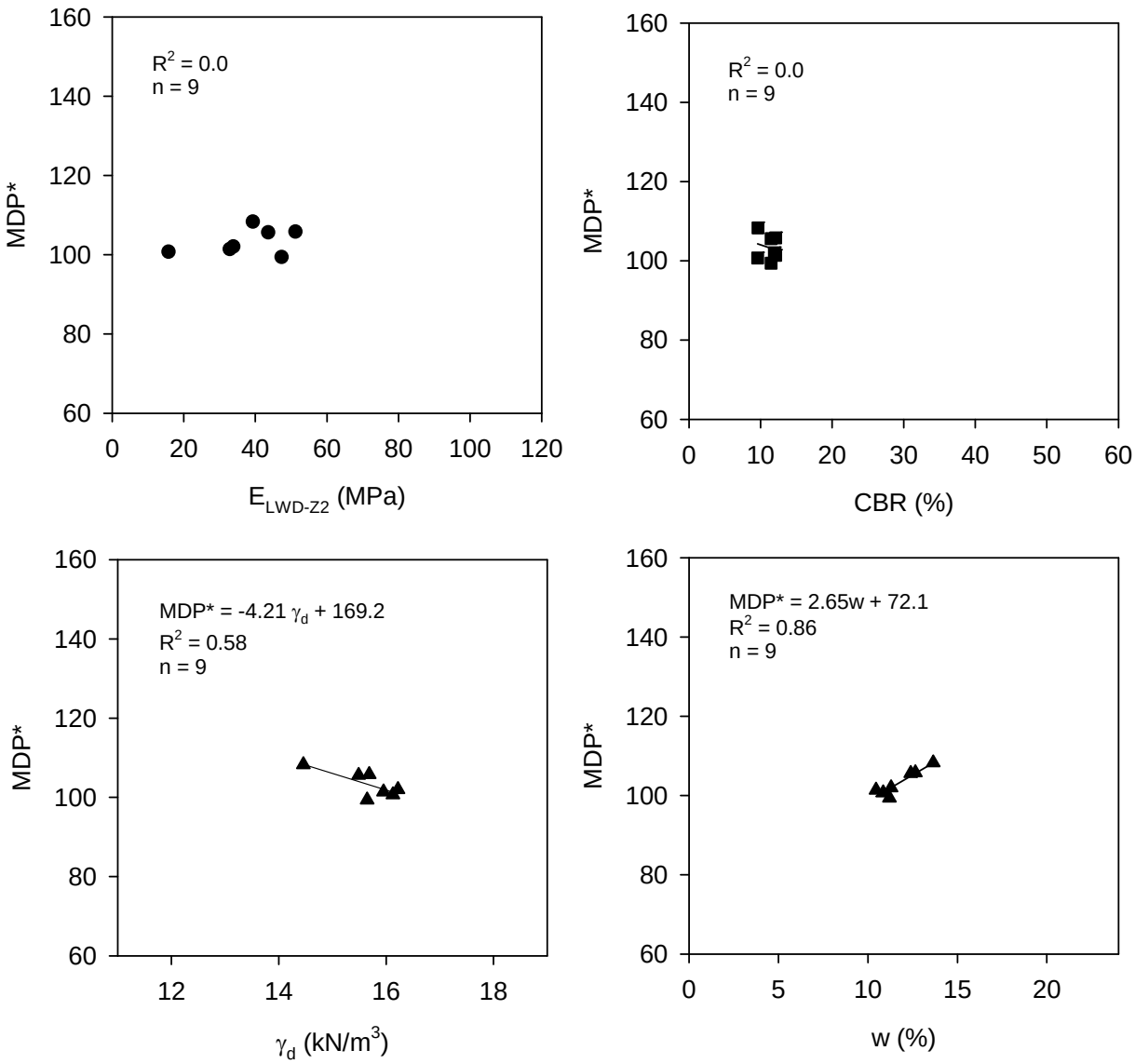

Figure 28. Correlations between MDP* and in-situ point measurements on lane 3 (*a* = 1.80 mm and *f* = 30 Hz) – TB1

TB2 Compacted Subgrade (Padfoot Roller)

TB2 consisted of a 30 m long test strip with compacted silty subgrade material and was located next to TB1. The test bed visually showed rutting or sinkage under construction traffic loading in two isolated locations (Figure 29). The test bed area was mapped using one roller pass in low amplitude setting (a = 0.90 mm and f = 30 Hz) using the padfoot IC roller. Following the roller pass, $E_{LWD\text{-}Z2}$ point-MVs were obtained at six locations across the test bed. MDP* IC-MVs in comparison with $E_{LWD\text{-}Z2}$ point-MVs are presented in Figure 30. Both MDP* and $E_{LWD\text{-}Z2}$ measurements showed relatively low values in the rutting areas. Correlation between MDP* and $E_{LWD\text{-}Z2}$ by spatially pairing the nearest point data is presented in Figure 31, which yielded R^2 = 0.40.

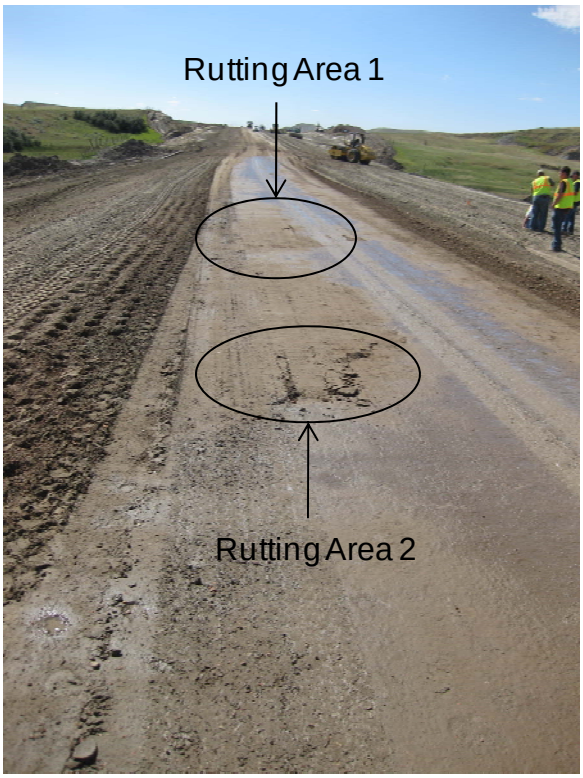

Figure 29. Picture of TB2 showing visually identified soft areas

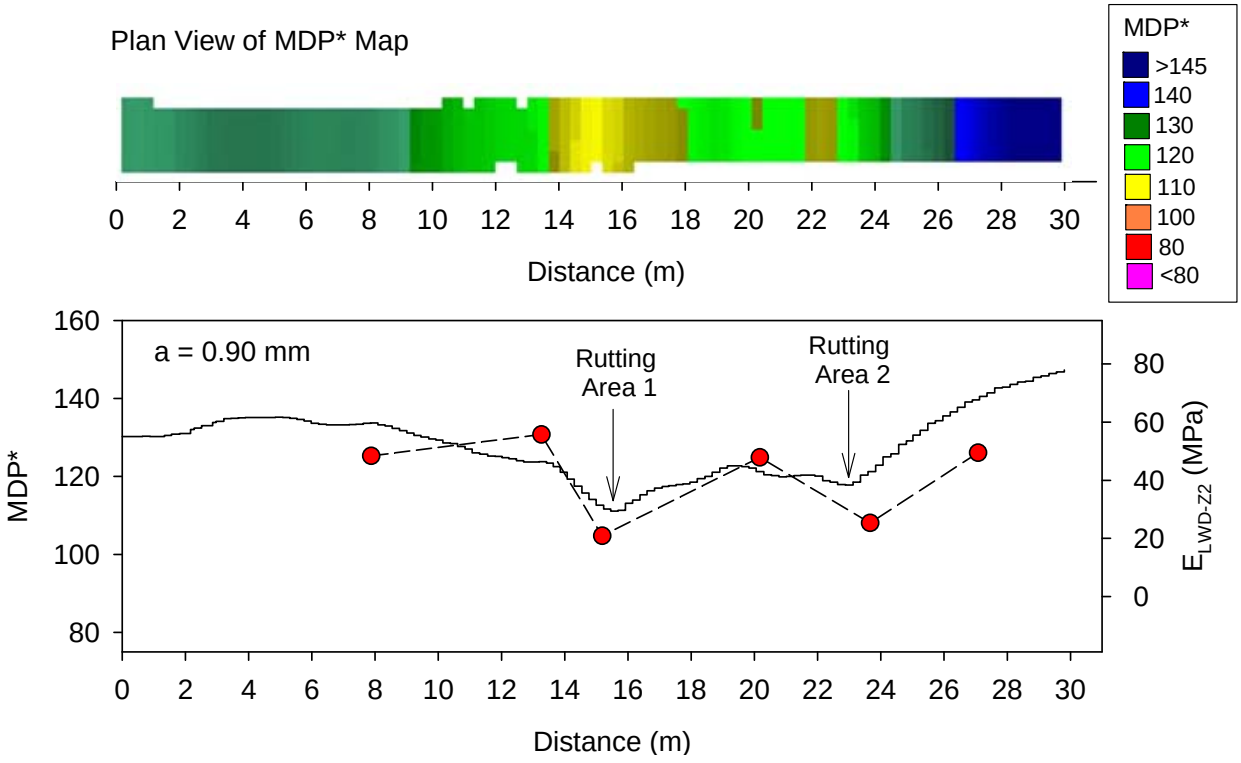

Figure 30. MDP* and E_{LWD-Z2} measurements on TB2

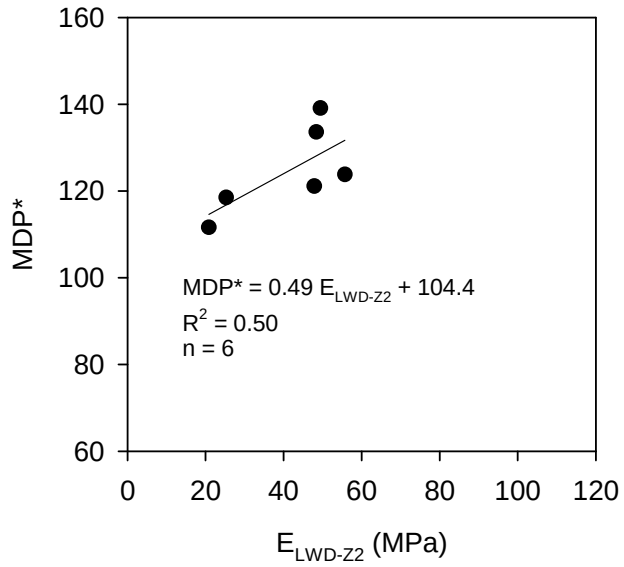

Figure 31. Correlation between MDP* (*a* = 0.90 mm and *f* = 30Hz) and E_{LWD-Z2} – TB2

TBs 3 and 7 Subgrade Production Compaction (Padfoot Roller)

Test bed construction and in-situ testing – TB 3

This test bed consisted of a production area with silty subgrade material (Figure 32) scarified to a depth of about 250 mm and was constructed following similar methods as discussed in TB1. Plan dimensions of the test bed were about 6.5 m x 302 m. The area was compacted with 9 roller passes using the padfoot IC roller in static mode followed by one mapping pass each in static and low amplitude (a = 0.90 mm and f = 30 Hz) modes. Nominal machine settings during each pass are summarized in Table 2. After the final mapping pass, the test bed area was leveled and sealed using a pneumatic roller for two roller passes. Based on the final mapping pass MDP* IC-MV map, point-MVs ($E_{LWD\text{-}Z2}$ and DCP-CBR profiles) were obtained from 10 test locations.

Figure 32. Photograph of the test bed area – TB3

In-situ test results, analysis, and discussion – TB3

Figure 33 shows MDP* maps in static and low amplitude modes, elevation map, and pass coverage map for the test bed area. Monitoring the elevation maps during construction can be a useful QC method to control lift thickness. Similarly, pass count coverage maps can also be used for QC. Figure 33 shows compaction curves of MDP* at three selected locations with relatively high, medium, and low MDP* values. Analyzing compaction curves also can also serve as an effective QC technique to assess the compaction state of the material.

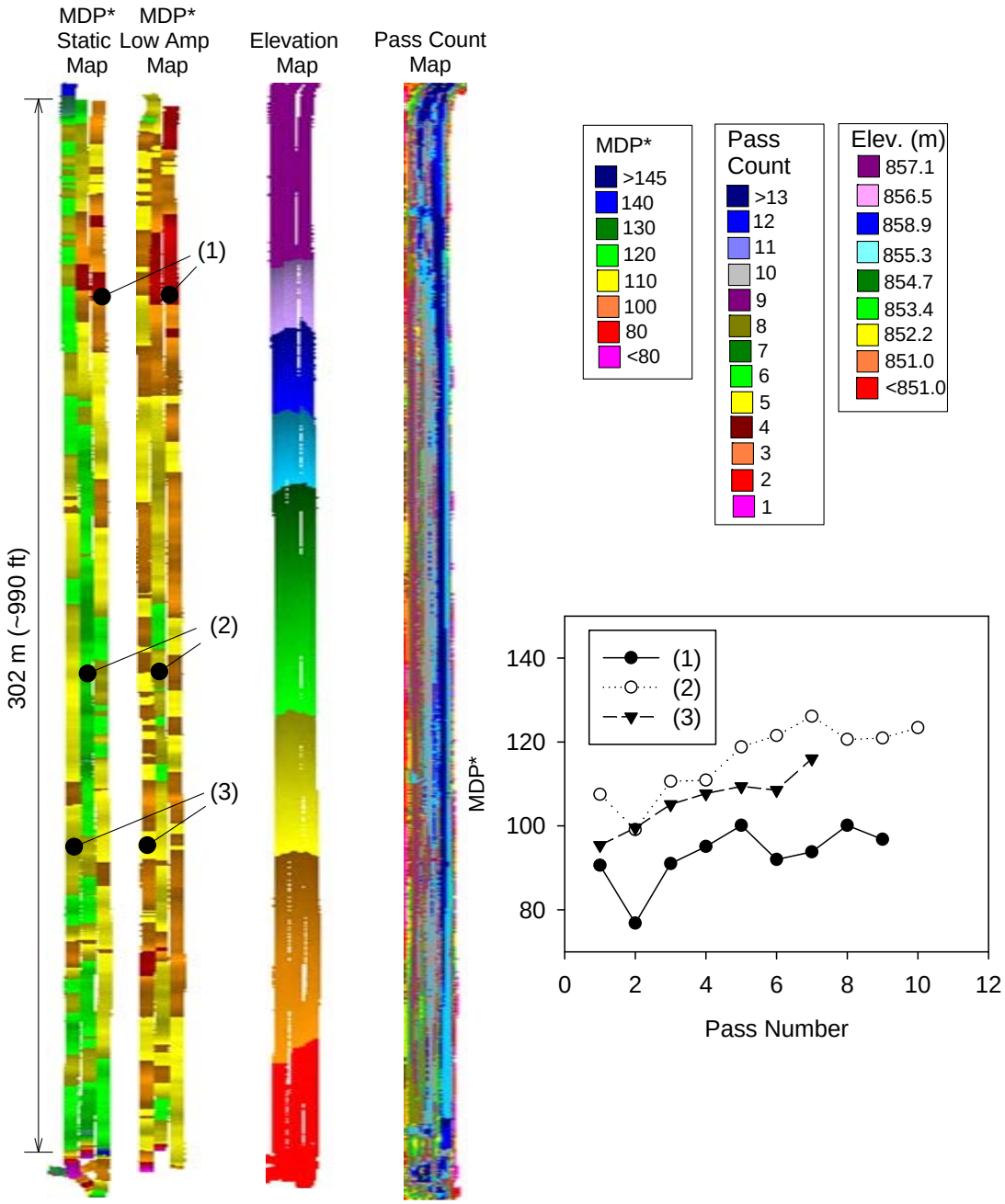

Figure 33. MDP*, percent target MDP*, elevation, and pass count maps, and MDP* compaction curves at three selected locations – TB3

Figure 34 shows MDP* and percent target MDP* (assuming a target MDP* = 140) histogram plots. On average, the MDP* values obtained in static mode were greater by about 1.06 times than the MDP* values obtained in low amplitude mode. Plotting the percent target MDP* data can be used for pass/fail analysis which can be useful for QA purposes. Geostatistical semivariograms of MDP* values for static and low amplitude passes are presented in Figure 35 along with a summary of the spatial statistics (i.e., nugget, sill, and range). The experimental semivariograms values showed a nested spatial structure with short-range and long-range components. Nested spherical variograms were fit to the experimental semivariogram data. It is

possible that the long-range spatial structure is linked to the spatial variation in underlying layer support conditions while the short-range spatial structure is a result of soil properties close to the surface. Similar nested variograms were observed in a previous field study conducted in New York as part of the FHWA IC pooled fund study (see New York field study report, White et al. 2010). The static MDP* values show more variability with high sill values compared to low amplitude MDP* values. This is also evident with a slightly higher standard deviation (σ) value for static MDP* over low amplitude MDP* as shown in Figure 34. More interestingly, the geostatistical variograms show similar long-range components for both static and low amplitude MDP* values (i.e., similar $Range_2$ values (i.e., about 56 m) and similar difference between $Sill_2$-$Sill_1$ (i.e., about 8 to 10)). These concepts have not previously been evaluated and could provide an important step in understanding the spatial variability associated with IC data.

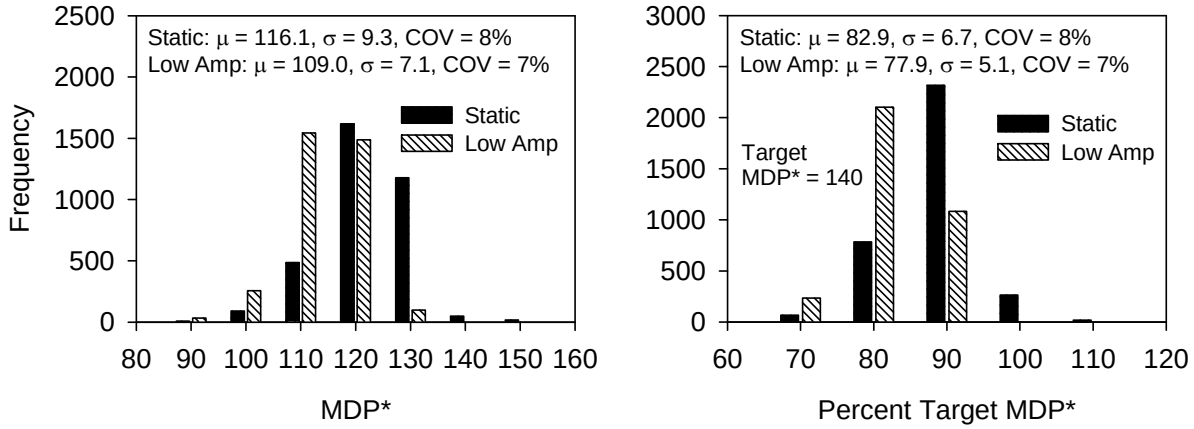

Figure 34. Histograms of MDP* and percent target MDP* for the static and low amplitude mapping passes – TB3

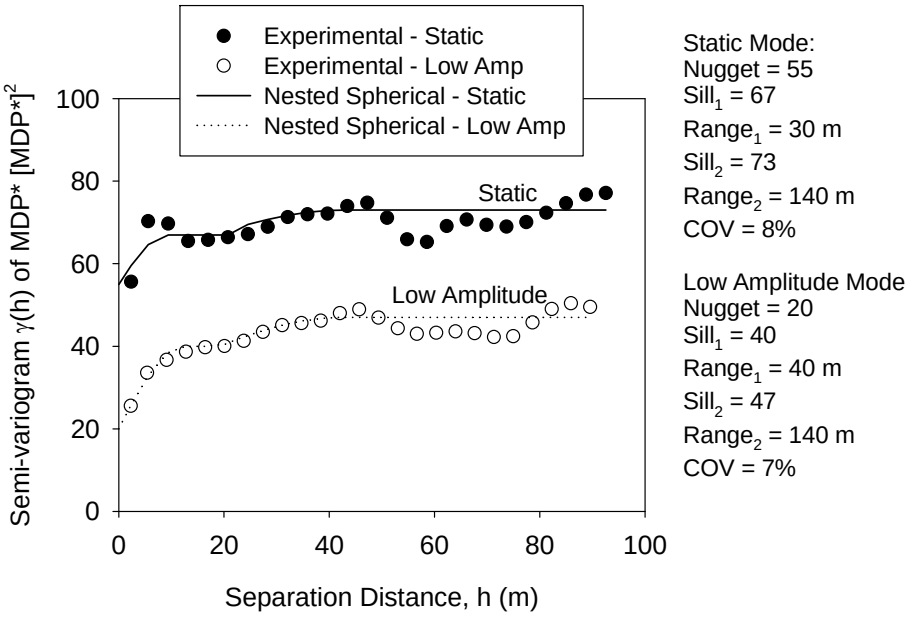

Figure 35. Geostatistical semivariograms of MDP* from static and low amplitude mapping passes – TB3

Figure 36 presents DCP-CBR profiles along with $E_{LWD\text{-}Z2}$ point-MVs obtained at 12 selected locations across the test bed area. Figure 37 shows correlations between MDP* and $E_{LWD\text{-}Z2}$ and CBR_{250} point-MVs by spatially pairing the nearest point data. Non-linear power relationships showed the best fit for these relationships. Point-MV relationships with static MDP* values yielded higher R^2 values (0.74 to 0.75) than with low amplitude MDP* values (0.37 to 0.52).

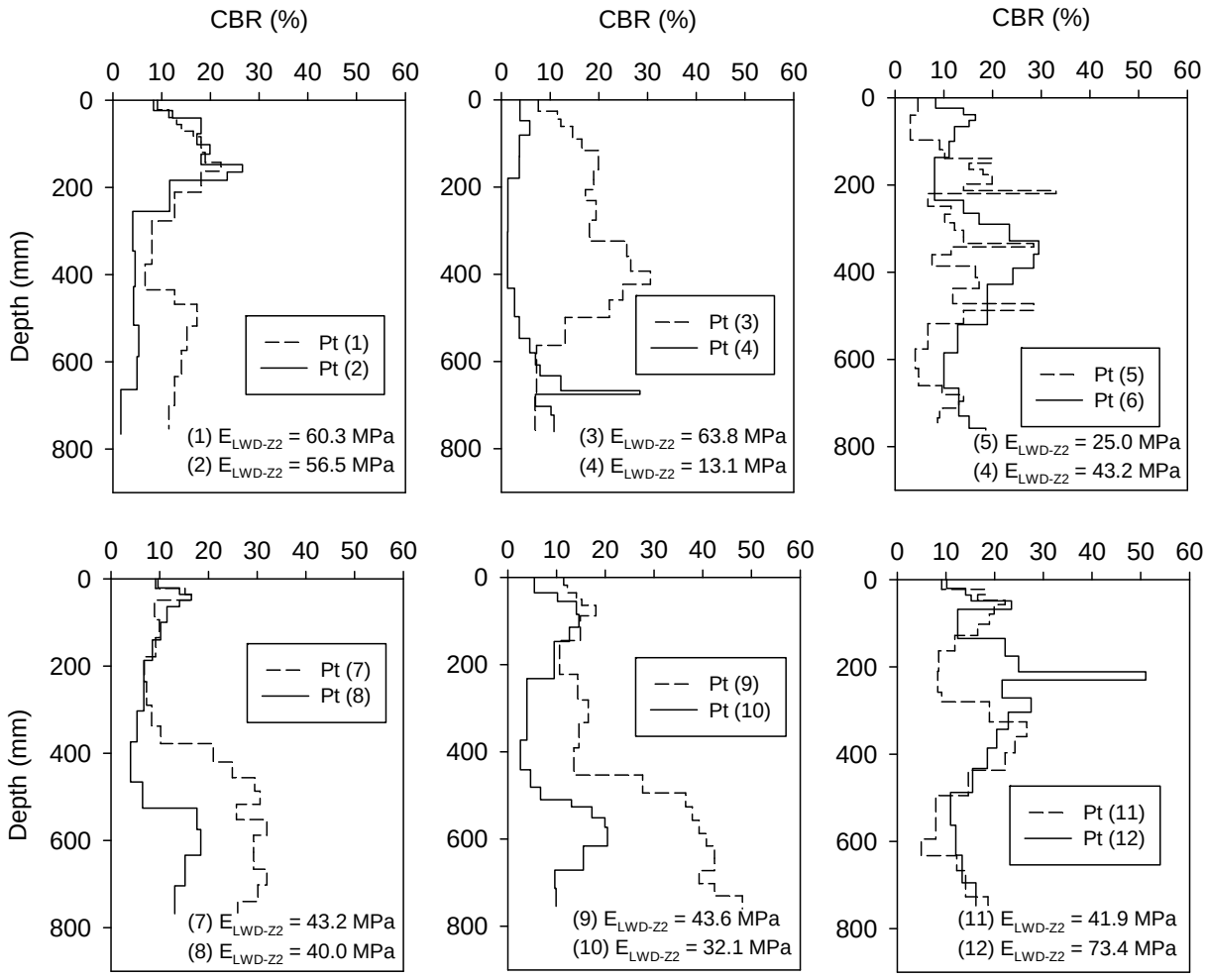

Figure 36. DCP-CBR profiles at selected in-situ test locations – TB3

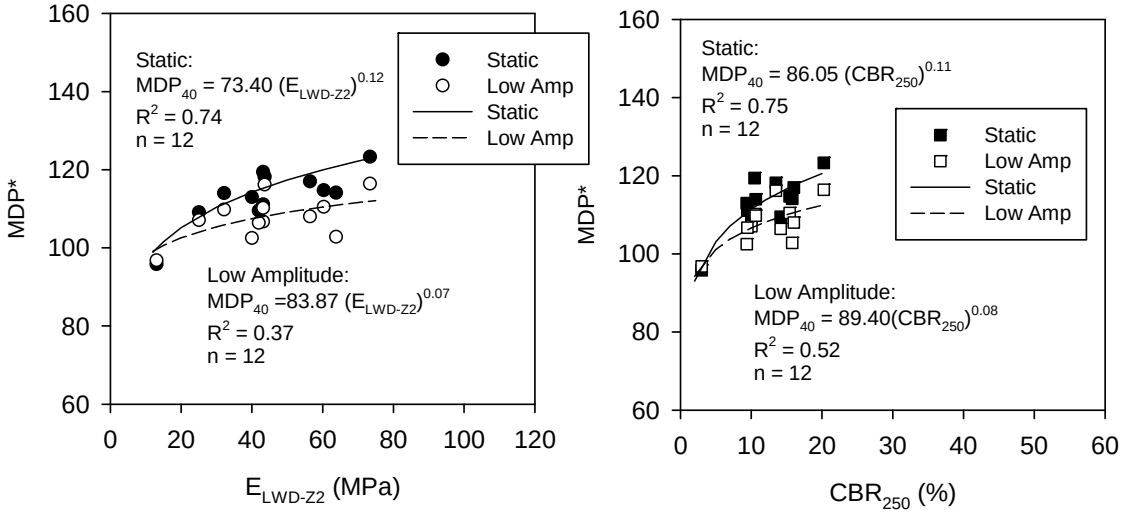

Figure 37. Correlations between MDP* (static and low amplitude) and in-situ point-MVs – TB3

Test bed construction and in-situ testing – TB 7

This test bed consisted of a production area with silty subgrade material scarified to a depth of about 250 mm. Plan dimensions of the test bed are about 6.5 m x 388 m. The area was compacted with 4 to 5 roller passes using the padfoot IC roller in static mode, and followed by one mapping pass in static mode. Nominal machine settings during each pass are summarized in Table 2. Following the final mapping pass, γ_d and *w* point-MVs were randomly obtained from 5 test locations, and DCP-CBR profiles were obtained from two of these locations.

In-situ test results and discussion – TB 7

Figure 38 shows MDP* maps in static mode, elevation map, and pass coverage map for the test bed area. DCP-CBR profiles obtained from two test locations (locations 4 and 5 as marked on the MDP* map) are also shown in Figure 38. Figure 39 shows MDP* and percent target MDP* (assuming a target MDP* = 140) histogram plots. Geostatistical semivariograms of MDP* values from this test bed are presented in Figure 35 along with a summary of the spatial statistics (i.e., nugget, sill, and range). Similar to MDP* values on TB3, the experimental semivariograms values on this test bed showed a nested spatial structure with short-range and long-range components. Nested spherical variograms were fit to the experimental semivariogram data.

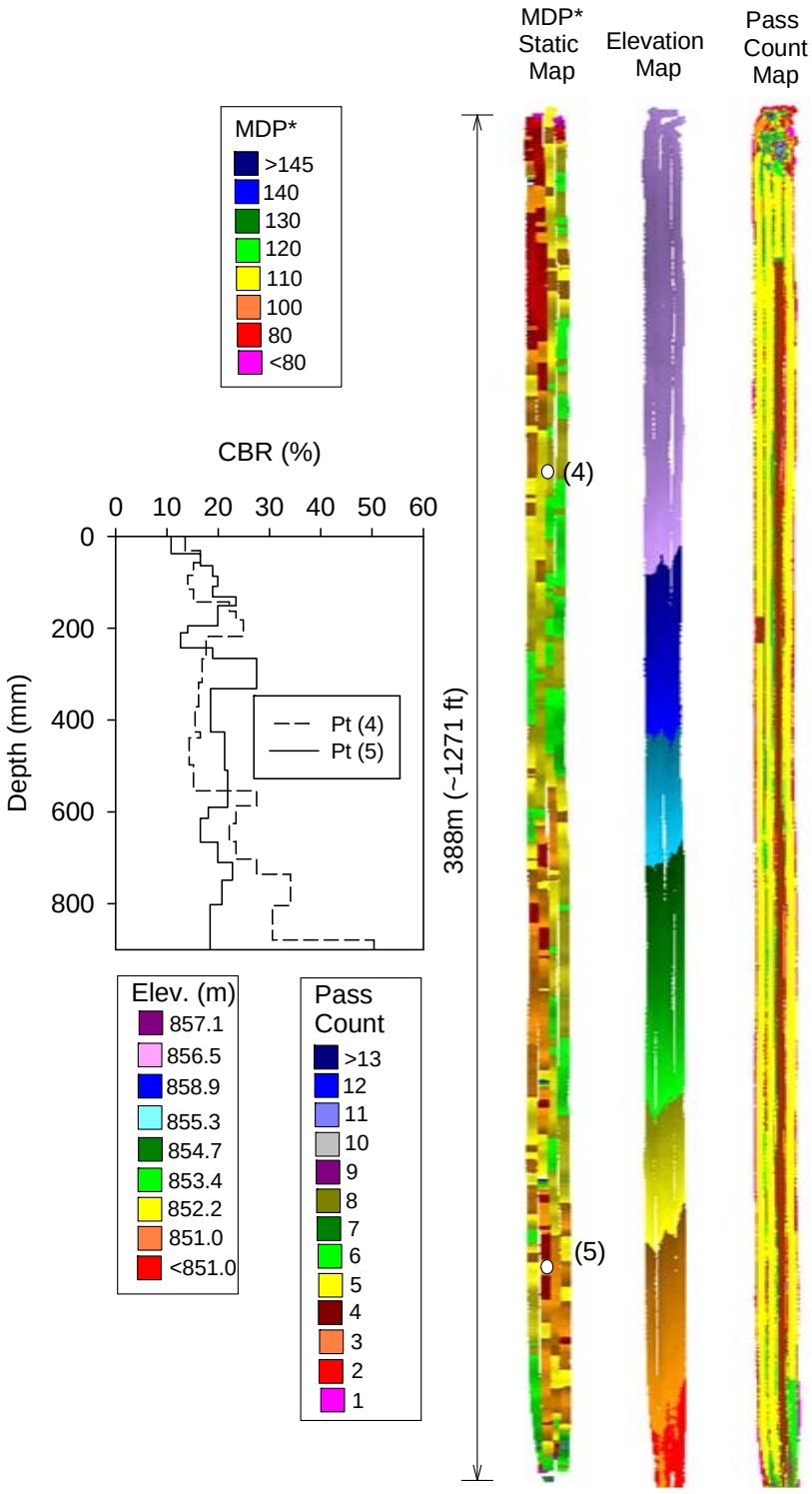

Figure 38. MDP*, elevation, and pass count maps, and CBR profiles at two selected locations – TB7

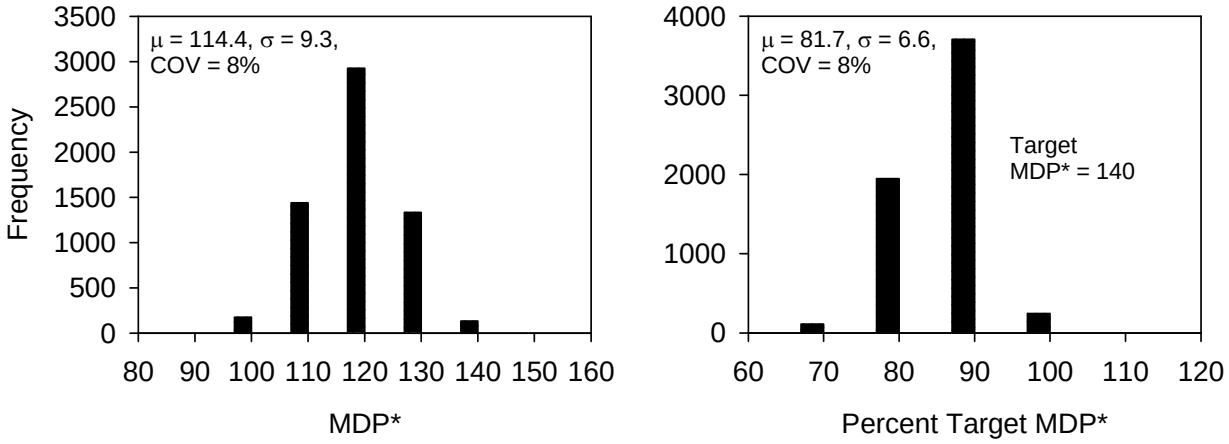

Figure 39. Histograms of MDP* and percent target MDP* of the final mapping pass – TB7

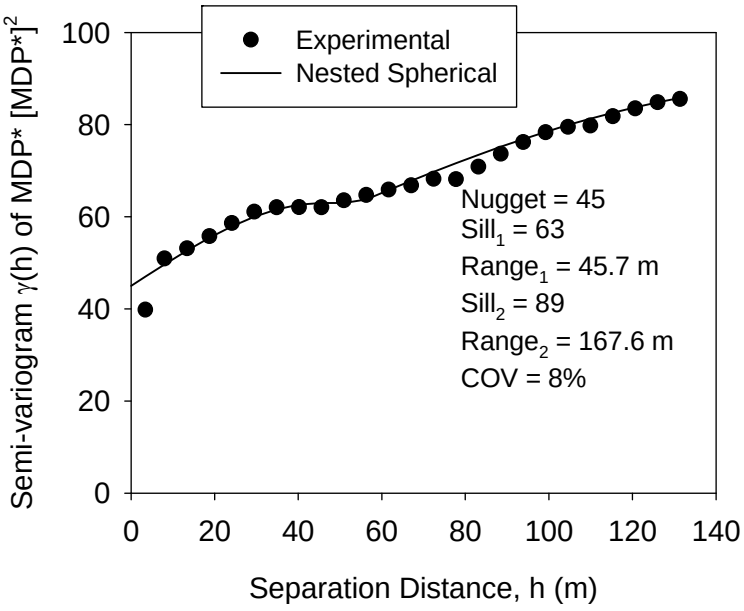

Figure 40. Geostatistical semivariograms of MDP*mapping pass – TB7

The average MDP* value from this test bed (i.e., 114.1) are similar to the average MDP* value from TB3 (i.e., 116.1). The COV of MDP* values were also about the same for the two test beds (COV = 8%). However, the spatial statistics (especially the range values) were substantially different between the two test beds. The MDP* values from this test bed showed more spatial continuity in the data as demonstrated by comparatively longer range values ($range_1$ = 45.7 m and $range_2$ = 167.6 m) compared to TB3 ($range_1$ = 9.1 m and $range_2$ = 56.4 m). The sill values are however somewhat similar for the two test beds. Longer range values represent comparatively more uniform conditions. These differences are not apparent if only univariate statistics (i.e., mean, COV) are assessed.

Figure 41 shows correlations between MDP* and γ_d point-MVs by spatially pairing the nearest point data. No statistically significant relationship was observed in MDP* vs. γ_d point-MVs. The relationship between CBR_{250} and MDP* is note presented here as there were only two measurements.

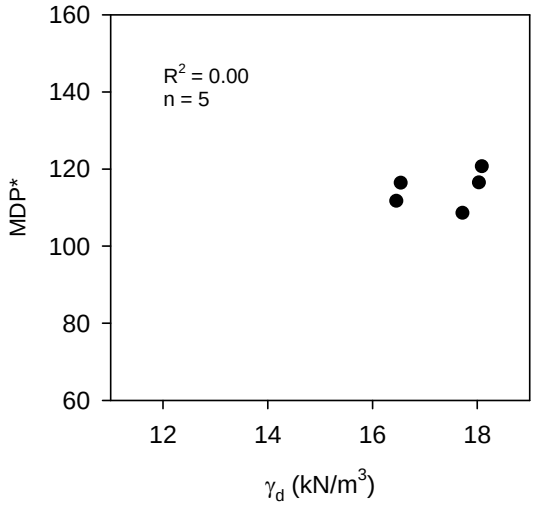

Figure 41. Correlations between MDP* and in-situ γ_d point-MVs – TB7

TBs 4, 5, and 6 Salvage Base Layer Production Compaction (Smooth Drum)

Test beds construction and in-situ testing

TBs 4, 5, and 6 consisted of production areas with two layers of salvage base material placed over an existing layer of subgrade mixed with salvage base material (here after referred to as mixed subgrade). Plan area map of the three test beds is shown in Figure 42. The three areas were located near the Main Street in Marmarth, ND. TB4 was located on the east side of the Main Street on US12 west bound. TB5 was located on the west side of Main Street on US12 west bound. TB6 was located on the east end of TB4. TB4 incorporated two layers of Tensar's TX5 geogrid reinforcement in the salvage base layers while TBs 5 and 6 did not have any reinforcement. TB6 however consisted of a portion of the test bed which was over-excavated and replaced with salvage base material. The objectives of testing on these test beds were to:

- evaluate differences in the IC-MVs and in-situ point-MVs obtained on the salvage base layers constructed with different underlying support conditions (i.e., with and without geogrid reinforcement, and with over excavation (or core-out) and replacement), and
- develop correlations between IC-MVs and in-situ point-MVs.

Smooth drum IC roller was used for mapping and compaction operations on TB4. Compaction operations on TBs 5 and 6 were performed by the contractor using their vibratory smooth drum and static pneumatic rollers. TBs 5 and 6 were mapped using the smooth drum IC roller. The IC roller was equipped to record MDP* and CMV IC-MVs. These two IC-MVs were recorded only on the TB4 subgrade layer. CMV IC-MVs were not recorded on other layers due to hardware problems on the roller.

TB4 consisted of an existing mixed subgrade layer (Figure 43) to a depth of about 250 mm underlain by native soft alluvial deposits with layered silty sand. The mixed subgrade layer was mapped using the smooth drum IC roller using one roller pass each in low amplitude (a = 0.90 mm and f = 30 Hz) and high amplitude (a = 1.80 mm and f = 30 Hz) settings. In addition, in-situ point-MVs (CBR_{250}, $E_{FWD\text{-}K3}$, $E_{FWD\text{-}D3}$, and $E_{LWD\text{-}Z3}$) were obtained on the mixed subgrade layer. TX5 geogrid was placed on the mixed subgrade layer (Figure 43) and approximately 300 mm thick salvage base layer 1 was placed over the geogrid. The layer was graded to the desired elevation using a motor grader and compacted using the smooth drum IC roller. Compaction was achieved using the smooth drum IC roller using three forward and three reverse passes in two roller lanes. Low amplitude settings (a = 0.90 mm and f = 30 Hz) were used for forward passes and static settings were used for reverse passes. A nominal speed of 3.2 km/h was used for forward passes and of 6.0 km/h was used for reverse passes. In-situ point-MVs (γ_d, w, $E_{FWD\text{-}K3}$, $E_{FWD\text{-}D3}$, and $E_{LWD\text{-}Z3}$) were obtained on the compacted base layer 1. Another layer of TX5 geogrid was placed over the compacted base layer 1 and approximately 150 mm thick salvage base layer 2 was placed over the geogrid. Similar to base layer 1, base layer 2 was graded to the desired elevation using a motor grader and compacted using the smooth drum IC roller. Compaction on base layer 2 was achieved in a similar way as on base layer 1. In-situ point-MVs (γ_d, w, CBR_{250}, $E_{FWD\text{-}K3}$, $E_{FWD\text{-}D3}$, and $E_{LWD\text{-}Z3}$) were obtained on the compacted base layer 2. In addition, 2m deep DCP-CBR profile was obtained at one location. A bore hole was drilled at the 2 m deep DCP location to conduct BSTs at various depths in the base and subgrade layers (Figure 44). Bag samples of subgrade and base materials were obtained from BST location at various depths to determine moisture content and percent fines content (% Fines) of the material.

Similar to TB4, TB6 also consisted of an existing mixed subgrade layer to a depth of about 250 mm underlain by native silty subgrade material. A portion of the test bed area was unstable under the construction equipment. The area that was unstable was over excavated to a depth of about 250 mm and was replaced with salvage base material. Compaction of these layers was achieved using Contractor's padfoot roller. Additional salvage base layers (with a total thickness of about 800 mm) were placed and compacted above the existing grade to match with the final grade of the adjacent TB4. The final layer is referred to as salvage final base layer. Compaction operations were performed on this test bed using contractor's equipment. The area was mapped using low amplitude settings (a = 0.90 mm and f = 30 Hz) in two roller lanes. In-situ point-MVs (γ_d, w, CBR_{250}, $E_{FWD\text{-}K3}$, $E_{FWD\text{-}D3}$, and $E_{LWD\text{-}Z3}$) were obtained on the final base layer. In addition, a 2m deep DCP-CBR profile was obtained in the core- out area. A bore hole was drilled at the DCP location to conduct BSTs at various depths in the base and subgrade layers. Bag samples of subgrade and base materials were obtained from various depths to determine moisture content and percent fines content (% Fines) of the material.

TB5 consisted of a compacted salvage base layer (Figure 45). No geogrid reinforcement was used in TB5. The base layer was reportedly compacted using pneumatic roller (Figure 45). After compaction operations, the area was mapped using low amplitude settings (a = 0.90 mm and f = 30 Hz) in two roller lanes on 08/10/2010 (Day 1) and 08/11/2010 (Day 2). After mapping passes on day 1, the TB5 area was used by haul trucks and other construction traffic, and moisture was added several times for dust control. The area was also left open to traffic at the end of day 1. In-situ point-MVs ($E_{FWD\text{-}K3}$ and $E_{LWD\text{-}Z3}$) were obtained on the compacted final base layer after the mapping passes on day 2.

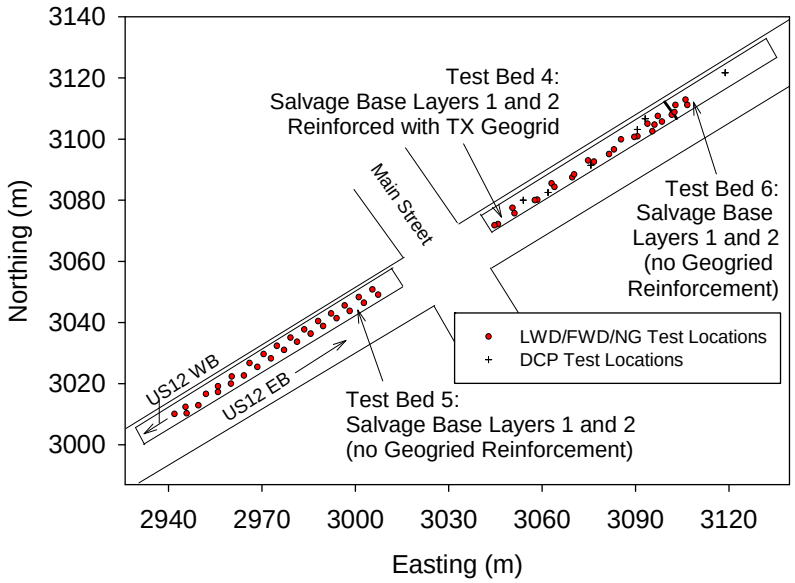

Figure 42. Map of test beds 4, 5, and 6, and in-situ testing locations

Figure 43. Photographs of TB4 during placement of TX5 geogrid and salvage base layers and

Figure 44. Photographs of drilling equipment and bore hole drilled for BST on TB4

Figure 45. TB5 location (left) and pneumatic roller used for compaction of base layer on TB5 (right)

Test results and discussion

IC-MV and elevation maps on TB4 subgrade and salvage base layers 1 and 2 are presented in Figure 46. IC-MV and elevation maps of TBs 5 and 6 final salvage base layers are presented in Figure 47 and Figure 48, respectively. The approximate limits of core-out on TB6 are shown in Figure 48. A summary of IC-MV and in-situ point-MV statistics on TB4 mixed subgrade and salvage base layers, and TBs 5 and 6 salvage base layers is presented in Table 4. Summary statistics for TB6 are presented separately for the measurements in the core-out area and outside the core-out area.

Results from TB4 (geogrid reinforced section)

Comparison between MDP* and CMV IC-MVs and in-situ point MVs on the TB4 subgrade layer are presented in Figure 49 to Figure 52. CMV IC-MVs showed relatively high variability

(COV = 78 to 87%) compared to MDP* IC-CMVs (COV = 2%) on the subgrade layer. The in-situ modulus and CBR_{250} point-MVs showed COV ranging between 30% and 64%. DCP-CBR profiles performed at four locations on the TB4 subgrade layer are presented in Figure 53. Lane 2 showed a relatively stiff zone (with CMV > 35) between 55 m and 70 m and some relatively soft zones (with CMV < 10) between 15 m and 22 m and between 34 m and 45 m. MDP* IC-MVs did not show much variation in these zones. DCP and $E_{LWD\text{-}Z3}$ tests were conducted in these zones, which confirmed the variations observed in the CMV IC-MVs. DCP 2 located in the stiff zone showed CBR_{250} =73, while DCP 1 located in the soft zone showed CBR_{250} = 20. The average $E_{LWD\text{-}Z3}$ in the stiff zone was about 91 MPa (based on 4 measurements), while in soft zone was about 60 MPa (based on 3 measurements). Variations in the points-MVs across the test bed lanes corroborated well with the variations in CMV IC-MVs. On the other hand, MDP* IC-MVs did not capture these variations.

Average MDP* compaction curves for TB4 salvage base layer 1 are presented in Figure 54. Results indicated slightly different trends in the MDP* compaction growth for forward (in low amplitude mode) and reverse (in static mode) passes. MDP* raw data plots for each compaction pass on lanes 1 and 2 are presented in Figure 55. These plots indicate that the MDP* IC-MVs are repeatable and increase with increasing number of passes. The MDP* values are on average higher in reverse passes (made at an average speed = 6.1 km/h) than in forward passes (made at an average speed = 3.2 km/h), which indicates that the values are affected by the machine speed settings. Previous research (White et al. 2009) also indicated that the MDP* IC-MVs are influenced by the machine travel speed. Comparison between MDP* IC-MVs and in-situ point MVs on base layer 1 are presented in Figure 56 and Figure 57. The average relative compaction of the base material was about 90% of AASHTO T-180 γ_{dmax}. These results and summary statistics presented in Table 4 indicate that the MDP* IC-MVs and the point-MVs are relatively higher and less variable on base layer 1 than on the underlying mixed subgrade layer. The COV of MDP* IC-MV reduced slightly from 2% to 1%, but the COV of $E_{LWD\text{-}Z3}$ reduced from 30% to 14%, $E_{FWD\text{-}D3}$ reduced from 51% to 20%, and $E_{FWD\text{-}K3}$ reduced from 37% to 23%.

Average MDP* compaction curves for TB4 salvage base layer2 are presented in Figure 58. Similar to results on the base layer 1, the average MDP* compaction curves on base layer 2 indicated different trends for forward (in low amplitude mode) and reverse (in static mode) passes. MDP* raw data plots for each compaction pass on lanes 1 and 2 are presented in Figure 59. The MDP* IC-MVs in reverse direction are generally higher than in forward direction but with exception in one zone (between 15 m and 25 m on lanes 1 and 2) on pass 6 where the reverse pass speed was reduced to about 3 km/h (Figure 59). Comparison between MDP* IC-MVs and in-situ point-MVs on base layer 2 are presented in Figure 60 and Figure 61. These results and summary statistics presented in Table 4 indicate that on average the point-MVs are higher on base layer 2 than on the underling base layer 1 and mixed subgrade. The modulus measurements were about 1.1 to 1.4 times higher on base layer 2 than on base layer 1, while the average relative compaction was about the same (90% of AASHTO T-180 γ_{dmax}) on the two base layers. COV of E_{FWD} measurements are slightly lower on base layer 2 while the COV of $E_{LWD\text{-}Z3}$ measurements are slightly higher on base layer 2, when compared to the COV of these measurements on base layer 1. The average MDP* and COV of MDP* were about the same on base layers 1 and 2. DCP-CBR profiles obtained from four locations (DCP 1, 2, 5, and 6) are presented in Figure 62. Note that the DCP tests were performed at the same locations as

identified on the underlying mixed subgrade layer. DCP test conducted at DCP2 location again confirmed the stiff location with high CBR values (CBR > 100) noted earlier in the mixed subgrade layer. Results from a 2m long DCP test and BST results at various depths at DCP1 test location are presented in Figure 63. Variations observed in the BST results (effective cohesion *c'* and effective angle of internal friction ϕ') in the base and subgrade layers corroborate well with the variations observed in the CBR values with depth.

Results from TB6 (control and core-out sections)

MDP* IC-MVs and point-MVs obtained on the final layer of salvage base material on TB6 are presented in Figure 60 and Figure 61 in comparison with measurements from TB4. The core-out limits on the test bed are also shown in Figure 60 and Figure 61, for reference. In the control section (i.e., outside the core-out area), results indicate that the average MDP* IC-MVs was lower (by about 1.06 times) and the COV of MDP* was greater than on TB4 (1% on TB4 and 4% on TB6). The $E_{LWD\text{-}Z3}$, $E_{FWD\text{-}K3}$, and $E_{FWD\text{-}D3}$ point-MVs in the control section were also on average lower (by about 1.1 to 1.6 times) than on TB4. However, it must be noted that only limited number of point-MVs (1 to 4) were obtained in this area.

A 2 m DCP and a FWD measurement were obtained in the core-out area. The CBR_{250} and $E_{FWD\text{-}K3}$ point-MVs at that location were comparatively higher (CBR_{250} by about 1.5 times and $E_{FWD\text{-}K3}$ by about 1.7 times) than on TB4, but the MDP* IC-MVs in the core-out location were slightly lower (by about 1.06 times) than on TB4. Figure 63 shows the 2m deep DCP profile in the core-out location (DCP4) along with *c'* and ϕ' values determined from BST at various depths in the base and subgrade layers. 1 m deep DCP profile conducted before core-out is also presented in Figure 63 for reference. Similar to observation above in DCP1 (TB4), the variations observed in the BST results (i.e., *c'* and ϕ') in the base and subgrade layers corroborate well with the variations observed in the CBR profile with depth.

Results from TB5 (control section)

Comparison between MDP* and in-situ point MVs on the TB5 final salvage base layer (control section) are presented in Figure 64 and Figure 65. MDP* IC-MVs obtained on TB5 on day 1 and on day 2 (i.e., after trafficking) are presented separately. On average, MDP* IC-MVs obtained on day 2 are about 1.06 times greater than on day 1. The reason for this increase in MDP* on day 2 is attributed to possible compaction under haul trucks and other construction vehicles.

MDP* IC-MVs were slightly lower (by about 1.04 times) than on TB4. The $E_{FWD\text{-}K3}$ point-MVs were also on average slightly lower (by about 1.1 times) than on TB4, while the average $E_{LWD\text{-}Z3}$ point-MVs were about the same on TBs 4 and 6. The COV of MDP* IC-MVs and point-MVs on TBs 4 and 5 were quite similar.

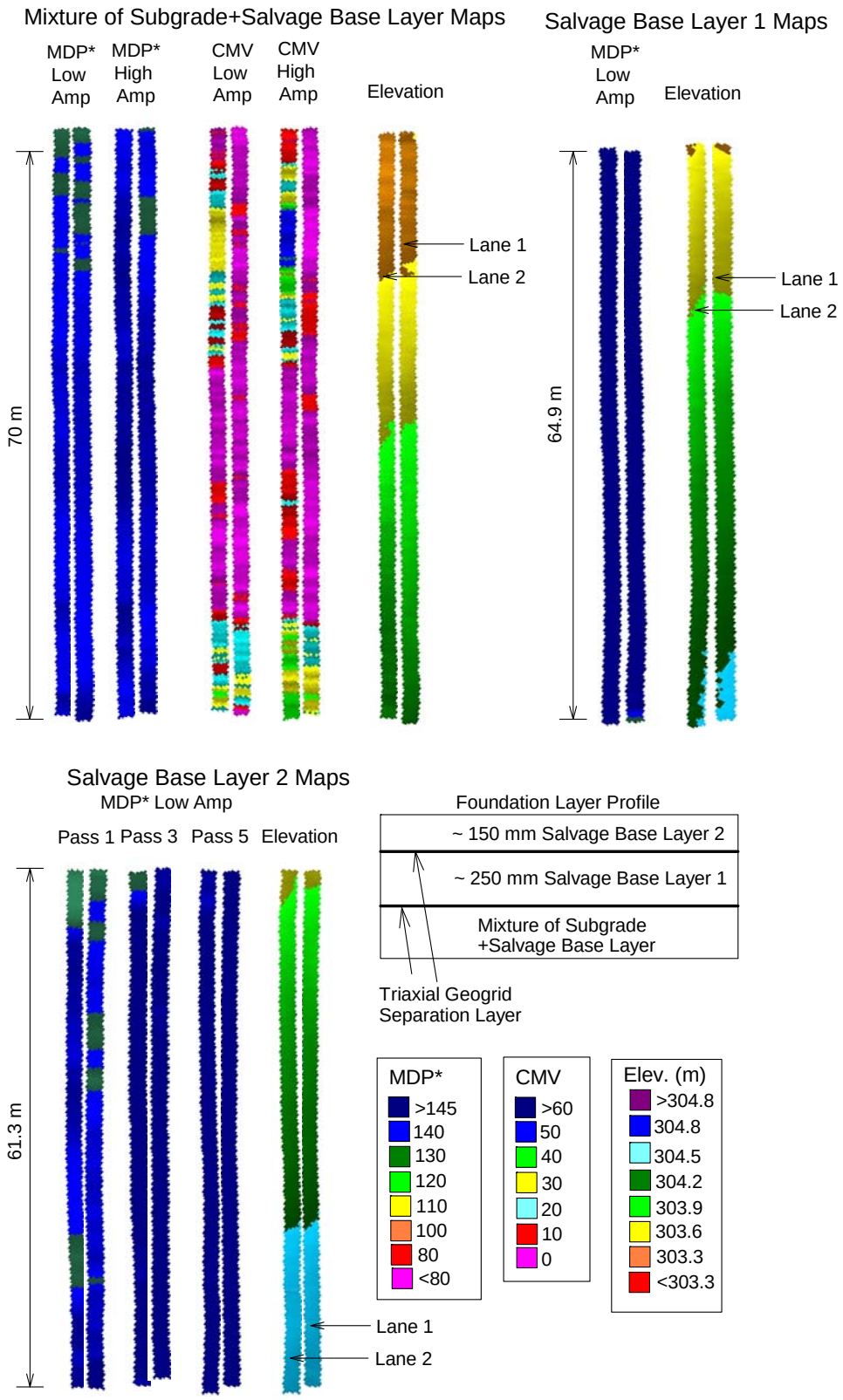

Figure 46. MDP*, CMV, and elevation maps on mixture of subgrade+salvage base layer, and MDP* and elevation maps on salvage base layers 1 and 2 – TB4

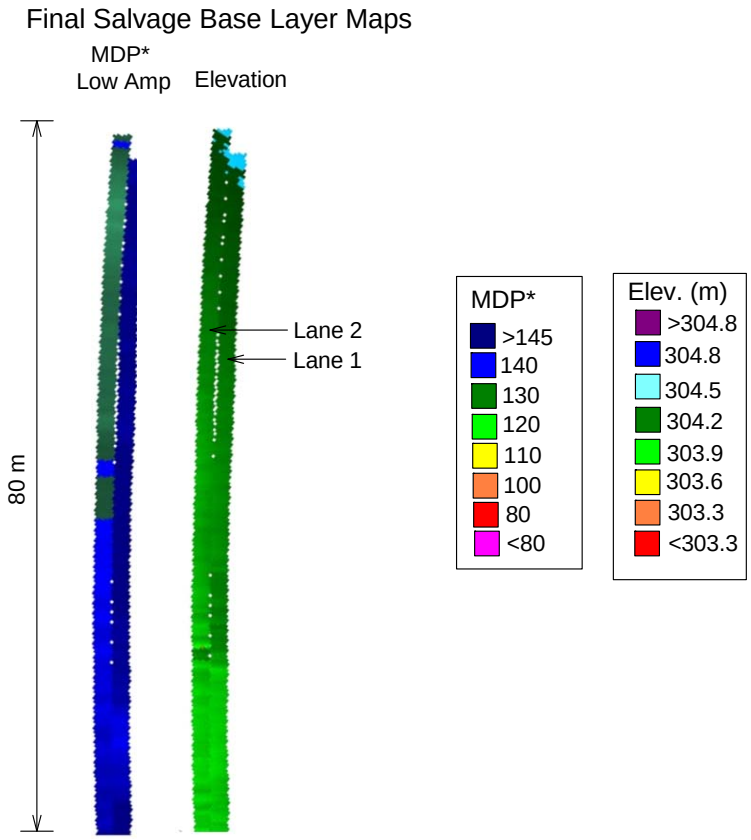

Figure 47. MDP* and elevation maps on final salvage base layer – TB5

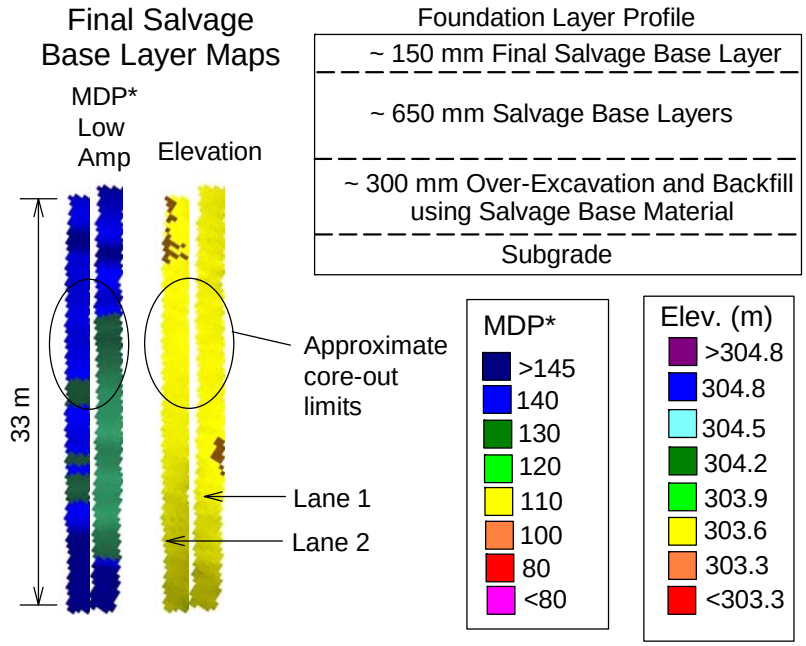

Figure 48. MDP* and elevation maps on final salvage base layer – TB6

Table 4. Summary statistics of measurements from TBs 4, 5, and 6

Test Bed	Layer	Measurement	n	μ	σ	COV (%)
TB4 (with geogrid)	Mixture of subgrade + salvage base	MDP* (a = 0.90 mm)	793	142.5	2.3	2
		CMV (a = 0.90 mm)	793	12.8	10.0	78
		MDP* (a = 1.80 mm)	736	145.5	2.8	2
		CMV (a = 1.80 mm)	736	17.6	15.3	87
		$E_{LWD\text{-}Z3}$ (MPa)	32	72.5	21.7	30
		$E_{FWD\text{-}K3}$ (MPa)	9	78.1	40.1	51
		$E_{FWD\text{-}D3}$ (MPa)	9	85.7	31.6	37
		CBR_{250} (%)	5	36	23	64
		γ_d (kN/m^3)	No Measurements			
		w (%)	No Measurements			
	Salvage base layer 1	MDP*	672	148.4	1.2	1
		$E_{LWD\text{-}Z3}$ (MPa)	32	92.2	13.2	14
		$E_{FWD\text{-}K3}$ (MPa)	9	98.0	20.3	20
		$E_{FWD\text{-}D3}$ (MPa)	9	125.3	29.3	23
		CBR_{250} (%)	No Measurements			
		γ_d (kN/m^3)	22	19.23	0.18	1
		w (%)	22	8.5	0.5	5
	Salvage base layer 2	MDP*	633	147.5	1.4	1
		$E_{LWD\text{-}Z3}$ (MPa)	32	99.7	16.8	17
		$E_{FWD\text{-}K3}$ (MPa)	21	134.5	25.8	19
		$E_{FWD\text{-}D3}$ (MPa)	9	160.6	19.7	12
		CBR_{250} (%)	5	19	4	23
		γ_d (kN/m^3)	22	19.34	0.24	1
		w (%)	22	8.0	4.2	5
TB5-1	Final salvage base layer	MDP*	747	133.2	3.5	3
TB5-2 (control section with no geogrid)	Final salvage base layer (*after trafficking*)	MDP*	749	141.9	3.8	3
		$E_{LWD\text{-}Z3}$ (MPa)	30	101.1	19.9	19
		$E_{FWD\text{-}K3}$ (MPa)	30	122.2	26.7	22
TB6 (control section with no geogrid and partial core-out)	Final salvage base layer	MDP*[a]	187	141.0	5.6	4
		MDP*[b]	83	138.8	3.5	3
		$E_{LWD\text{-}Z3}$ (MPa) [a]	4	69.3	17.3	25
		$E_{FWD\text{-}K3}$ (MPa) [a]	2	79.7	38.2	48
		$E_{FWD\text{-}K3}$ (MPa)[b]	1	224.1	Not applicable	
		$E_{FWD\text{-}D3}$ (MPa)[a]	1	145.2		
		CBR_{250} (%)[b]	1	29		
		γ_d (kN/m^3)[a]	1	19.09		
		w (%)[a]	1	9.1		

[a]Measurements outside the core-out area; [b]Measurements in the core-out area

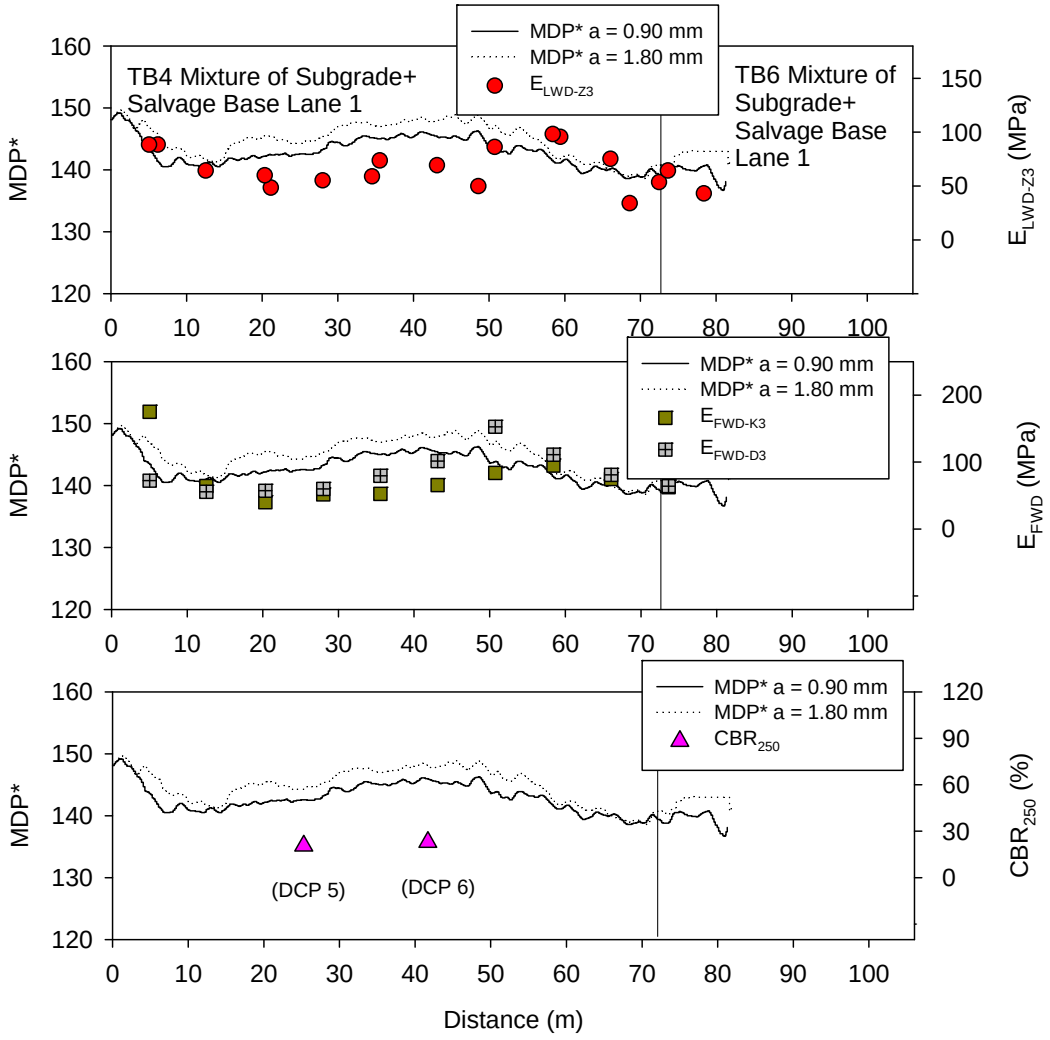

Figure 49. Comparison of MDP* and in-situ point measurements on mixture of subgrade + salvage base layer lane 1 – TB4

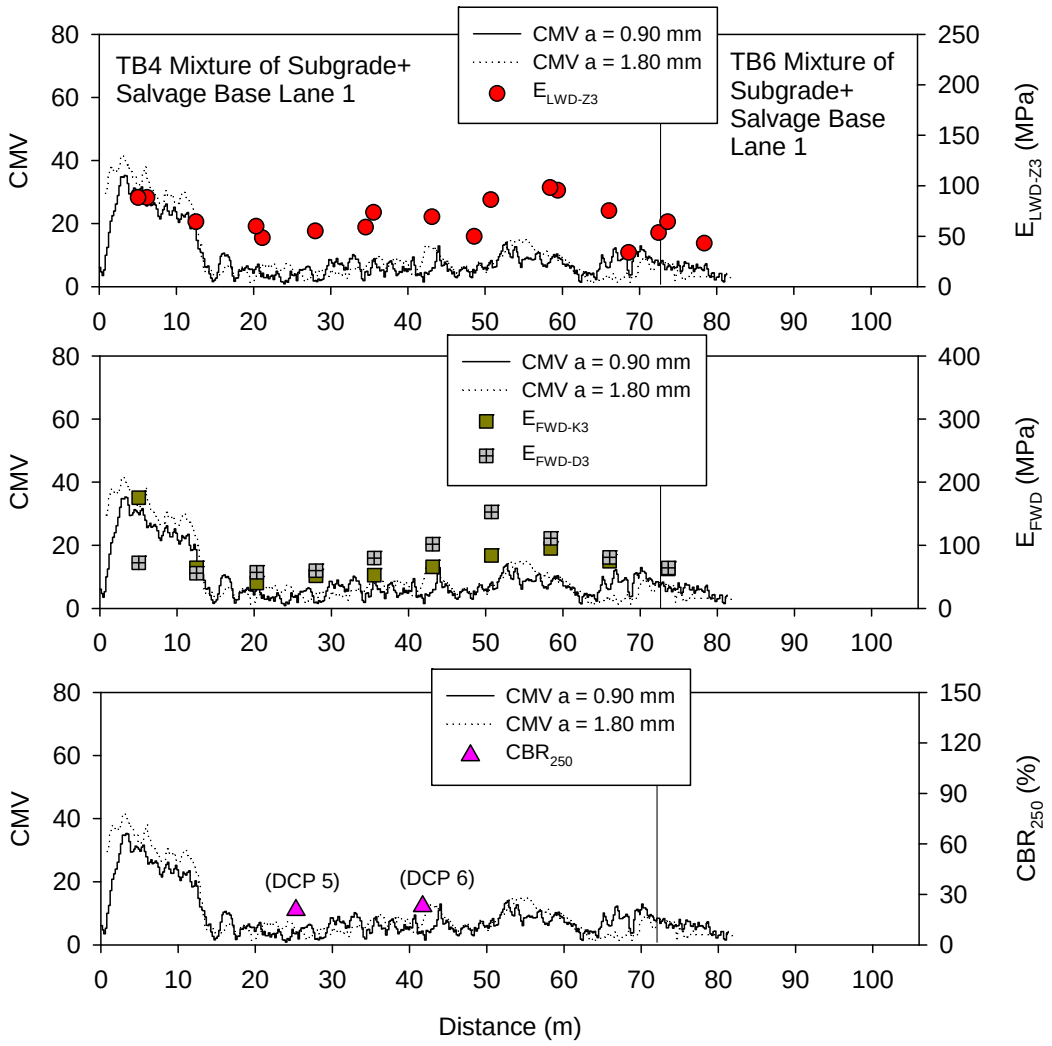

Figure 50. Comparison of CMV and in-situ point measurements on mixture of subgrade + salvage base layer lane 1 – TB4

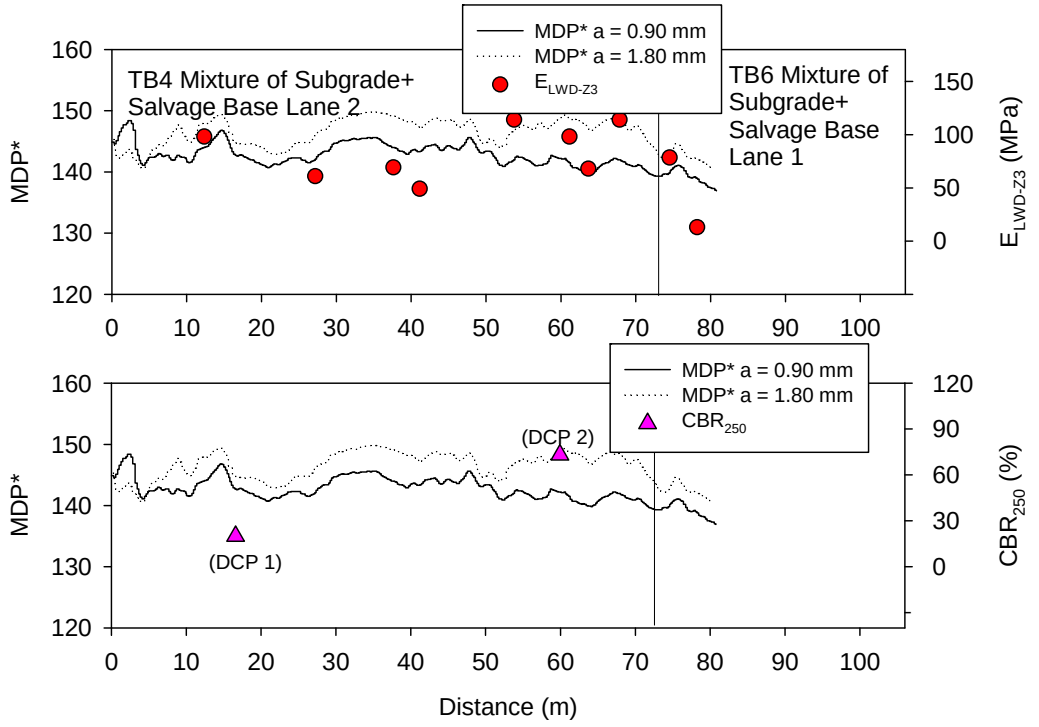

Figure 51. Comparison of MDP* and in-situ point measurements on mixture of subgrade + salvage base layer lane 2 – TB4

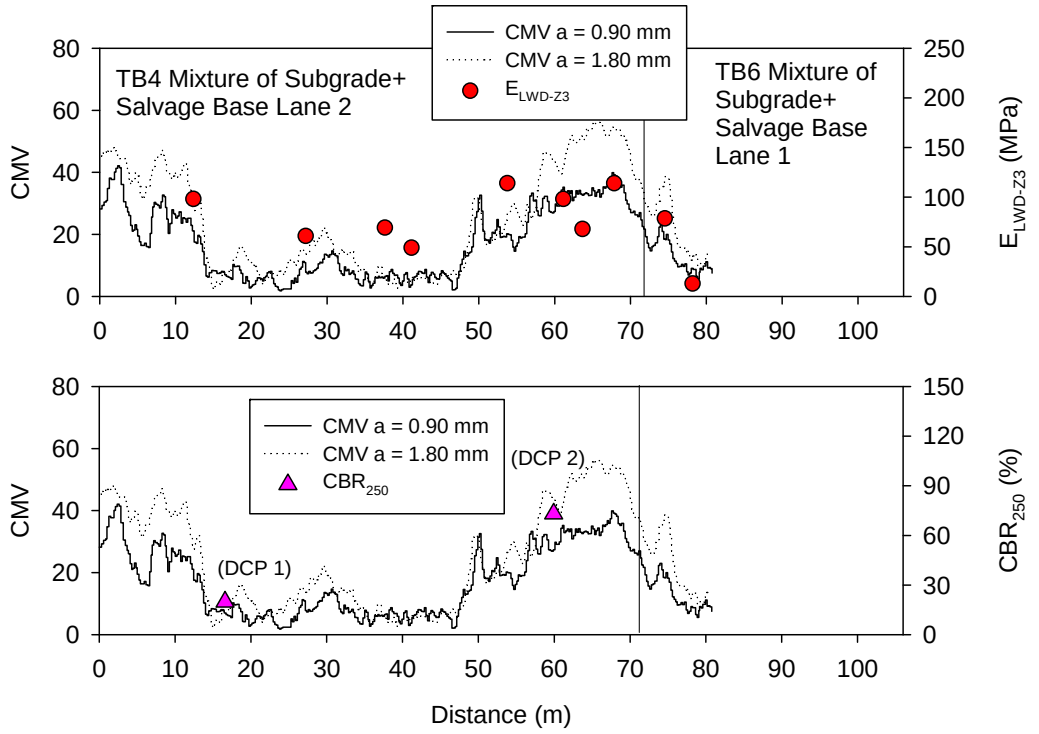

Figure 52. Comparison of CMV and in-situ point measurements on mixture of subgrade + salvage base layer lane 2 – TB4

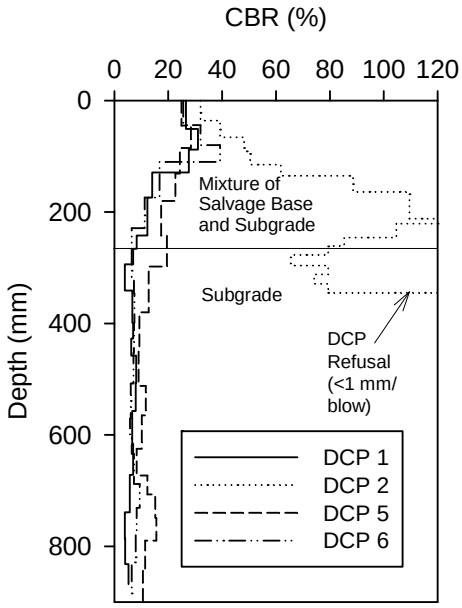

Figure 53. DCP-CBR profiles on mixture of subgrade + salvage base – TB4

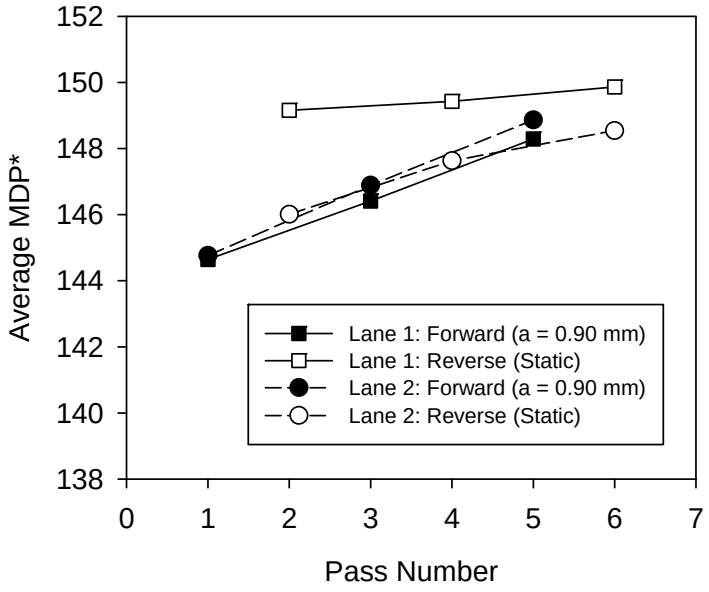

Figure 54. MDP* compaction curves on salvage base layer 1 – TB4

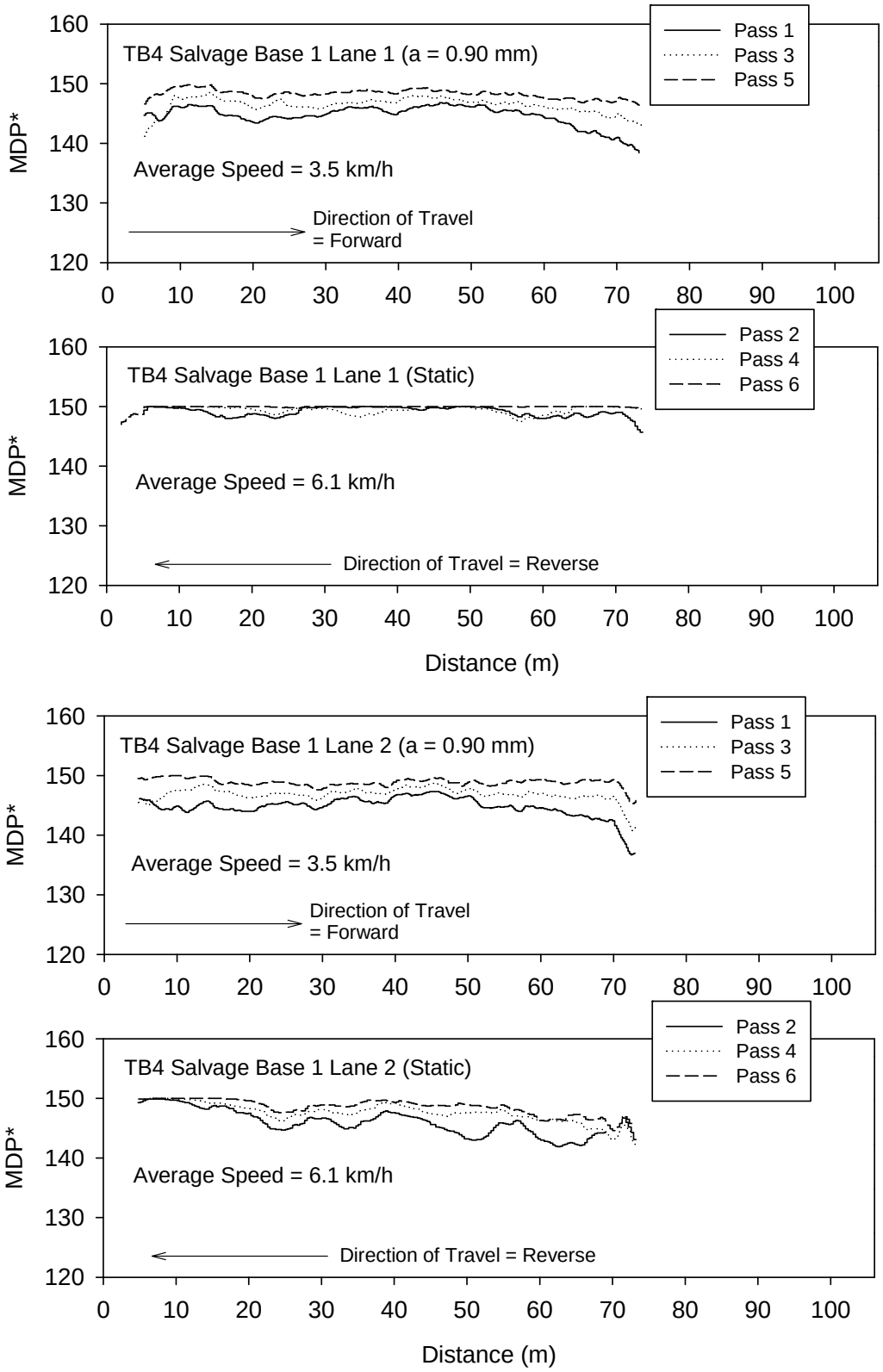

Figure 55. MDP* measurements for multiple passes on lanes 1 and 2 on salvage base layer 1 – TB4

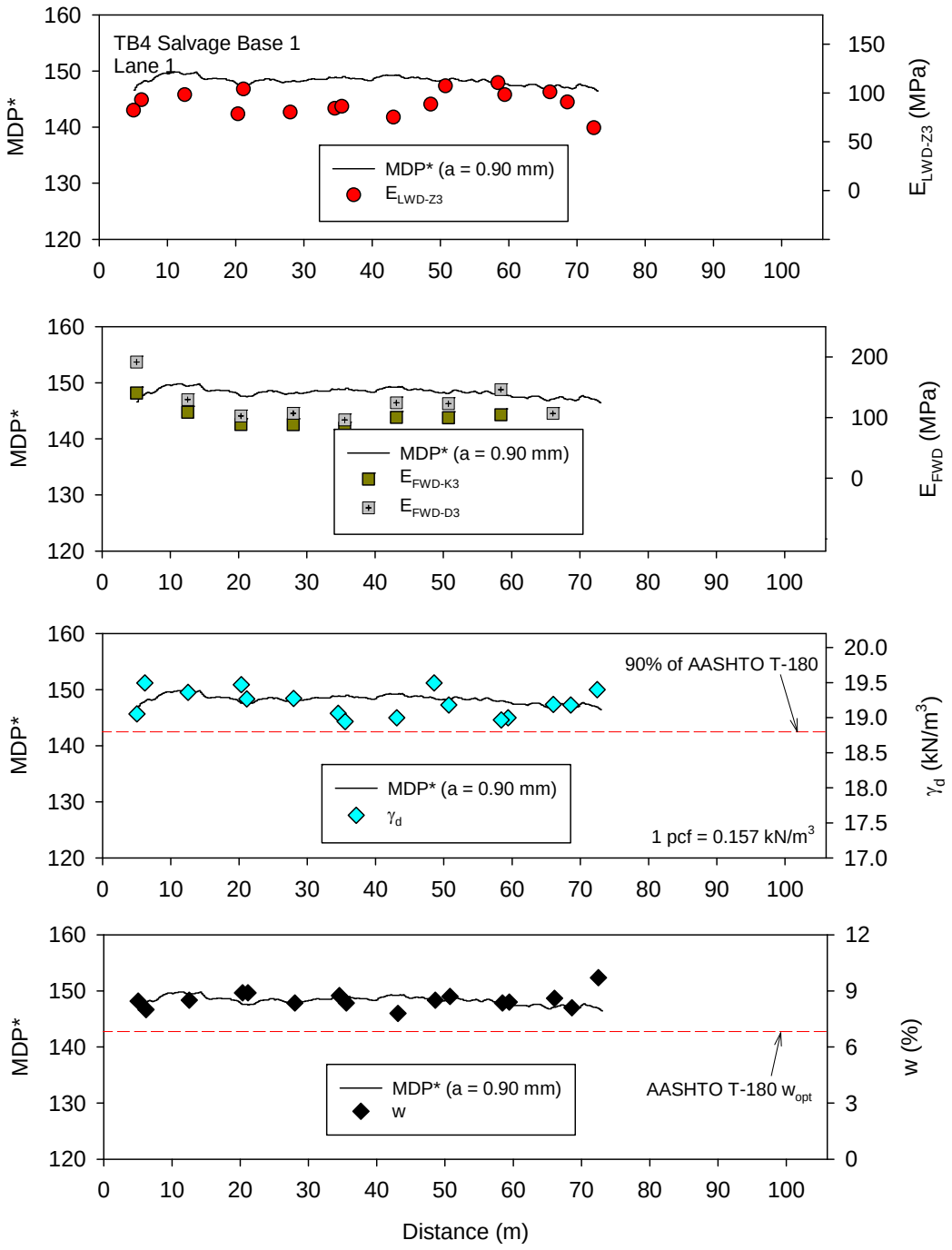

Figure 56. Comparison of MDP* measurements and in-situ point measurements on salvage base layer 1 lane 1 – TB4

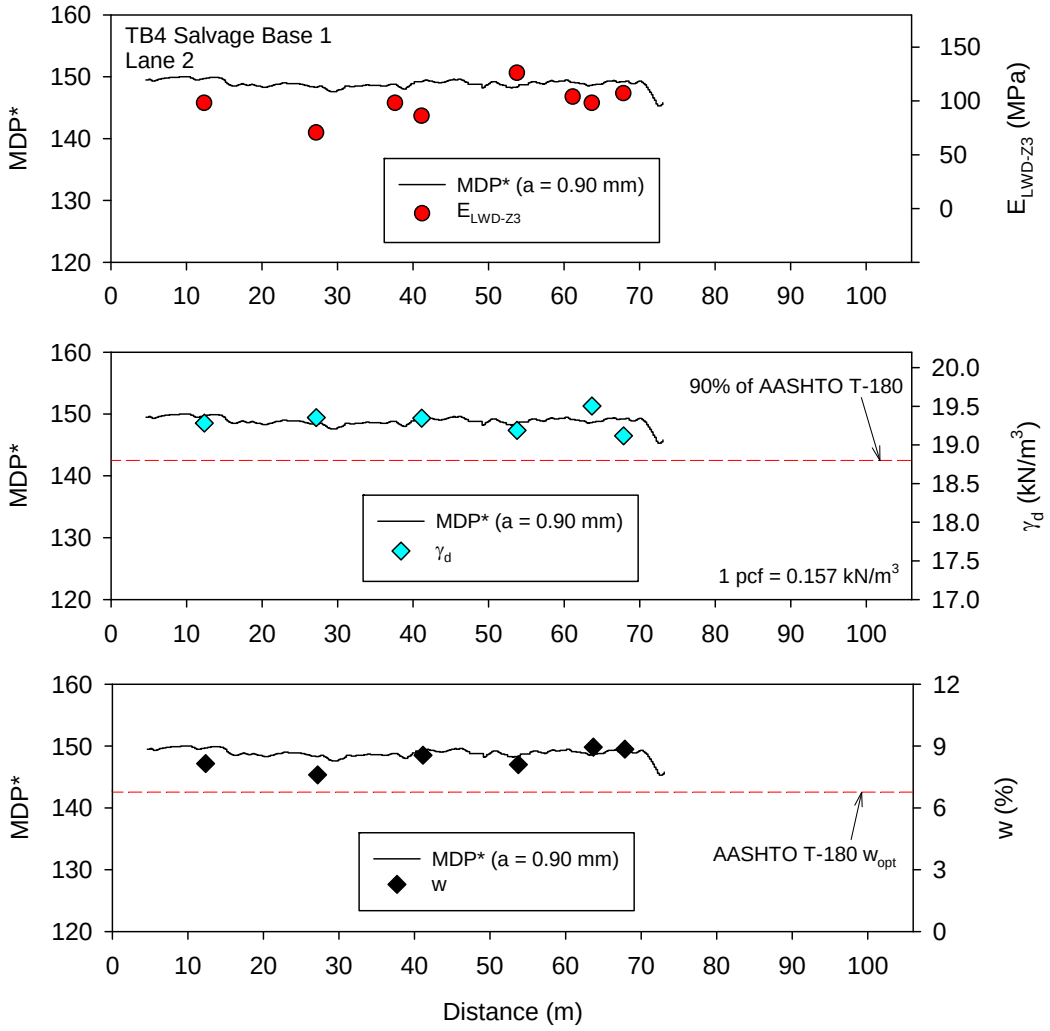

Figure 57. Comparison of MDP* measurements and in-situ point measurements on salvage base layer 1 lane 2 – TB4

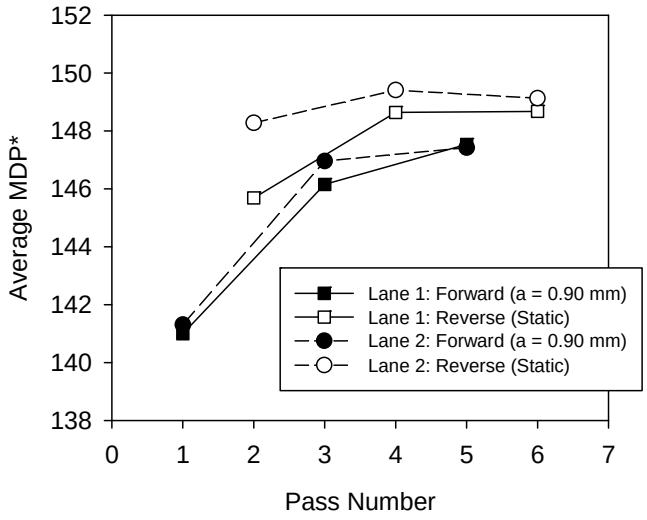

Figure 58. MDP* compaction curves on salvage base layer 2 – TB4

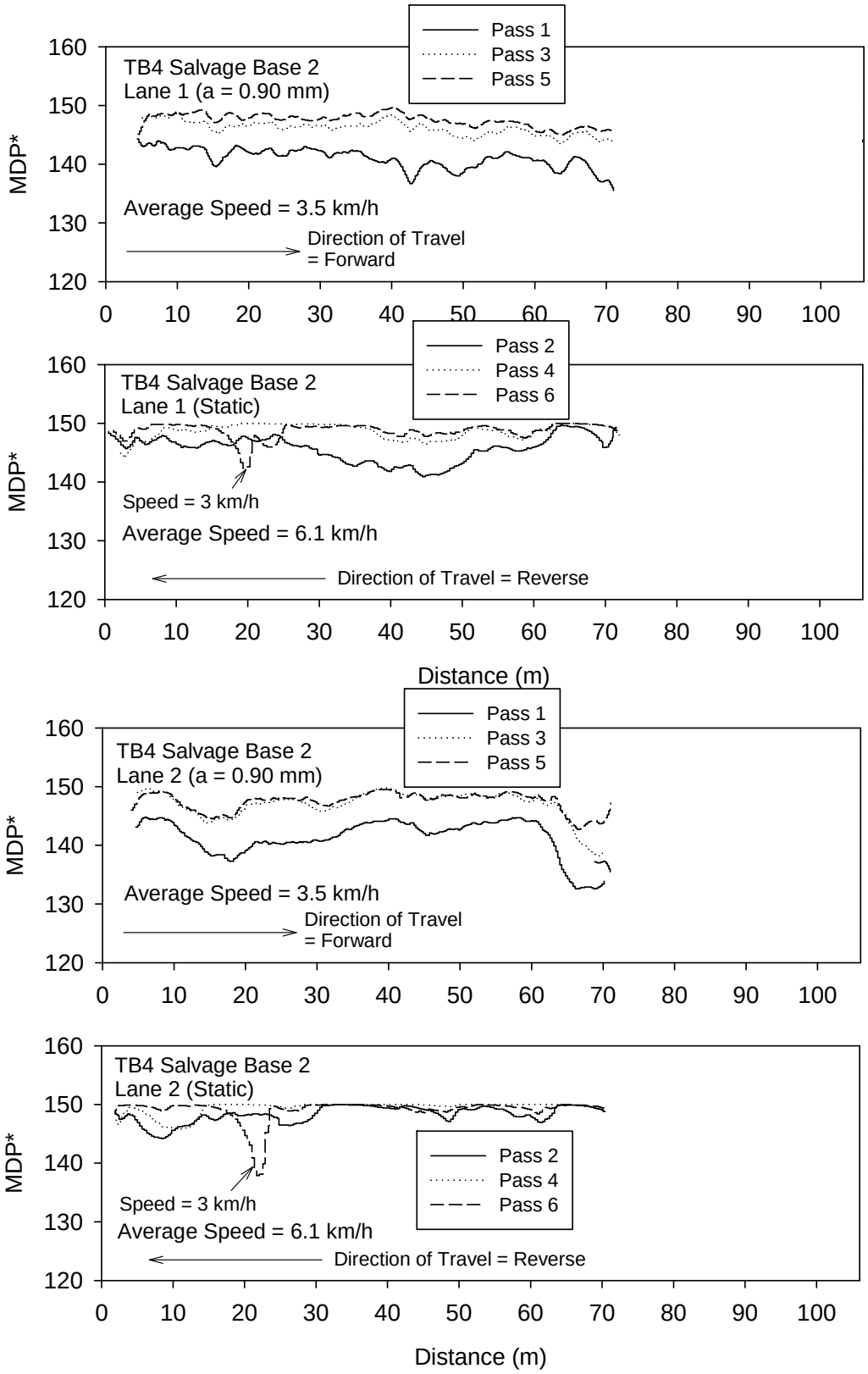

Figure 59. MDP* measurements for multiple passes on lanes 1 and 2 on salvage base layer 2 – TB4

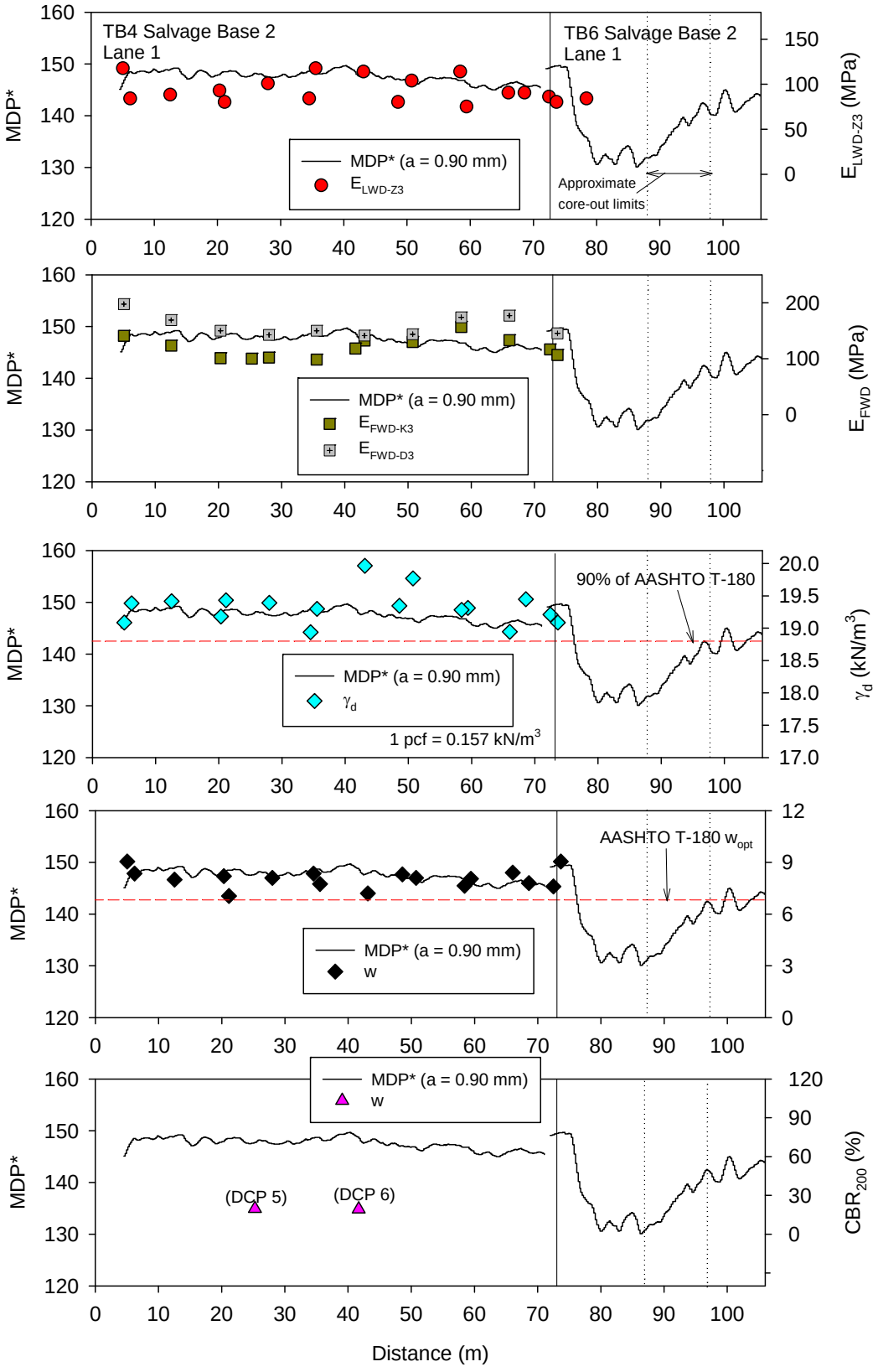

Figure 60. Comparison of MDP* measurements and in-situ point measurements on salvage base layer 2 lane 1 – TBs 4 and 6

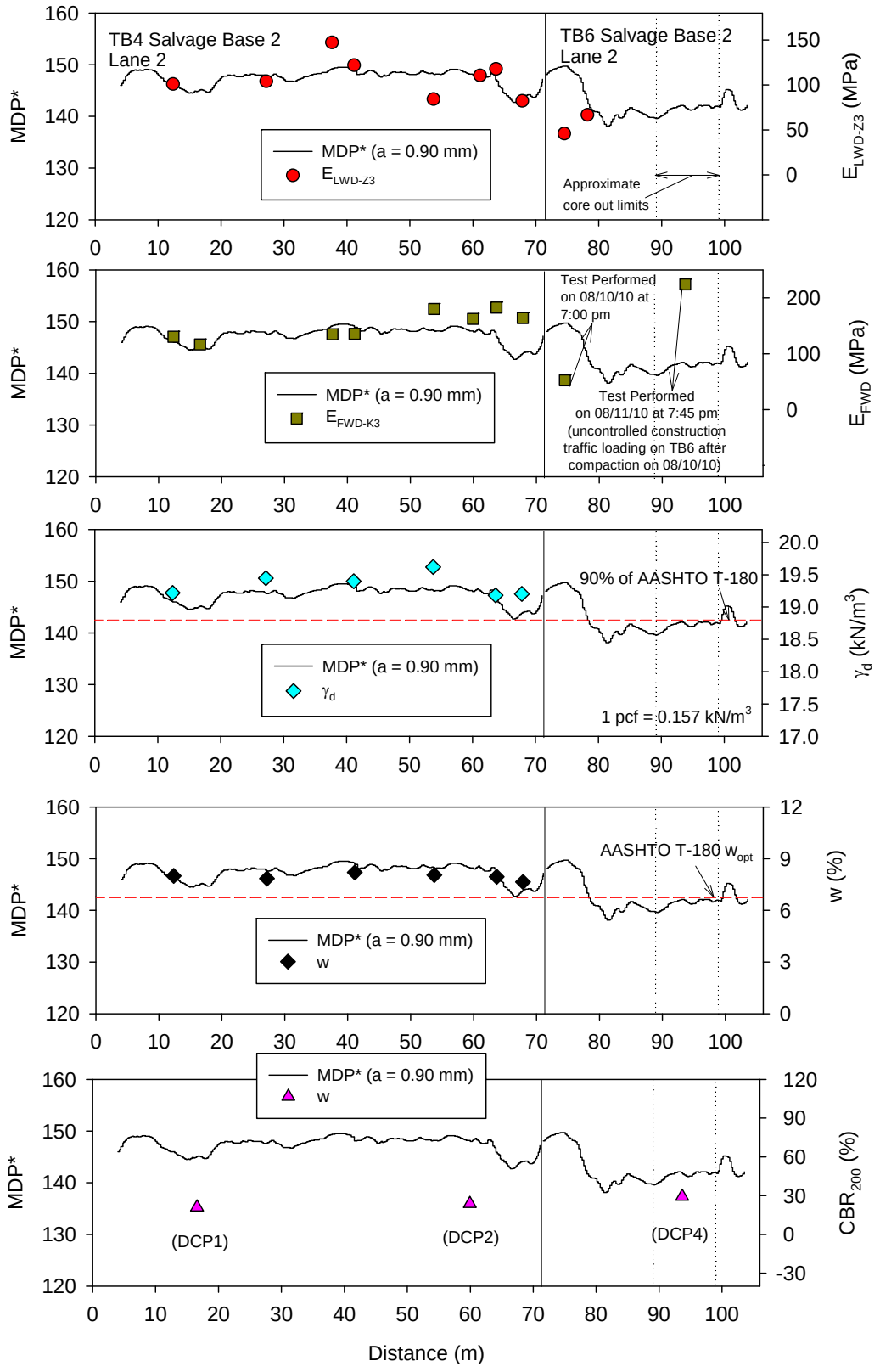

Figure 61. Comparison of MDP* measurements and in-situ point measurements on salvage base layer 2 lane 2 – TBs 4 and 6

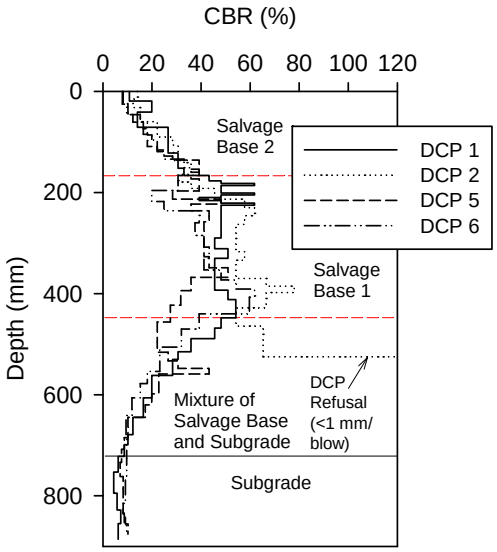

Figure 62. DCP-CBR profiles on salvage base layer 2 lane 2 – TB4

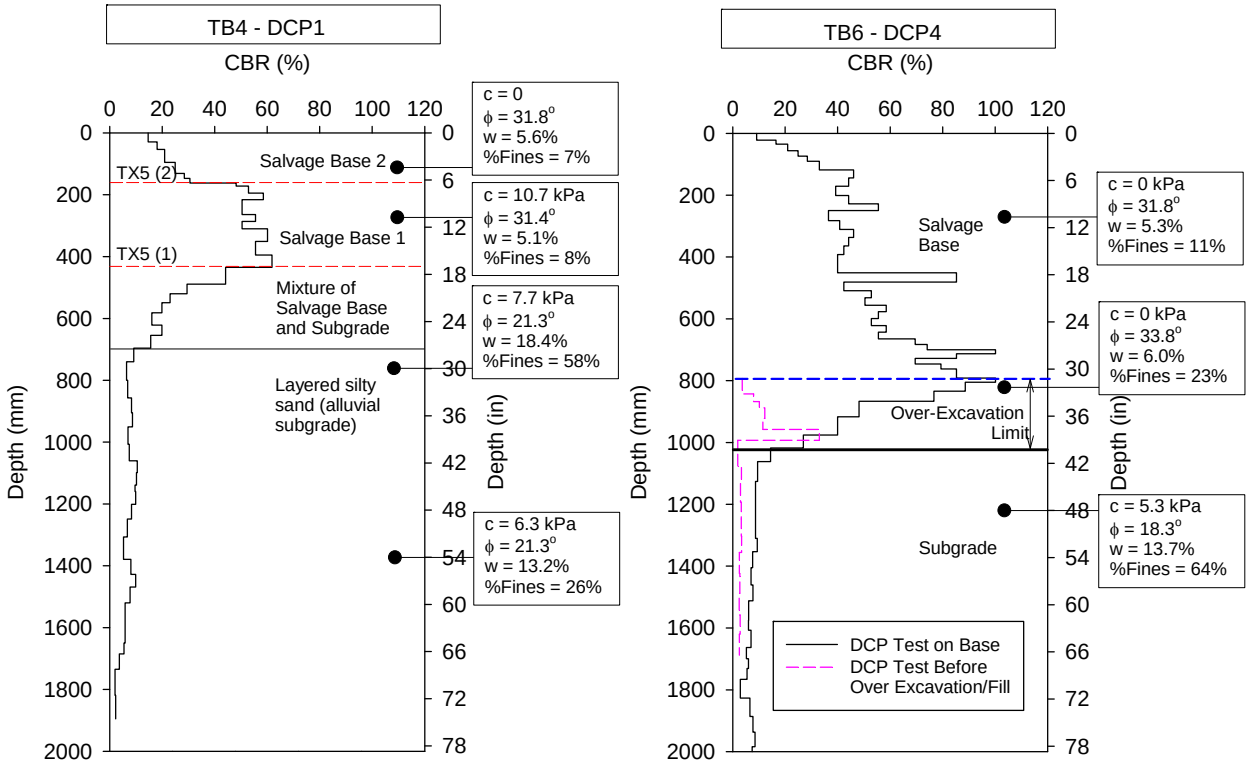

Figure 63. Comparison of DCP-CBR profiles and BST results on salvage base layer 2 lane 2 from TB4 (with TX5 geogrid) and TB6 (over excavation and replacement in subgrade)

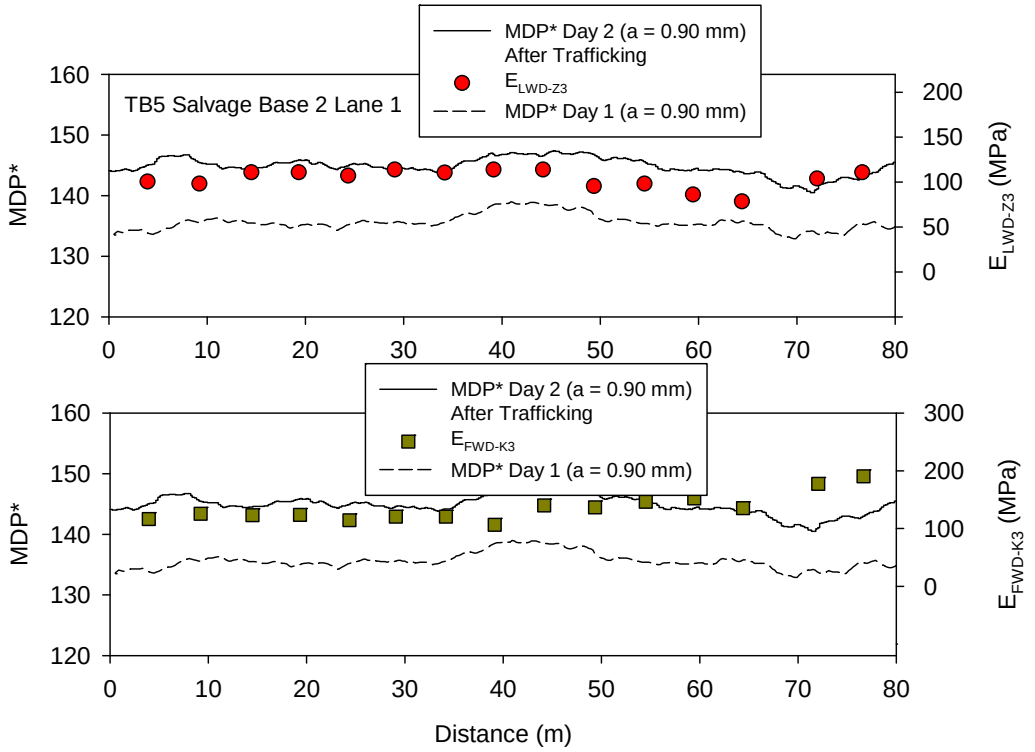

Figure 64. Comparison of MDP* measurements and in-situ point measurements on final salvage base layer lane 1 – TB5

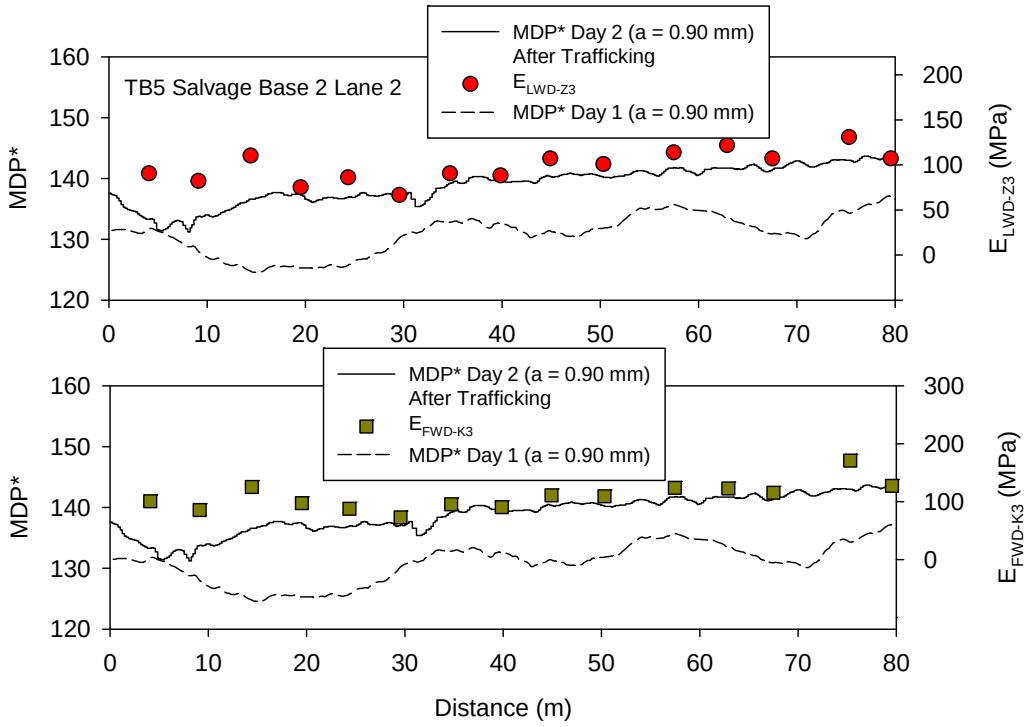

Figure 65. Comparison of MDP* measurements and in-situ point measurements on final salvage base layer lane 2 – TB5

Geostatistical Analysis

Geostatistical semivariograms of MDP* values on TB4 mixed subgrade and salvage base layers 1 and 2 are presented in Figure 66a along with a summary of the spatial statistics (i.e., nugget, sill, and range). MDP* semivariogram on the mixed subgrade layer showed a nested spatial structure with short-range and long-range components, while the semivariograms on the base layers 1 and 2 did not. Similar to findings from the univariate statistics summarized in Table 4, comparison of sill values on the three layers indicate that the mixed subgrade is comparatively more non-uniform than base layers 1 and 2. MDP* semivariograms on TBs 4, 5, and 6 final salvage base layers 1 are presented in Figure 66b. Comparison of sill values on the three test beds indicate that TB6 final base layer is more non-uniform than TB5 final base layer, and TB5 final base layer is more non-uniform than TB4 base layer 2. These findings corroborate with findings from the univariate statistics (Table 4).

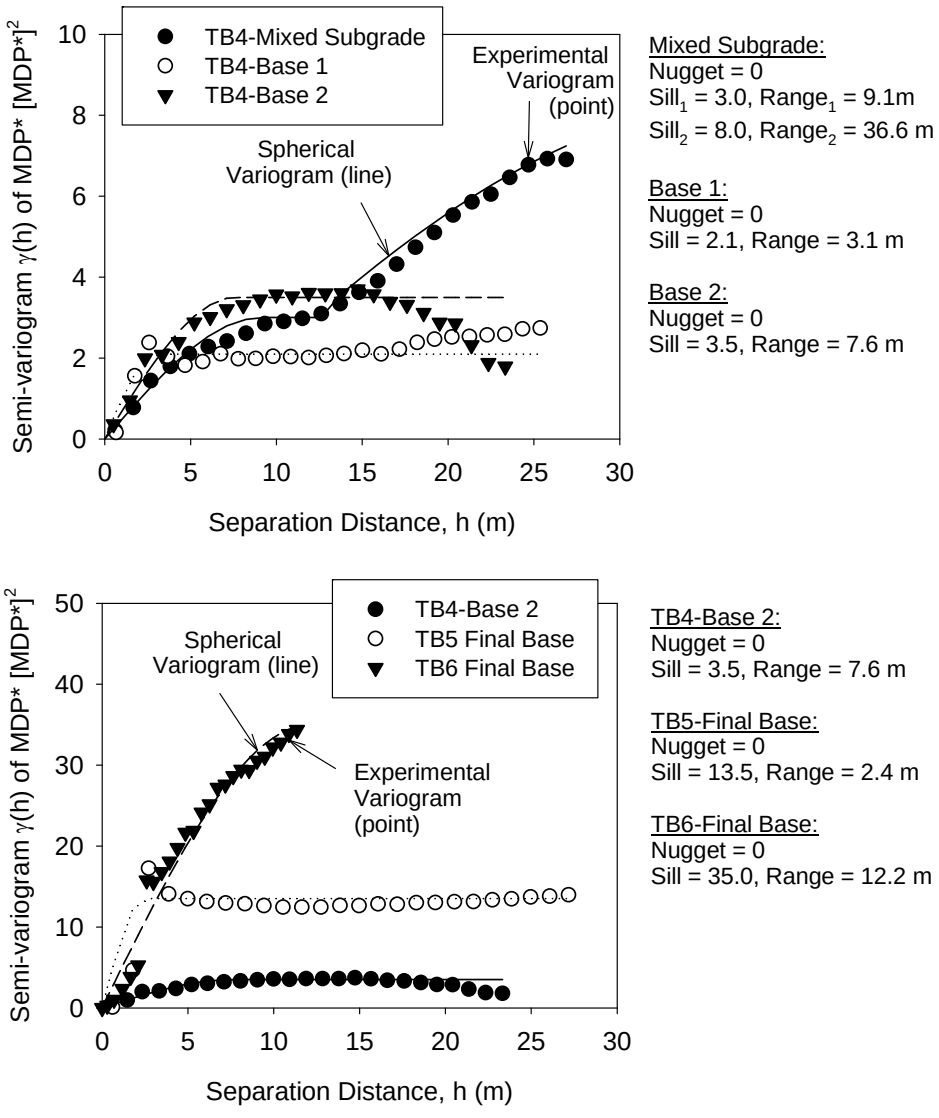

Figure 66. (a) Comparison of MDP semivariograms on TB 4 mixed subgrade, base 1, and base 2 layers, (b) Comparison of MDP semivariograms on TB4, 5, and 6 base layers

Regression analysis

Correlations between MDP* IC-MVs and point-MVs for low and high amplitude settings are presented in Figure 67 and Figure 68, respectively. Correlations between CMV IC-MVs and point-MVs for low and high amplitude settings are presented in Figure 67 and Figure 68, respectively.

TBs 4, 5, and 6 generally had stiff conditions and the MDP* values were greater than 135 at all point-MV locations. Although the relationships generally showed correct trends, they were weak ($R^2 < 0.5$) for all MDP* correlations with point-MVs. The primary reason for such weak correlations is primarily attributed to the narrow MDP* measurement range (varied between 135 and 149). Also, different trends were observed for TB4 and TB5 for MDP* vs. $E_{LWD\text{-}Z3}$ and MDP* vs. $E_{FWD\text{-}K3}$ relationships. This is likely because of differences in underlying support conditions. No information was available from TB5 to assess those conditions.

CMV correlations with $E_{FWD\text{-}K3}$ and CBR_{250} yielded $R^2 > 0.5$, while correlations with $E_{LWD\text{-}Z3}$ yielded $R^2 = 0.35$. No statistically significant relationship was observed between CMV and $E_{FWD\text{-}D3}$.

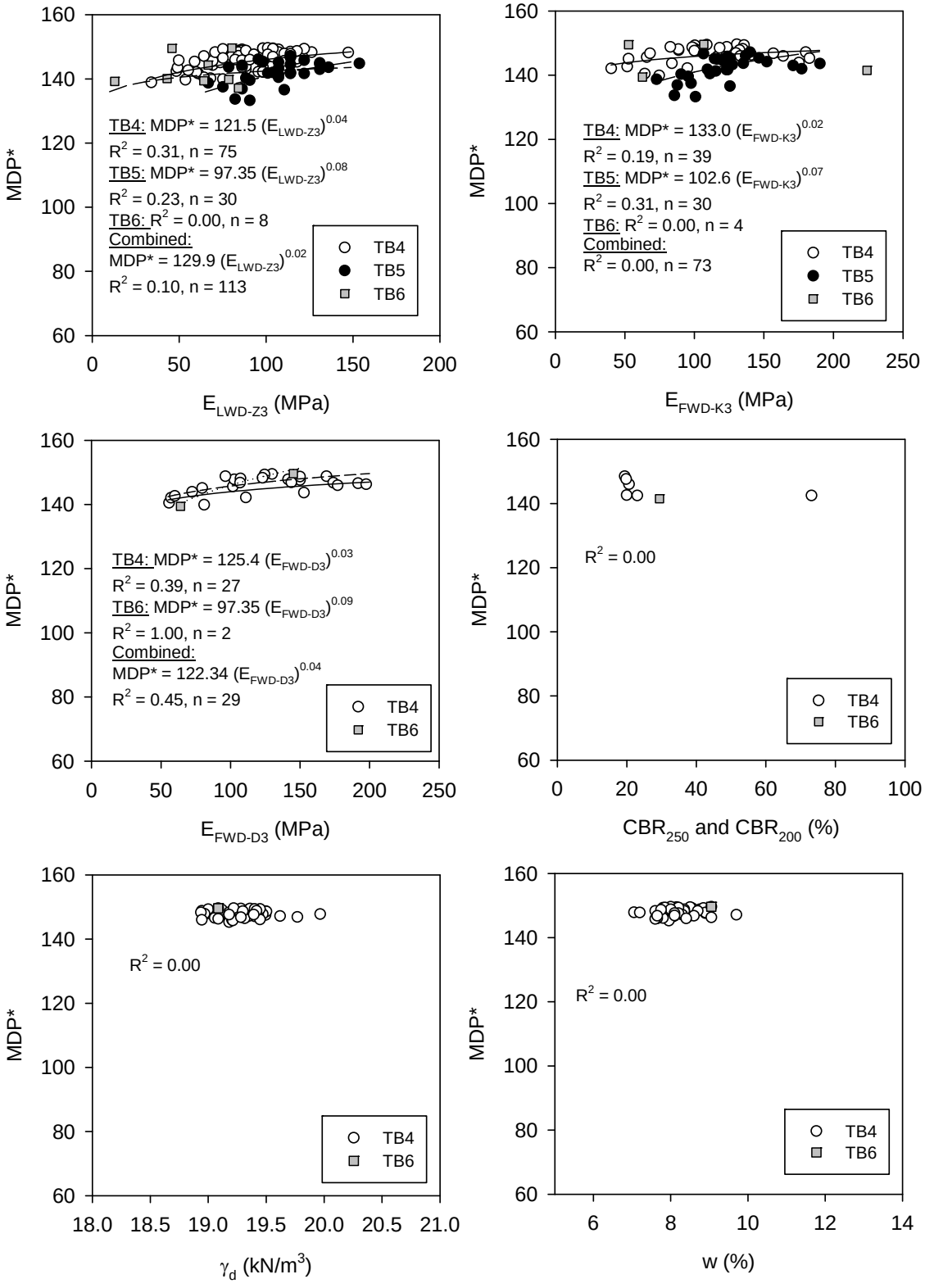

Figure 67. Correlations between MDP* (*a* = 0.90 mm and *f* = 30 Hz) and point-MVs - TBs 4, 5, and 6

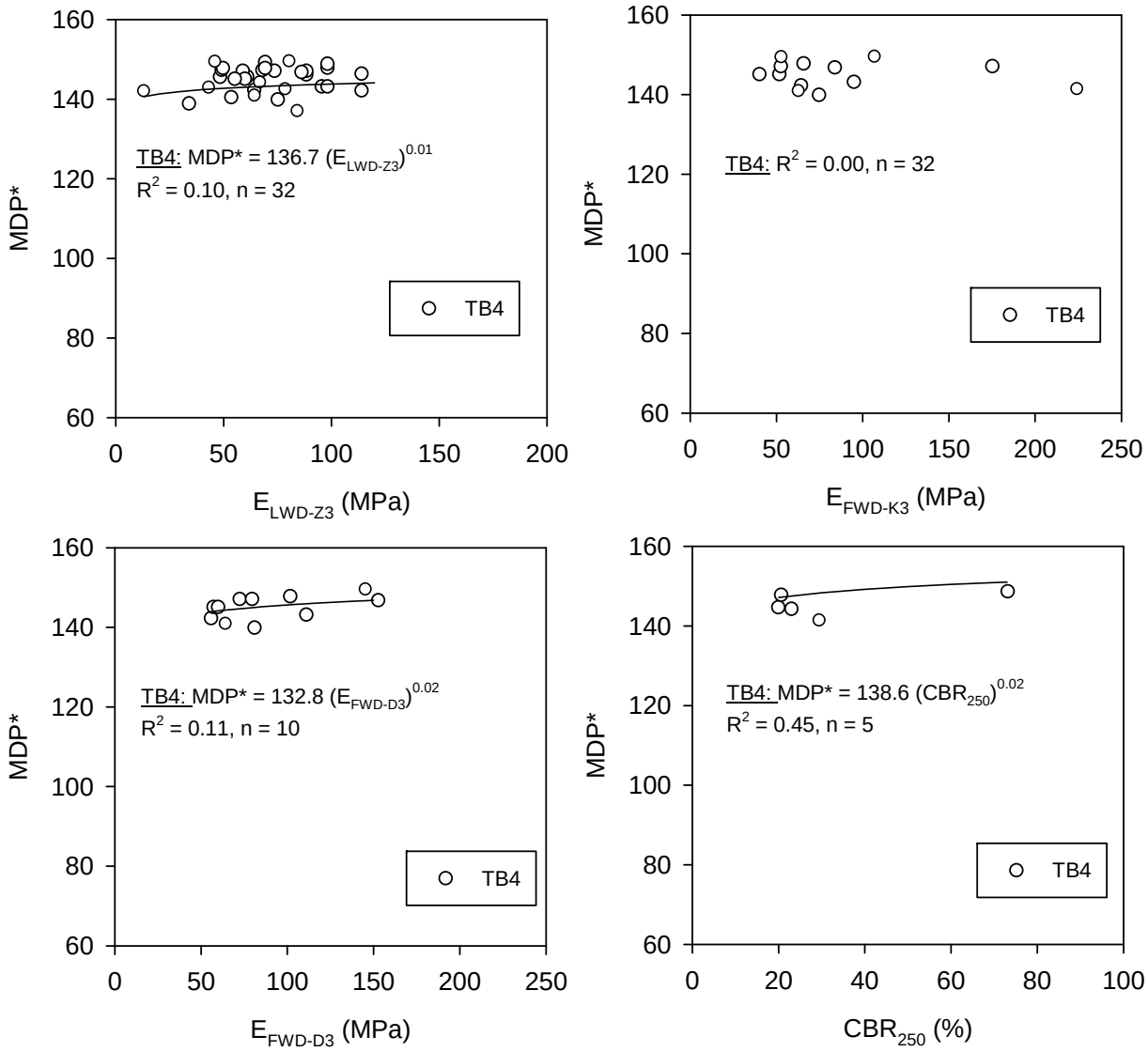

Figure 68. Correlations between MDP* (*a* = 1.80 mm and *f* = 30 Hz) and point-MVs - TB 4

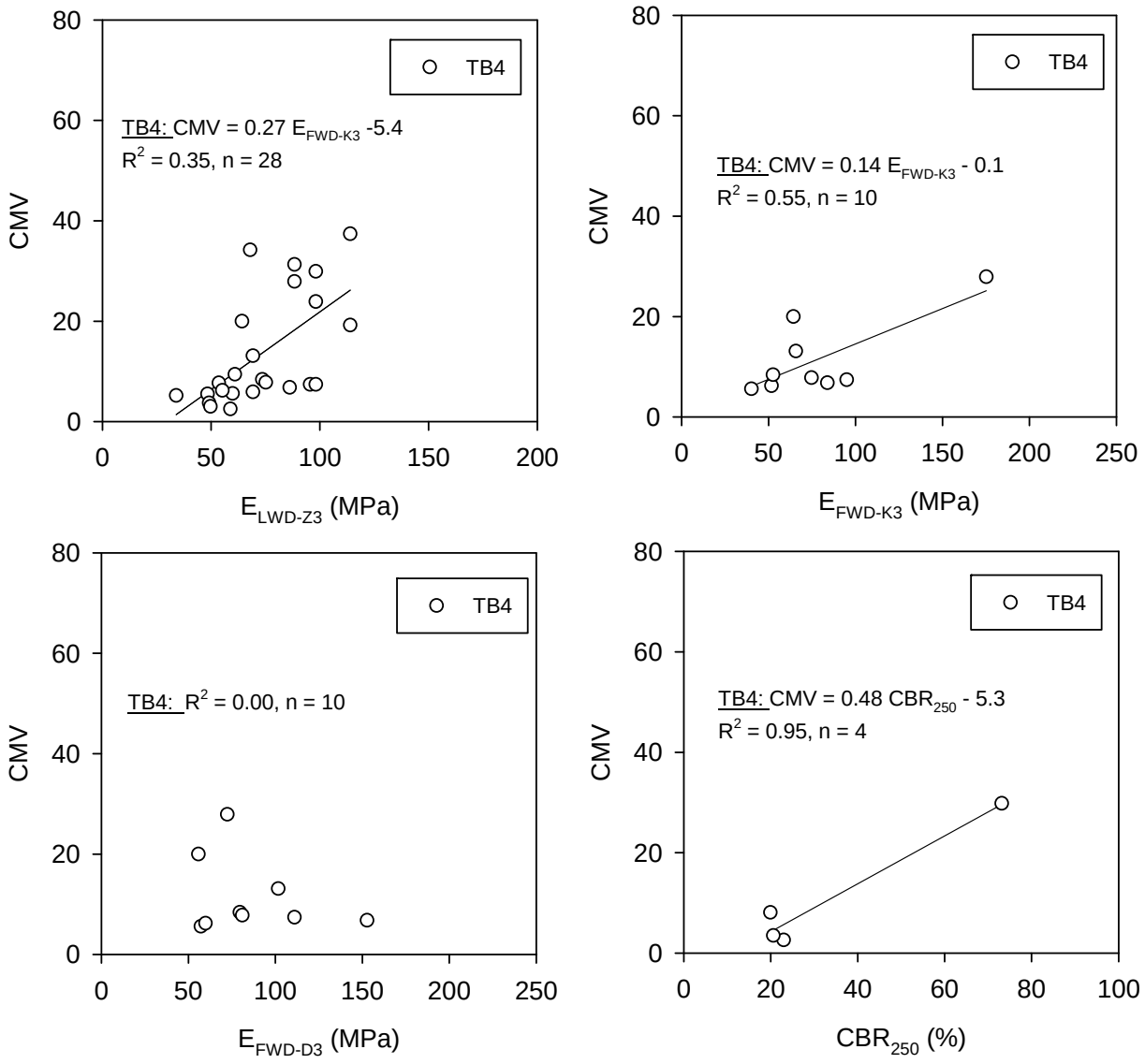

Figure 69. Correlations between CMV (*a* = 0.90 mm and *f* = 30 Hz) and point-MVs - TB 4

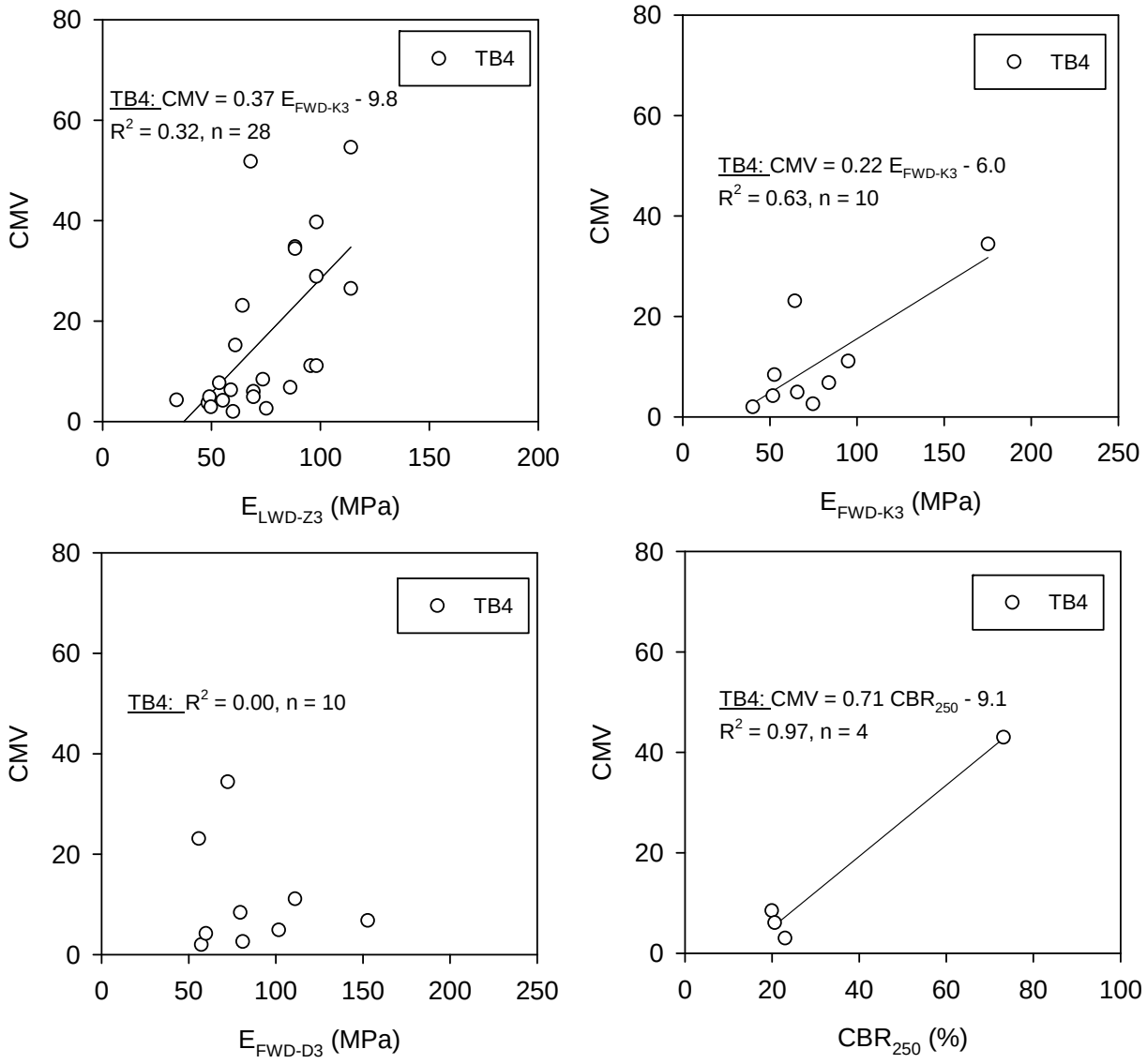

Figure 70. Correlations between CMV (*a* = 1.80 mm and *f* = 30 Hz) and point-MVs - TB 4

FIELD DEMONSTRATION – OPEN HOUSE

An open house was conducted on August 12, 2010 as part of this field study which included dissemination of results from previous IC field studies and results from the current field study as part of a presentation. Demonstration of the two IC rollers, a tour of the Iowa State University geotechnical mobile lab with several laboratory and in-situ testing methods and the KUAB FWD followed the presentation. About 50 people attended the open house including representatives from North Dakota DOT, FHWA, contractor, Caterpillar, and Butler Machinery. Photographs from the open house are presented in Figure 71. Some of the attendees operated the IC rollers and received hands-on-experience.

Figure 71. Photographs from open house on the project site

SUMMARY AND CONCLUSIONS

Results from a field study conducted on the US12 project in Marmarth, ND from August 9-12, 2009 are presented in this report. The project involved evaluating a Caterpillar CS-56 padfoot IC roller on silty subgrade materials and a CS-563E smooth drum IC rollers on salvage base materials. A total of seven test beds involving calibration and production operations were constructed and tested as part of this study. MDP* and CMV IC-MVs were obtained from the test beds in conjunction with various in-situ point-MVs from in-situ nuclear gauge, LWD, FWD, DCP, and borehole shear test devices. IC-MVs maps on the on-board computer display unit were utilized in selecting field QA test locations to simulate a future specification option in some production areas. Key findings and conclusions from this field study are provided below:

Padfoot IC Roller on Subgrade Test Beds:

Three subgrade test beds (TBs 1 to 3, and 7) were constructed and tested in this study. TB1 consisted of three side-by-side calibration lanes compacted in static, low amplitude (a = 0.90 mm), and high amplitude modes (a = 1.80 mm). TB2 consisted of a one-dimensional test strip with visible rutting areas at the surface. TBs 3 and 7 consisted of production areas. Following are some key findings and conclusions from these test beds:

- MDP* IC-MVs are influenced by the vibration amplitude settings used during compaction. Results from TB1 indicated that on average, MDP* IC-MVs generally increased with increasing number of passes when compacted in static and low amplitude mode, while in high amplitude mode the compaction growth curve yielded inconsistent results between passes. This is attributed to de-compaction of the material at the surface and possibly deeper compaction when high amplitude setting is used for compaction.
- The average MDP* values from TB1 obtained in low amplitude mode were either similar or slightly lower (by about 1.02 to 1.05 times) than the MDP* values obtained in static mode. The average MDP* values from TB3 production area in low amplitude mode were about 1.06 times lower than the MDP* values obtained on in static mode.
- The average MDP* values from TB1 obtained in high amplitude (a = 1.80 mm) mode were lower (by about 1.19 to 1.25 times) than the average MDP* values in static and low amplitude modes.
- The average $E_{LWD\text{-}Z2}$ and CBR_{250} point-MVs were lower on low and high amplitude mode lanes, compared to the lanes compacted in static mode. In contrary, the average γ_d was greater on low and high amplitude mode lanes than on static mode lane.
- Regression analysis results between static MDP* IC-MVs and point-MVs showed R^2 values ranging from 0.15 to 0.54. Static MDP* values were better correlated with $E_{LWD\text{-}Z2}$ (R^2 = 0.54), than with CBR_{250} (R^2 = 0.17) and γ_d (R^2 = 0.15). This observation is generally consistent with findings from several previous case studies that the IC-MVs correlate better with stiffness or modulus measurements compared to density measurements. Correlations with low and high MDP* IC-MVs generally showed weak relationships because of limited and narrow range of measurements.
- MDP* IC-MVs and LWD point-MVs conducted in TB2 were able to effectively identify the soft/rutting areas observed at the surface.

- Geostatistical analysis on production areas MDP* IC-MVs indicated nested spherical variogram structures with short- and long-range spatial structures. The long-range spatial structures are likely linked to the spatial variation in the underlying support conditions while the short-range spatial structures are a result of soil properties close to the surface. Similar observations were made by previously White et al. (2010).
- The static MDP* IC-MVs in TB3 production area showed more variability with high sill values compared to low amplitude MDP* IC-MVs. This was also evident with a slightly higher standard deviation (σ) value for static MDP* over low amplitude MDP*.
- The average and COV of static MDP* IC-MVs from TBs 3 and 7 production areas were similar but the spatial statistics (especially the range values) were substantially different between the two test beds. The MDP* values from TB7 showed more spatial continuity in the data with comparatively longer range values compared to TB3, while sill values were somewhat similar for the two test beds. Longer range values represent comparatively more uniform conditions. These differences are not apparent if only univariate statistics (i.e., mean, COV) are assessed.

Smooth Drum IC Roller on Salvage Base Materials (Control, Geogrid Reinforced, and Partial Core-out and Replace Sections):

Three test beds were constructed and tested with salvage base material. TB4 consisted of two salvage base layers reinforced with two TX5 geogrid layers, and were placed over compacted mixed subgrade+base. TB6 was partially treated with core-out and replacement with salvage base due to soft subgrade conditions. TB5 served as a control section with no treatments. On TB4, tests were conducted on the mixed subgrade+base layer, and the two salvage base layers. On TBs 5 and 6, tests were mostly conducted on the final surface of the salvage base layer. Following are the key findings from these test beds.

- CMV IC-MVs showed relatively high variability (COV = 78 to 87%) compared to MDP* IC-MVs (COV = 2%) on TB4 mixed subgrade+base layer. The in-situ modulus and CBR_{250} point-MVs showed COV ranging between 30% and 64%. Variations observed in the points-MVs corroborated well with the variations in CMV IC-MVs while MDP* IC-MVs did not capture these variations.
- MDP* IC-MVs obtained during compaction of salvage base layers indicated slightly different trends in the average MDP* compaction growth for forward (in low amplitude mode) and reverse (in static mode) passes. MDP* IC-MVs were repeatable for forward passes but were affected by variable machine speed for reverse passes, and therefore were not repeatable.
- Results on TB4 indicate that the MDP* IC-MVs and the point-MVs are relatively high and less variable on salvage base layer 1 than on the underlying mixed subgrade layer. On salvage base layer 2, the point-MVs are on average higher on base layer 2 than on the underlying base layer 1 and the mixed subgrade layer. The average MDP* and COV of MDP* were about the same on base layers 1 and 2.
- Variations observed in DCP-CBR profiles corroborated well with variations observed in the BST effective shear strength measurements (i.e., cohesion *c'* and effective angle of internal friction ϕ') with depth in the base and subgrade layers.

- The average MDP* from TB6 control section (i.e., outside the core-out area) was lower (by about 1.06 times) and the COV of MDP* was greater than on TB4 (1% on TB4 and 4% on TB6). The $E_{LWD\text{-}Z3}$, $E_{FWD\text{-}K3}$, and $E_{FWD\text{-}D3}$ point-MVs in the control section were also on average lower (by about 1.1 to 1.6 times) than on TB4. However, it must be noted that only limited number of point-MVs (1 to 4) were obtained in this area.
- MDP* IC-MVs were obtained on TB5 control section on day 1, and day 2 after the area was subjected to construction and vehicular traffic. The MDP* IC-MVs were on average 1.06 times greater on day 2.
- MDP* IC-MVs were slightly lower (by about 1.04 times) on TB5 control section than on the TB4 geogrid reinforced section. The $E_{FWD\text{-}K3}$ point-MVs were also on average slightly lower (by about 1.1 times) on TB5 than on TB4, while the average $E_{LWD\text{-}Z3}$ point-MVs were about the same. The COV of MDP* IC-MVs and point-MVs on TBs 4 and 5 were quite similar.

The results from this study provided new information with application of IC-MVs in conjunction with various QA test devices on subgrade and base materials with and without geogrid reinforcement. The study demonstrated several potential advantages of implementing IC roller operations and various in-situ testing methods into earthwork construction QC/QA practice. To advance the implementation of IC technology in North Dakota, it is recommended that additional field trials be organized with the intent of bringing together various stakeholders to further evaluate the IC technologies and initiate discussions on fully developing IC specifications.

REFERENCES

AASHTO T-99 (2004). "Standard method of test for moisture-density relations of soils using a 2.5 kg (5.5lb) rammer and a 305 mm (12in) drop." American Association of State Highway and Transportation Officials, Washington, D.C.

AASHTO T-180 (2004). "Standard method of test for moisture-density relations of soils using a 4.54 kg (10lb) rammer and a 457 mm (18in) drop." American Association of State Highway and Transportation Officials, Washington, D.C.

ASTM D6951-03. (2003). "Standard test method for use of the dynamic cone penetrometer in shallow pavement application." American Standards for Testing Methods (ASTM), West Conshohocken, Pennsylvania.

ASTM C136-06 (2009). "Standard test method for sieve analysis of fine and coarse aggregates." American Standards for Testing Methods (ASTM), West Conshohocken, Pennsylvania.

ASTM D422-63. (2009). "Standard test method for particle-size analysis of soils." American Standards for Testing Methods (ASTM), West Conshohocken, Pennsylvania.

ASTM D4318-05 (2009). "Standard test methods for liquid limit, plastic limit, and plasticity index of soils." American Standards for Testing Methods (ASTM), West Conshohocken, Pennsylvania.

ASTM D3282-09. (2009). "Standard practice for classification of soils and soil-aggregate mixtures for high construction purposes." American Standards for Testing Methods (ASTM), West Conshohocken, Pennsylvania.

ASTM D2487-10. (2010). "Standard practice for classification of soils for engineering purposes (unified soil classification system)." American Standards for Testing Methods (ASTM), West Conshohocken, Pennsylvania.

Brandl, H., and Adam, D. (1997). "Sophisticated continuous compaction control of soils and granular materials." *Proc. 14th Intl. Conf. Soil Mech. and Found. Engrg.*, Hamburg, Germany, 1–6.

Chilès, J-P., and Delfiner, P. (1999). *Geostatistics – Modeling Spatial Uncertainty.* John Wiley & Sons, Inc., New York.

Clark, I., and Harper, W. (2002). *Practical geostatistics 2000*. 3rd reprint, Ecosse North America Llc, Columbus, Ohio.

Guler, M, Bahia, H.U., Bosscher, P.J., and Plesha, M.E. (2000). "Device for measuring shear resistance of hot-mix asphalt in gyratory compaction," *Transportation Research Record: Journal of the Transportation Research Board*, No. 1723, 119-124.

Handy, R.L., Fox, N.S. (1967). “A soil bore-hole direct-shear test device.” *Highway Research News,* Vol. 27, Highway Research Board, Washington, D.C., 42-51.

Handy , R.L., Schmertmann, J.H, and Lutenegger, A.J. (1985). “Borehole shear tests in a shallow marine environment.” *ASTM Special Publication*, No. 883, ASTM International, West Conshohocken, PA.

Isaaks, E. H., and Srivastava, R. M. (1989). *An introduction to applied geostatistics*. Oxford University Press, New York.

Mooney, M., Rinehart, R., White, D., Vennapusa, P., Facas, N., and Musimbi, O. (2010). “Intelligent soil compaction systems.” *Final Rep.*, *NCHRP Project No. 21-09*, Transportation Research Board, Washington, D.C., in press.

Odemark (1949). Investigations as to the elastic properties of soils and design of pavements according to the theory of elasticity. *Statens Väginstitut*, Mitteilung No. 77, Stockholm, Sweden.

Samaras, A.A., Lamm, R., Treiterer, J. (1991). “Application of continuous dynamic compaction control for earthworks in railroad construction.” *Transp. Res. Rec.,* 1309, Journal of the Transportation Research Board, Washington, D.C., 42–46.

Sandström Å., and Pettersson, C. B., (2004). “Intelligent systems for QA/QC in soil compaction”, *Proc. TRB 2004 Annual Meeting* (CD-ROM), Transportation Research Board, Washington, D. C.

Thompson, M., and White, D. (2008). “Estimating compaction of cohesive soils from machine drive power.” *J. of Geotech. and Geoenv. Engrg.,* ASCE, 134(12), 1771-1777.

Vennapusa, P., White, D.J., and Gieselman, H. (2009). “Influence of support conditions on roller-integrated machine drive power measurements for granular base.”, *Intl. Found. Cong. and Equip. Expo (IFCEE) 2009*, 15-19 March, Orlando, Florida.

Vennapusa, P., and White, D. J. (2009). “Comparison of light weight deflectometer measurements for pavement foundation materials.” *Geotech.Test. J.*, ASTM, 32(3), 239-251.

Vennapusa, P., White, D.J., Morris, M. (2010). “Geostatistical analysis for spatially referenced roller-integrated compaction measurements, *J. of Geotech. and Geoenv. Engrg.,* ASCE, (in print).

White, D. J., Jaselskis, E., Schaefer, V., Cackler, T. (2005). “Real-time compaction monitoring in cohesive soils from machine response.” *Transp. Res. Rec., 1936*, Journal of the Transportation Research Board, Washington D.C., 173–180.

White, D.J., and Thompson, M. (2008). Relationships between in situ and roller-integrated compaction measurements for granular soils. *J. of Geotech. and Geoenv. Engrg.,* ASCE, 134(2), 1763-1770.

White, D.J., Vennapusa, P., Zhang, J., Gieselman, H., Morris, M. (2009). *Implementation of Intelligent Compaction Performance Based Specifications in Minnesota,* Final Report MN/RC 2009-14, Minnesota Department of Transportation, St. Paul, Minnesota, July.

White, D.J., Vennapusa, P., Gieselman, H., Zhang, J., Goldsmith, R., Johanson, L., Quist, S. (2010). *Accelerated Implementation of Intelligent Compaction Monitoring Technology for Embankment Subgrade Soils, Aggregate Base, and Asphalt Pavement Materials* TPF-5(128) – *New York IC Demonstration Field Project*, ER10-01, Report submitted to The Transtec Group, FHWA, January.

Zorn, G. (2003). *Operating manual: Light drop-weight tester ZFG2000*, Zorn Stendal, Germany.